Washington University in St. Louis
Washington University Open Scholarship

Arts & Sciences Electronic Theses and Dissertations

Arts & Sciences

5-9-2024

Infrared Magneto-Spectroscopy of Correlated Electron Systems in Graphene

Yashika Kapoor
Washington University in St. Louis

Follow this and additional works at: https://openscholarship.wustl.edu/art_sci_etds

Recommended Citation

Kapoor, Yashika, "Infrared Magneto-Spectroscopy of Correlated Electron Systems in Graphene" (2024). *Arts & Sciences Electronic Theses and Dissertations*. 3031.
https://openscholarship.wustl.edu/art_sci_etds/3031

This Dissertation is brought to you for free and open access by the Arts & Sciences at Washington University Open Scholarship. It has been accepted for inclusion in Arts & Sciences Electronic Theses and Dissertations by an authorized administrator of Washington University Open Scholarship. For more information, please contact digital@wumail.wustl.edu.

WASHINGTON UNIVERSITY IN ST. LOUIS
Department of Physics

Dissertation Examination Committee:
Erik A. Henriksen, Chair
Mark Lawrence
Kater W. Murch
Alexander Seidel
Xi Wang

Infrared Magneto-Spectroscopy of Correlated Electron Systems in Graphene

by

Yashika Kapoor

A dissertation presented to
Washington University in St. Louis
in partial fulfillment of the
requirements for the degree
of Doctor of Philosophy

May, 2024
St. Louis, Missouri

©2024, Yashika Kapoor

Table of Contents

List of Figures

Acknowledgements

First and foremost, let me thank my thesis advisor, Erik Henriksen, for his patience and encouragement all these years. He has significantly shaped my growth as a researcher, guiding me to tackle challenging problems with diligence and persistence and helping me evolve into a better and more confident experimentalist. His continuous stream of ideas and enthusiasm has been a constant source of inspiration. Erik has extended tremendous support, which was truly responsible for me navigating through the struggle of getting the infrared back up and running.

I am sincerely grateful to Kater Murch and James Buckley for their support and invaluable advice regarding my research and academic path. I also extend my thanks to my other committee members, Alexander Seidel, Xi Wang, and Mark Lawrence, for their much-appreciated feedback and suggestions. I also acknowledge the Institute of Materials Science and Engineering at Washington University in St. Louis and its staff for their assistance over the years.

My labmates over the last several years. I especially acknowledge Jordan Russell for patiently teaching me everything about the infrared setup. Even when he was not around, I have found his lab notebooks to be like treasure troves of information. Additionally, I want to thank Jesse Balgley for showing me the ropes in nano-fabrication. Thanks also to Xinyi Du for being a willing ear for ideas and complaints. Lastly, I thank Jordan Pack, Jackson Butler, Yiwei Le, Erdong Song, and Gwyneth Phillips. Working alongside such a talented and supportive team of individuals has been an incredible experience.

The Physics department at WashU has been a welcoming and supportive community throughout my journey, thanks to the tireless efforts of the students, staff, and faculty. I extend my gratitude to my fellow graduate students Kiandokht, Andrew, Matheus, Paul,

Fang, Linghan, Luis, Wolfgang, Serra, Daria, and Ali, who not only shared the challenges of graduate school but also provided invaluable support. Special appreciation goes to Maryam, my steadfast companion since the first day of graduate school. The highlights of my education have been the relationships I have formed in my (long!) time in St.Louis. A heartfelt thank you to my friends like family Sakshi, Pankhuri, Priya, Neha, Sheetal, Girish, and Shubham.

I would like to express my gratitude to Dr. Vineet Kumar, whose mentorship sparked my interest in research. I fondly recall the invaluable time I spent at RRCAT and the countless hours spent reading Feynman lectures at the library.

Finally, I would like to express my deepest gratitude to my family: my very kind and supportive partner, Sukrant Dhawan; my sweet grandmother, who has always showered me with love and wisdom; my sister, whose unwavering support has been my rock; my brother; and my parents. I am grateful to my parents for letting me be my own person. Coming from our background, where women are often dictated what to do and how to do it, my parents kept an open mind, supported me, and believed in my ability to make my own decisions, including the decision to move countries. I know it was not easy. Lastly, I acknowledge the rebellious girl I once was for her resilience in fighting for her dreams.

Yashika Kapoor

Washington University in St. Louis

May, 2024

ABSTRACT OF THE DISSERTATION

Infrared Magneto-Spectroscopy of Correlated Electron Systems in Graphene

by

Yashika Kapoor

Doctor of Philosophy in Physics

Washington University in St.Louis, 2024

Erik A. Henriksen (Chair)

Van der Waals (vdW) heterostructures represent a novel class of artificial materials created by layering atomically thin planar crystals and offer a promising platform for band structure engineering. Here, we focus on a vdW heterostructure of monolayer graphene (G) coupled to a hexagonal boron nitride (h-BN). We utilize cyclotron resonance (CR) spectroscopy as a primary investigative tool for probing the interacting Dirac fermions in graphene. This work presents a system capable of conducting broadband far- to mid-infrared CR spectroscopy in high magnetic fields and ultra-low temperatures. Our study investigates the influence of the h-BN substrate on the properties of graphene in two key aspects. First, the atomic-scale modulations break the local symmetry between the graphene sublattices, influenced by the potential difference between boron and nitrogen atoms in h-BN. We perform CR measurements on high-quality graphene devices, presenting the first observation of the complete lifting of the four-fold degeneracy of Landau levels (LLs) due to broken spin and valley symmetries. Secondly, we explore the effect of near-perfect alignment between G/h-BN that causes the superlattice potential to match the magnetic length scale in graphene, yielding a self-similar energy spectrum. We spectroscopically investigate the fractal levels by measuring optical transitions across the reconstructed LLs in G/h-BN moiré superlattice.

Chapter 1

Introduction and Overview

This work is motivated by a cascade of discoveries that have revolutionized our understanding and exploration of two-dimensional (2D) materials. Initially deemed thermodynamically unstable, the isolation of atomically thin 2D structures from layered materials heralded a new era. Through micromechanical exfoliation, Geim and Novoselov demonstrated the startling possibility of obtaining monolayers from graphite [1], MoS_2 [2], and other layered materials [3] in the laboratory. The isolation of these monolayers sparked excitement and raised intriguing questions about how their two-dimensional nature influences their electronic properties.

Layered 2D materials showcase a variety of electronic behaviors, spanning from superconductivity and metallic to semimetallic, semiconductor, and insulating properties [4]. The transition to the 2D realm offers an unexplored frontier for investigating the impact of dimensionality on these properties. Moreover, combining different monolayers to form heterostructures presents even greater opportunities for novel device applications [5].

Dimensionality lies at the heart of many fundamental physical phenomena, offering a rich playground for exploration. By reducing the spatial degrees of freedom of charge carriers, we can uncover novel physics previously hidden in higher dimensions. Experimentally, this dimensional confinement can be achieved artificially or directly, reducing material dimen-

sionality.

Graphite, comprised of layers of hexagonally-bonded carbon atoms held together by weak van der Waals (vdW) interactions, can be exfoliated to obtain graphene monolayers. The discovery of graphene in 2004 [6] through mechanical exfoliation marked a milestone, revealing its exceptional properties as an ultra-thin electrical and thermal conductor [7] with high carrier mobility and ambipolar field-effect gate modulation [6]. The isolation of graphene ushered in a new era of research into 2D materials, fueled by the simplicity and versatility of the micromechanical exfoliation method.

Electrons in typical two-dimensional electron systems are described by a scalar Hamiltonian. In contrast, electrons in monolayer graphene are massless and described by a matrix Dirac Hamiltonian. Unlike most semiconductor materials, which exhibit a parabolic dispersion, the quasi-particle energy in graphene follows a linear function of momentum, $E \propto k$. While various parabolic systems display diverse behaviors due to effective masses, non-parabolicity effects, and multiple active bands, their underlying dispersions remain similar. Graphene stands out for its linear dispersion, akin to a relativistic system of massless charge carriers where the Fermi velocity in graphene plays a material analog of the speed of light. Moreover, graphene features simple degenerate points where the conduction and valence bands touch, forming what are known as Dirac points. With its single plane of carbon atoms on a honeycomb lattice, graphene features the simplest atomic structure among van der Waals (vdW) materials. The unit cell of graphene comprises two identical carbon atoms represented by two different lattice vectors, effectively forming two equivalent triangular lattices conventionally termed A and B. Beyond electron spin, the sublattice structure of graphene confers a second conserved degree of freedom called "pseudospin", leading to a system of chiral, massless, charged particles known as Dirac fermions.

Notice that in quantum mechanics, the momentum p of the particle relates to its wave-

length λ, by $p = \hbar/\lambda$ and hence the kinetic energy behaves as $K = \hbar^2/(2m^*\lambda^2)$, where m^* is the effective mass of the particle. Suppose the average distance between electrons is l. In that case, we see that the average kinetic energy per electron has to be of the order $E_k \approx \hbar^2 {n_d}^{2/d}(2m^*)$ where $n_d = 1/l^d$ is the average electron density in d spatial dimensions. On the other hand, the Coulomb interaction is given by

$$V(r) = \frac{e^2}{\epsilon_0 r}, \tag{1.1}$$

where e is the electron charge, and ϵ_0 is the dielectric constant of the medium. Notice that Coulomb energy per electron is in order $E_C = e^2 {n_d}^{1/d}/\epsilon_0$. Thus, the ratio of Coulomb to kinetic energy is given by $r_s = E_C/E_K \propto (n_0/n_d)^{1/d}$, where $n_0 = [m^* e^2/\hbar^2\epsilon]^d$ depends on the material properties. Therefore, the kinetic energy dominates at higher electron densities, $n_d \gg n_0$, while at lower densities, $n_d \ll n_0$, the Coulomb energy dominates. Therefore, the relative strength of the kinetic to Coulomb interactions is completely controlled by the electron density. Due to the linear energy dispersion relation of graphene, $E_K = \pm v_f |\mathbf{p}| k$, where v_F is the Fermi velocity of graphene. We reach very different conclusions if we take this value and reconsider the abovementioned argument on the relevance of the Coulomb interactions. The average kinetic energy per electron scales as $E_G \approx \hbar v_F n^{1/2}$ and consequently, the ratio of Coulomb to kinetic energy is given by

$$\alpha = \frac{E_C}{E_G} = \frac{e^2}{\epsilon_0 \hbar v_F}, \tag{1.2}$$

and is independent of the electron density n, depending only on material properties and environment conditions ϵ_0. For suspended graphene $\kappa = 1$, one finds $\alpha \approx 2.3$, so the interactions are quite strong. The interaction in graphene can thus be adjusted by altering

its surroundings.

Recent advancements in sample preparation, optical detection, transfer, and manipulation of layered materials have paved the way for new opportunities in the domain of 2D van der Waals crystals, including hexagonal boron nitride (h-BN). With a lattice constant similar to that of graphene, h-BN serves as an insulating substrate and encapsulation layer owing to its atomic flatness and chemical inertness. The close values of lattice constants between graphene and h-BN also offer an additional degree of freedom during the fabrication of vdW heterostructures: the twist angle between the crystallographic axes of the two materials. Aligning the crystallographic orientation between h-BN and graphene enables the formation of a superlattice with a lattice spacing of approximately 100 atoms greater than that of the individual crystals. The presence of these superlattices introduces repetitive changes in the electronic structure of graphene and shows a self-similar pattern. The electronic properties of graphene are sensitive to environmental conditions; they can be modified by the proximity of other layered structures. In this work, we aim to utilize cyclotron resonance to probe deeply into aspects of the physics of interacting electrons that other techniques are not sensitive to.

A breakthrough recently transforming the field of 2D materials and the entire condensed matter community is the revelation of intrinsic unconventional superconductivity in graphene superlattices [8]. When two monolayers of graphene are stacked with a small relative twist angle, the resulting band structure exhibits a remarkably flat pair of bands at a sequence of 'magic' angle. This discovery opens up an exceptional playground to explore many-body quantum phases of matter, allowing for the realization of a wide range of novel correlated or topological phenomena.

In the subsequent sections, we provide a brief overview of the fundamental properties of graphene, including its unique band structure. We also delve into the influence of out-of-plane magnetic fields on the band structure of graphene, a key aspect of understanding the

experimental findings that we will present later in this thesis. We discuss various experimental techniques used to probe graphene properties, with a particular focus on cyclotron resonance and its significance in understanding the intrinsic properties of graphene. We further address the limitations of the single-electron model and the role of electron-electron (e-e) interactions in shaping the observable properties of graphene, drawing from both theoretical frameworks and experimental evidence. Additionally, we discuss the influence of the h-BN substrate on the electronic band structure of graphene.

1.1 Theoretical overview of graphene

Through mechanical exfoliation with scotch tape, single-layer graphene emerges as a derivative of its 3D precursor, graphite, presenting remarkable traits. Structurally, graphene consists of a single atomic layer of carbon atoms arranged in a honeycomb lattice formed by sp^2-hybridized bonds. Isolating a flat single-atom-thick layer of graphene was possible due to the much weaker Van der Waals force between graphite layers compared to covalent bonds within a single layer. This unique 2D carbon allotrope demonstrates thermodynamic stability, with remarkable mechanical strength and thermal conductivity attributed to its strong covalent bonds. The optical properties of graphene stem directly from its 2D structure and gapless electronic spectrum (discussed below). Despite being only one atom thick, the 2.3% opacity [9] of graphene makes it visible to the naked eye through a glass slide covered with graphene.

1.1.1 Electronic structure of single-layer graphene in the absence of interactions

The unusual electronic properties of graphene stem from three key factors: its 2D structure, the honeycomb lattice arrangement, and the uniform occupancy of carbon atoms across all lattice sites, thereby introducing inversion symmetry. Since these concepts have been known for decades and have been explained in many excellent references [10–12], we will only review key elements and briefly overview the graphene band structure, focusing on a single-particle approximation that neglects electron-electron interactions. Graphene has the honeycomb crystal lattice shown in Figure 1.1. The lattice vectors of the triangular Bravais lattice are

$$\vec{a}_1 = \frac{a}{2}\left(3, \sqrt{3}\right), \quad \vec{a}_2 = \frac{a}{2}\left(3, -\sqrt{3}\right), \tag{1.3}$$

where $a = 1.42$ Å is the nearest-neighbor distance(not the graphene lattice constant). The unit cell shown in Figure 1.1a contains two atoms belonging to two distinct sublattices called A and B. Each atom of sublattice A is surrounded by three atoms of sublattice B, and vice versa. The vectors connecting each atom to its three nearest neighbors are

$$\vec{\delta}_1 = \frac{a}{2}\left(1, \sqrt{3}\right), \quad \vec{\delta}_2 = \frac{a}{2}\left(1, -\sqrt{3}\right), \quad \vec{\delta}_3 = a\left(-1, 0\right). \tag{1.4}$$

The reciprocal lattice of the triangular Bravais lattice is also triangular, with lattice vectors

$$\vec{b}_1 = \frac{2\pi}{3a}\left(1, \sqrt{3}\right), \quad \vec{b}_2 = \frac{2\pi}{3a}\left(1, -\sqrt{3}\right). \tag{1.5}$$

In Figure 1.1b we show the Brillouin zone (BZ) with the special high-symmetry K, $K^{'}$

and M points

$$\vec{K}' = \left(\frac{2\pi}{3a}, \frac{2\pi}{3\sqrt{3}a}\right), \quad \vec{K} = \left(\frac{2\pi}{3a}, -\frac{2\pi}{3\sqrt{3}a}\right), \quad \vec{M} = \left(\frac{2\pi}{3a}, 0\right). \tag{1.6}$$

The inequivalent K and K' points are often referred to as valleys in momentum space. In single-layer graphene, the nearest-neighbor carbon atoms form sp^2 hybridized bonds, giving rise to two distinct electronic bands, π and σ. The σ bands primarily influence electronic phenomena at energies greater than 3 eV. The unique low-energy properties of graphene stem from the π bands, whose structure can be elucidated within the tight-binding model proposed by Wallace. This model exclusively considers the π states and nearest-neighbor hopping terms, represented by the parameter γ_0 that facilitates hopping processes solely between sublattices. Within this framework, the basis of the electronic states comprises two π states per unit cell, belonging to atoms of the two triangular sublattices, denoted as A and B, within the full honeycomb lattice. Consequently, the tight-binding Hamiltonian [12] governing the electronic behavior is described by a 2×2 matrix since each unit cell contains two $2p_z$ orbitals, one centered at each atomic site:

$$H_K = \begin{pmatrix} E_D & \gamma_0 S_{\mathbf{k}} \\ \gamma_0 S_{\mathbf{k}}^* & E_D \end{pmatrix}, \tag{1.7}$$

where E_D is the nearest-neighbor bonding energy, $\mathbf{k} = k_x, k_y$ is the in-plane crystal momentum, and

$$S_{\mathbf{k}} = \sum_{\vec{\delta}} e^{i\mathbf{k}\vec{\delta}} = \exp\left(\frac{2ik_x a}{\sqrt{3}}\right) + \exp\left(\frac{-ik_x a}{\sqrt{3}}\right)\cos(k_y a), \tag{1.8}$$

represents the sum of the hopping amplitudes between a given site and its nearest neighbors.

The resulting spectrum of single-layer graphene has the form

$$E_{\pm}(\mathbf{k}) = E_D \pm \gamma_0 |S_{\mathbf{k}}|. \tag{1.9}$$

The electronic properties of graphene are controlled by the low energy ($|E| \ll \gamma_0$) dispersion around the two inequivalent K and K' points, corresponding to the electron states near the Fermi energy. By defining $\mathbf{q} = \mathbf{k} - \mathbf{K}$. The energy dispersion has a conical shape:

$$E_{\pm}(\mathbf{q}) = \pm \hbar v_F |\mathbf{q}|. \tag{1.10}$$

Near the corners of the hexagonal Brillouin Zone (BZ), the velocity is characterized by $v_F = \sqrt{3}\gamma_0 a/2\hbar$. This linear dispersion is a 2D analog of the Dirac spectrum for massless fermions, expressed as $E = \sqrt{p^2c^2}$. However, instead of the velocity of light (denoted as c), we have the parameter of band velocity, $v_F \simeq c/300$. In contrast to true Dirac fermions, where the electronic spin represents their internal degree of freedom, graphene possesses an additional degree of freedom represented by the sublattice index (or valley degree of freedom), leading to a 4-fold degeneracy in graphene. The linear dispersion corresponds to the spectrum of the Dirac-like Hamiltonian for low-energy massless Dirac fermions. In the sublattice basis A, B, the 2×2 Hamiltonian can be rewritten as:

$$H_K = \hbar v_F \begin{pmatrix} 0 & k_x - ik_y \\ k_x + ik_y & 0 \end{pmatrix} = \hbar v_F \vec{\sigma} \cdot \vec{k}. \tag{1.11}$$

The Dirac Hamiltonian is essentially an expansion of the tight-binding Hamiltonian (Eq. 1.7) near the K point. Similarly, near the K' point, the Hamiltonian takes the form $H_{K'} = \hbar v_F \vec{\sigma}^* \cdot \vec{k}$, where $\vec{\sigma} = (\sigma_x, \sigma_y)$ represents the 2D vector of Pauli matrices (with * indicating

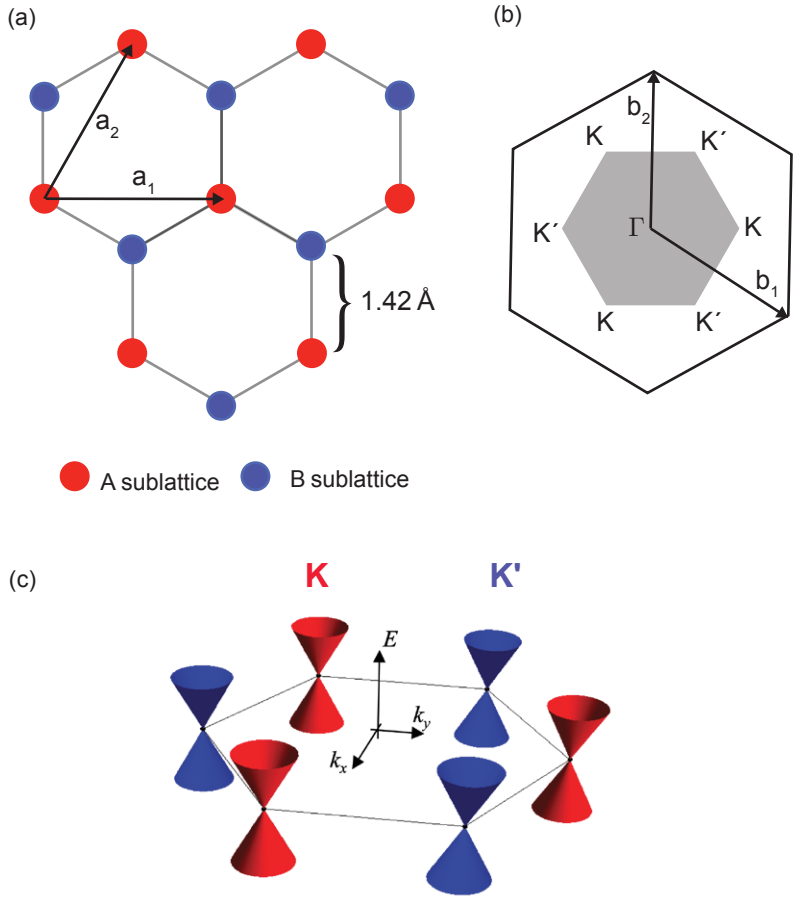

Fig. 1.1: (a) The crystal lattice of monolayer graphene with red and blue circles representing the trigonal A and B sublattices. (b) First Brillouin zone of the reciprocal lattice, where b_1 and b_2 represent the primitive reciprocal lattice vectors. (c) The low-energy band structure is linear, presented by "Dirac cones" with a zero in the energy coinciding with each of the six corners of the BZ.

.

its complex conjugate). The eigenfunctions near the Dirac points are expressed as follows:

$$\Psi_{\pm}(\mathbf{k}) = \frac{1}{\sqrt{2}} \begin{pmatrix} \pm e^{i\theta_k} \\ 0 \end{pmatrix}, \quad \text{where} \quad \tan\theta_k = \frac{k_x}{k_y}. \tag{1.12}$$

This state is characterized by its "helicity" – that is, as the quasiparticle momentum rotates once around the Dirac point, the phase of the eigenfunction changes by π. In graphene, this helicity is called chirality because of the inability to transform one type of dispersion into another[13]. The chirality in graphene indicates a pseudospin quantum number for the charge carriers. This quantum number is analogous to spin but is entirely independent of the electronic spin. The pseudospin quantum number allows for the distinction of contributions from each sublattice. So, for example, polarizing the graphene to a pseudospin "up" state leads to all the electrons residing in the A sublattice, and similarly, a pseudospin "down" state has all electrons on the B sublattice.

The conical dispersion yields the single-particle density of states (DOS), $\nu(E)$, that is linear in E. This can be obtained by considering the number of states $n = k^2/2\pi$, in the reciprocal space within a circle of radius $|k'| = |E|/\hbar v_F$ and taking into account the spin and valley degeneracy. The DOS associated with this point per unit area is

$$\nu(E) = \frac{2}{\hbar v_F}\frac{dn}{dq} = \frac{2}{\pi\hbar^2 {v_F}^2}|E|. \tag{1.13}$$

The frequently needed relations between the zero temperature chemical potential μ (referred to the Dirac point energy E_D), Fermi momentum k_F, and the carrier density n_s are

$$k_F = \sqrt{\pi|n_s|}, \quad \mu \simeq E_F = \mathrm{sgn}(n_s)\hbar v_F k_F. \tag{1.14}$$

The density of states in graphene exhibits qualitative differences compared to non-relativistic 2D electron systems, leading to significant experimental implications. In graphene, the DOS is linear in energy, electron-hole symmetric, and vanishes at the Dirac point (DP), contrasting with the constant value and quadratic energy dispersion for the more traditional parabolic system. Graphene can be easily doped through an external gate voltage. At zero doping, the lower half of the band is perfectly filled up to the DPs. The application of a gate voltage induces a non-zero charge, effectively injecting either electrons or holes (depending on the polarity of the applied voltage) into the upper or lower half of the Dirac cones. The ambipolar gating behavior, driven by electron-hole symmetry, changes the sign of the charge at the DP. The difference between Dirac fermions and Schrödinger fermions can be observed in transport measurements. One of the most notable examples is the unconventional quantum Hall effects discussed in the following sections.

1.1.2 Landau levels in graphene

This section discusses the impact of a magnetic field applied perpendicular to the plane of monolayer graphene on its electronic properties. At low energies, the momentum values in momentum space are confined to regions near two distinct valleys located at

$$K_\xi = \xi \left(\frac{4\pi}{3a}, 0 \right), \tag{1.15}$$

here, $\xi = \pm 1$ describes two distinct valleys. To facilitate analysis, we define $\vec{p} = \hbar\vec{k} - \hbar\vec{K_\xi}$. With this definition of $\vec{p}$, the tight-binding Hamiltonian in 1.11 can be rewritten as

$$H_\xi = v_F \begin{pmatrix} 0 & \xi p_x - i p_y \\ \xi p_x + i p_y & 0. \end{pmatrix} \tag{1.16}$$

A perpendicular magnetic field, $\mathbf{B} = |B|\hat{e_z}$, has a vector potential $\vec{A}$ parallel to the layer plane so that the canonical momentum operator in the Hamiltonian, H_ξ, is shifted to

$$\vec{p} = -i\hbar\vec{\Delta} + e\vec{A}. \tag{1.17}$$

When a magnetic field is applied to conductors, free charge carriers are forced to circulate in cyclotron orbits. In the non-relativistic case, observed in systems like 2D electron systems on helium or in semiconductor heterostructures, the Landau level sequence comprises equally spaced levels akin to those of a harmonic oscillator, given by $E_n = \hbar\omega_c(N + 1/2)$, with $\omega_c = eB/m^*$ the cyclotron frequency. In graphene, however, the charge carrier velocity remains independent of energy, resembling that of massless particles. The zero density of states in graphene corresponds to one electron per atomic site or two electrons per unit cell, resulting in a half-filled zero-energy Landau level at neutral doping. Furthermore, the linear band structure leads to an uneven spacing of Landau levels in energy,

$$E_{n,\pm} = \pm v_F\sqrt{2\hbar eBn} \quad n \in \mathbf{N}. \tag{1.18}$$

The degeneracy of each Landau level is $g_v g_s|eB|/h$, where we consider both spin and valley degree of freedom. The structure of the LLs, as shown in 1.2a, leads to the unconventional half-integer quantum Hall effect in graphene, which was predicted by theory [14] and subsequently observed experimentally [15] [16].

In contrast to the Landau levels (LLs) observed in conventional 2D electron gases (2DEGs), where $E_n = \hbar\omega_c(N+1/2)$, $n \in \mathbf{N}$, it is important to highlight a distinct LL at $E = 0$ resulting from the electron-hole symmetry in graphene as shown in Figure 1.2a. This zero-energy LL arises equally from electron and hole states, causing a half-integer shift in the number

of flux quanta required to fill an integer number of LLs. The fourfold degeneracy of LLs manifests in the formation of quantum Hall (QH) plateaus [17]:

$$\sigma_{xy} = \pm 4\left(N + \frac{1}{2}\right)\frac{e^2}{h} \quad n \in \mathbf{N}. \tag{1.19}$$

The LL filling factor, ν, is related to the carrier density n_s

$$\nu = \frac{n_s h}{eB}. \tag{1.20}$$

Note that $\nu = -2$ and $\nu = 2$ correspond to completely emptying or filling the zeroth LL ($E_{n=0} = 0$). Figure 1.2b shows a typical Hall conductance trace (G_{xy}) in units of e^2/h and longitudinal resistance (R_{xx}) vs charge density n_s for fixed $B = 8$ T. The characteristic half-integer QHE plateaus at $G_{xy} = \nu e^2/h$ are observed for filling factor, $\nu = \pm 2 \pm 6 \pm 10$. However, the longitudinal resistance nearly vanishes at densities where the Hall conductance exhibits plateaus, which is the hallmark of QHE in single-layer graphene [18].

1.2 Cyclotron resonance

In the context of materials, CR arises [19] when a charged particle, characterized by its charge e, moves in a circular trajectory perpendicular to an applied magnetic field with a cyclotron frequency $\omega_c = eB/m_c$. Here, m_c denotes the cyclotron mass, which is a measure of the effective mass m in the effective mass approximation, where m^* describes the inertial response of a charged particle moving in a periodic potential. When an electromagnetic field with frequency $\omega = \omega_c$ is applied, the particle absorbs energy from the electromagnetic field, resulting in cyclotron resonance. In semiconductor materials, various scattering processes can modify the resonant behavior of particles. A well-defined resonance is observed when

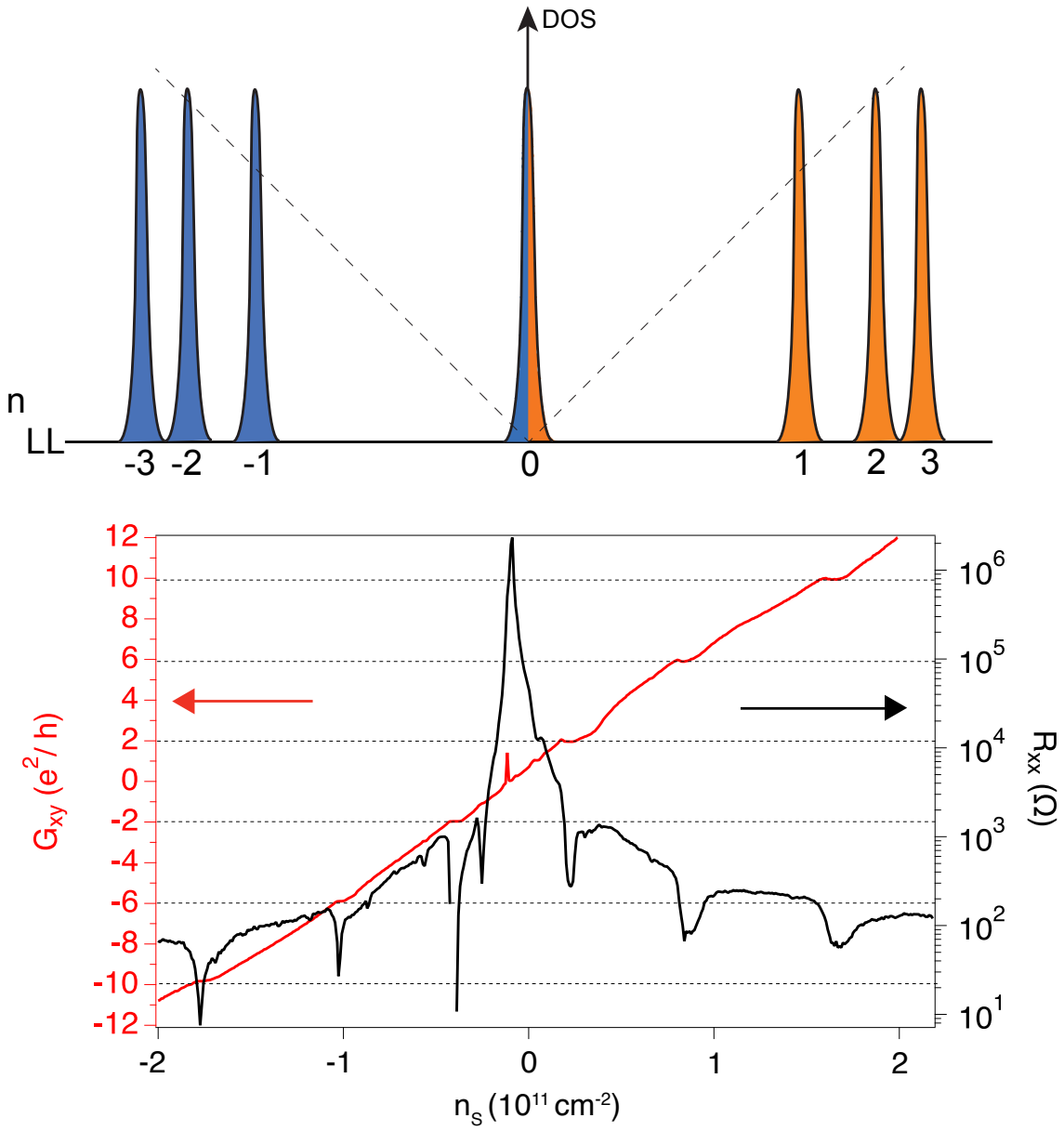

Fig. 1.2: (a) Density of states of single-layer graphene in zero magnetic fields is shown as a dashed line, illustrating the linear energy dependence. When the field is turned on, the continuum of energy is quantized into a series of particle-hole symmetric Landau levels. The filled colors indicate electrons (orange) and holes (blue). (b) Longitudinal resistance R_{xx} and Hall conductance G_{xy} as a function of carrier density at B = 8T, T = 4K. Half-integer quantum Hall plateaus at $G_{xy} = \nu e^2/h$ are observed for filling factor $\nu = \pm 2 \pm 6 \pm 10$

$\omega_c\tau \gg 1$, where τ represents the scattering time, meaning that the carriers should complete at least one cyclotron orbit between scattering events.

In crystalline structures, the absence of spherical symmetry results in inherent anisotropy [20]. This crystalline anisotropy can be quantified using an effective mass tensor, which is expressed as:

$$\left(\frac{1}{m^*}\right)_{ij} = \frac{1}{\hbar^2 k}\frac{\partial E}{\partial k_i \partial k_j}. \tag{1.21}$$

Thus, determining m^* for a given relative orientation of the crystal and B-field facilitates understanding the low-energy band structure. Due to crystalline anisotropy, the cyclotron mass m_c is not always the same as the effective mass $m*$, but they are approximately close in practice.

CR absorption spectra of a material are typically obtained by varying either the magnetic field strength or the frequency of the electromagnetic field. Plotting the cyclotron frequency ω_c against the magnetic field strength facilitates the determination of the effective mass of the particle. This information is essential for comprehending the behavior of Bloch electrons within a restricted-energy and wavenumber range in crystalline solids. Therefore, CR acts as a powerful spectroscopic probe of the electronic structure of conducting materials [21]. This methodology was particularly instrumental in early CR studies on semiconductors like Si and Ge [22] and continues to be valuable for newer materials.

The application of CR to two-dimensional electron gases (2DEGs) ushered in a new era, with its utility expanding to material systems such as GaAs/AlGaAs heterostructures [23, 24]. CR offers insights complementary to electronic transport, especially when the Fermi energy lies within a cyclotron gap. For instance, while transport probes only the edge states of a quantum Hall system, CR allows for the direct investigation of Landau levels (LLs) throughout the bulk of the material.

Traditionally, CR measures a single resonance for a given sample and field orientation, determining the charge carrier effective mass, a fundamental property of the band structure. However, the linear and particle-hole symmetric dispersion of graphene introduces a myriad of new inter- and intra-band resonances spanning a wide range of energies [25]. In graphene, the ease of controlling the charge carrier density (or Fermi level) allows for precise control over which transitions are active, facilitating clear assignment to specific levels of the electronic structure. Importantly, unlike traditional materials with parabolic dispersion, CR energies in graphene are inherently sensitive to contributions from electron correlations [26]. Therefore, CR spectroscopy presents a novel opportunity to explore interaction-induced physics [27] in graphene and beyond, constituting a primary aim of this thesis.

To discuss the interaction of light with graphene in the presence of a quantizing magnetic field, we return to the tight-binding Hamiltonian at the K point and rewrite it in terms of kinetic energy momentum $\pi = \mathbf{p} + e\mathbf{A}$, this yields

$$H_\xi = \frac{1}{2m}(\mathbf{p} + e\mathbf{A})^2 = \frac{1}{2m}\left({\pi_x}^2 + {\pi_y}^2\right), \tag{1.22}$$

If we define the ladder operators for the total momentum of the system as

$$\hat{a}_\pm = \frac{l_B^2}{\sqrt{2\hbar}}\left(\pi_x \pm i\pi_y\right), \tag{1.23}$$

where $\hat{a}_\pm$ are creation and annihilation operator satisfying the condition $[\hat{a}_+, \hat{a}_-] = 1$. In

addition to the usual commutation relations

$$[x, p_x] = [y, p_y] = i\hbar, \tag{1.24a}$$

$$[x, y] = 0, \tag{1.24b}$$

$$[p_x, p_y] = 0, \tag{1.24c}$$

we find that in contrast to the components of the canonical momentum, the components of the kinetic momentum do not commute with each other in the presence of a magnetic field.

$$[x, \pi_x] = [y, \pi_y] = i\hbar, \tag{1.25a}$$

$$[x, \pi_y] = [y, \pi_x] = 0, \tag{1.25b}$$

$$[\pi_x, \pi_y] = \frac{i\hbar^2}{l_B^2}. \tag{1.25c}$$

When we apply a far-infrared light to the system, the Hamiltonian gains a perturbing term $\mathbf{A}'$. In the electric dipole approximation, the time-varying electric field given by

$$\mathbf{A}_{\pm}^{'} = \frac{\mathcal{E}_0}{\sqrt{2}i\omega} \left(\hat{e}_x \pm \hat{e}_x\right) e^{-i\omega t}, \tag{1.26}$$

where $\mathbf{A}_{\pm}^{'}$ represents the right- or left-handedness of the circularly polarized light with frequency ω. Substituting the latter operators to the Hamiltonian in (1.22) and adding (1.26) as perturbation we find

$$\mathbf{H} = \frac{1}{2m^*}\left(\mathbf{p} + e\mathbf{A} + e\mathbf{A}_{\pm}^{'}\right)^2 \approx \frac{1}{2m^*}\boldsymbol{\pi}^2 + \frac{e}{m^*}\boldsymbol{\pi}.\mathbf{A}_{\pm}^{'} = H_{\xi} + H_{\xi}^{'}, \tag{1.27}$$

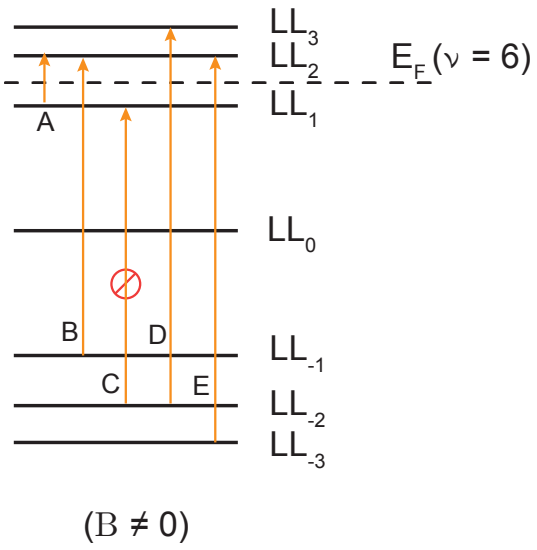

Fig. 1.3: The Landau level spectrum of graphene, with the Fermi level between first and second LLs. One intraband and four interband transitions demonstrate a selection rule $= |n_{\text{final}}| = |n_{\text{initial}}| = \pm 1$ Transition "C" is not allowed because all the levels are filled.

where $H_\xi^{'}$ can be written in terms of ladder operators as

$$H_\xi^{'} = \frac{e}{m^*}\left(\pi_x \mathbf{A}_{\pm,\mathbf{x}}^{'} + \pi_y \mathbf{A}_{\pm,\mathbf{y}}^{'}\right) = \frac{-e\mathcal{E}_0}{\sqrt{2}im^* l_B}\left(\pi_x \pm i\pi_y\right) e^{-i\omega t} = \frac{-e\hbar\mathcal{E}_0}{i\omega m^* l_B}\hat{a}_\pm e^{-i\omega t}. \tag{1.28}$$

We observe that electromagnetic radiation of frequency $\omega = \omega_c$ is detectable from charges undergoing cyclotron motion, inducing transitions $n \to n+1$ across Landau levels (LLs). The diagram in Fig. 1.3 illustrates optically active transitions in monolayer graphene for Fermi energy E_F lying between $N = 1$ and $N = 2$. In parabolic systems, the lowering operator associated with the perturbation typically corresponds to raising a hole by one LL (e.g., $N = -1 \to N = -2$). However, in graphene, this lowering operator can also facilitate the lowering of an electron by one LL while simultaneously raising its energy, enabling interband transitions e.g., $N = -3 \to N = 2$ (transition "E" in Fig. 1.3). We explore

several implications derived from equations 1.27 and 1.28: due to electron-hole symmetry, the wavefunctions of positive and negative Landau level (LL) states are identical, allowing dipole-allowed inter-LL transitions in graphene following the selection rules $|n| \rightarrow |n|+1$ and $|n| \rightarrow |n|-1$. These transitions can be categorized into three groups ($j \geq 1$). Firstly, allowed inter-band resonances:

$$\begin{cases} LL_{-j} \rightarrow LL_{j+1} \\ LL_{-j-1} \rightarrow L_j \end{cases} \quad \text{at} \quad E = v_F\sqrt{2\hbar eB}(\sqrt{j+1}+\sqrt{j}), \tag{1.29}$$

where j represents the LL index $\neq 0$. Secondly, allowed intra-band resonances:

$$\begin{cases} LL_{j} \rightarrow LL_{j+1} \\ LL_{-j-1} \rightarrow LL_{-j} \end{cases} \quad \text{at} \quad E = v_F\sqrt{2\hbar eB}(\sqrt{j+1}-\sqrt{j}). \tag{1.30}$$

Lastly, mixed $LL_{-1(0)} \rightarrow LL_{0(1)}$ resonance, involving the $n = 0$ LL, having energy $v_F\sqrt{2\hbar eB}$. Therefore, graphene exhibits a rich, multi-mode magneto-optical response [28]. Cyclotron resonance is often used interchangeably with Landau level spectroscopy where the energies of individual resonances, corresponding to inter-LL transitions, scale as $\sqrt{B}$, thus preserving the unique property of the non-equidistant ladder of LLs in graphene.

1.2.1 Many body effects and Kohn's theorem

While the properties of graphene discussed above can be understood within a non-interacting electron framework, the role of electron-electron interactions [29] remains crucial for a comprehensive understanding of the LL transition energies in cyclotron resonance measurements.

In 1961, Walter Kohn [30] showed that in a translationally invariant system with Landau

quantized charge carriers interacting via the short-range Coulomb force U, electromagnetic radiation primarily interacts with the center-of-mass motion of the system. This interaction leads to excitations across Landau levels $N \rightarrow N+1$ at the cyclotron energy $\hbar\omega_c$. When we include the interaction term U into the Hamiltonian in equation1.28, the commutation relation $[H_\xi, \hat{a}_\pm] = \pm\hbar\omega_c$ remains unchanged. Therefore, the cyclotron resonance frequency remains unchanged, so the interactions play a negligible role in cyclotron resonance in parabolic systems [30–32].

Kohn's theorem can break down due to various factors like disorder and, in some cases, non-parabolic energy-momentum relations. The extreme nonparabolicity of the electronic spectra in graphene thus evades Kohn's theorem [27, 33–37], leading to deviations from Eq. 1.29 [28, 38–41], which opens up the opportunity to observe many-body corrections to cyclotron resonance, a phenomenon we experimentally investigate in Chapter 3 of this thesis.

Building upon prior work by Henriksen et al., [38] which established the breakdown of Kohn's theorem in the context of unusual Landau-level sequence in graphene, our research extends this investigation further. However, recent advancements within our lab have provided more deeper insights into this phenomenon. A nonmonotonic variation of the effective Fermi velocity of charge carriers in a magnetic field, mainly attributed to electron-electron interactions, was investigated in prior work [42] using magneto-optical spectroscopy. In a single-particle picture, the transitions energy between interband Landau levels in graphene are defined by

$$E_{mn} = v_F\sqrt{2e\hbar B}\left(\sqrt{|m|} + \sqrt{|n|}\right) \tag{1.31}$$

Here, m and n are indices for the initial and final levels, respectively, with $v_F \approx 10^6$ m/s representing the carrier Fermi velocity. However, the presence of electron-electron interactions introduces an additional term, $\delta E_{ee} = C_{mn}e^2/l_B$ [33, 34]. This term, also contingent upon

initial and final states, magnetic field strength, and the chemical potential (Fermi energy), poses a challenge in distinguishing between single- and many-particle contributions since $\delta E_{ee} \sim \sqrt{B}$ and $E_{mn} \sim \sqrt{B}$. To understand this complexity, its crucial to consider both the single-particle transition energy (E_{mn}) and the many-body contribution. The combined impact of these factors yields the total transition energy,

$$\Delta E_{mn}^{total} = \Delta E_{mn} + \delta E_{ee} = \frac{v_F^{ee}}{v_F} \Delta E_{mn}, \tag{1.32}$$

where the "effective" Fermi velocity $v_F^{ee} \geq v_F$ captures the interaction contribution. Consequently, any variation in v_F^{ee} at a constant field reflects changes arising from many-particle interactions. Cyclotron resonance acquires a qualitatively novel capability when employed in materials with non-parabolic dispersion. Given the well-defined single-particle Landau levels, cyclotron resonance spectroscopy allows for a quantitative assessment of the contribution of electron-electron interactions.

1.3 Graphene on hexagonal boron nitride

The electronic properties of two-dimensional materials such as graphene are extremely sensitive to their environment, especially the underlying substrates [43]. Initially, graphene on SiO_2 substrates served as a convenient entry point due to its visible optical contrast and ease of fabrication [44, 45]. However, the electronic quality of graphene/SiO_2 devices is often compromised by trapped charge impurities [46]. The advent of suspended graphene structures, achieved by substrate removal, marked a significant advancement, enabling device quality approaching ballistic transport [47]. Nevertheless, suspended configurations are mechanically fragile and lack flexibility in device architecture, adding complexity to fabrica-

tion processes. Hexagonal boron nitride (h-BN), similar to graphite, features atomically flat surfaces when exfoliated, with the lattice constants δ of the two materials differing only by 1.8%. Each h-BN layer consists of a hexagonal lattice of boron and nitrogen atoms. Unlike the covalent bonds in graphene, boron and nitrogen atoms form ionic bonds, resulting in a substantial band gap of approximately 6 eV. These unique properties position h-BN as an ideal substrate for graphene, leading to significant improvements in charge carrier mobility compared to devices on SiO_2. Since hBN has a similar lattice constant with graphene, when the two lattices are nearly perfectly aligned, interactions between the crystals significantly alter the graphene band structure. This opens an avenue for studying interesting phenomena, such as the Hofstadter quantization, and provides a route to make graphene insulating, which we will discuss further in the following section.

1.3.1 Graphene/h-BN moiré superlattice

Stacking two-dimensional crystals with identical Bravais lattice structures can result in the emergence of new large-scale periodicity [48–50]. This arises from the crystallographic alignment and the mismatched lattice constants, leading to a topographic moiré pattern. The h-BN lattice acts as a long wavelength electrostatic potential modulation for the electron states in graphene. Given the lattice mismatch δ between h-BN and graphene, the relative rotational angle θ between the two lattices uniquely determines the moiré wavelength λ as [48],

$$\lambda = \frac{(1+\delta)a}{\sqrt{2(1+\delta)(1-\cos\theta)+\delta^2}}, \tag{1.33}$$

where a is the lattice constant of graphene. Due to lattice mismatch, there is a moiré pattern for all orientations of graphene on h-BN with a maximum possible length of about 14 nm (for $\theta = 0°$). A visual illustration of the graphene/h-BN moiré pattern is shown in Figure

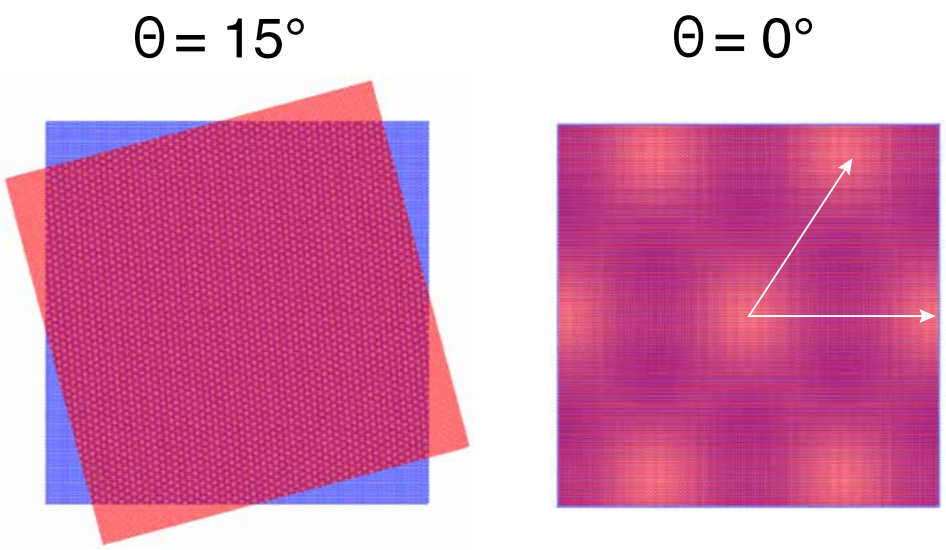

Fig. 1.4: Moiré patterns in graphene/h-BN heterostructures for two different rotational alignments. The lattice mismatch between G and h-BN leads to the formation of moiré patterns for all rotational alignments. Notably, the moiré pattern reaches its maximum length for perfect alignment (0°), highlighted by dashed line.

1.4 for two different rotational alignments.

As the lattice length scale increases, the electronic matter wave propagates at a longer wavelength on the lattice, which corresponds to a lower momentum. Since the kinetic energy of electrons is linear in momentum, the reduced momentum on the superlattice implies a reduced kinetic energy. This makes the interaction energy relatively more important than the kinetic energy, resulting in enhanced interaction among the electrons.

The key effects of the h-BN substrate on the electronic structure of graphene can be summarized by two points. Firstly, the atomic-scale modulations break the local symmetry between the graphene sublattices, influenced by the potential difference between boron and nitrogen atoms in h-BN. In our study, we investigate CR measurements conducted on high-quality graphene devices, presenting the first observation of the complete lifting of four-fold degeneracy of Landau levels due to broken spin and valley symmetries using

magneto-spectroscopy. Secondly, perfect crystallographic alignment of two lattices gives long wavelength moiré pattern that introduces a λ-scale modulation of the graphene-hBN coupling, forming a smooth superlattice potential. The superlattice length scale provides access to the Hofstadter butterfly phenomenon, which we will discuss further in the following section. Our work in this thesis reports cyclotron resonance measurements in the Hofstadter butterfly regime in graphene/h-BN superlattices.

1.4 Hofstadter's butterfly

Hofstadter solved the energy spectrum of electrons in commensurate lattices [51] where he treated the electrons as idealized "Bloch electrons", which means they do not interact with each other and move in a periodic electric potential commensurate with the lattice. The butterfly-like pattern visible in Figure 1.5 originates from the nested self-similar fractal structure of the energy spectrum of electrons. It arises due to the interplay of two characteristic length scales in the problem: magnetic length l_B and the lattice constant a of the lattice. The conditions for observing fractals are met when the magnetic flux $\Phi = BA$ is as large as the magnetic flux quantum $\phi_0 = h/e$ and their ratio takes on rational values:

$$\Phi = \frac{p}{q}\phi_0 \tag{1.34}$$

where p and q are co-prime integers. However, the lattice spacing is considerably smaller for most materials than the magnetic length scales, necessitating extraordinarily high magnetic field values to fulfill this criterion. For instance, with a lattice constant of approximately 2 Å, the condition for observing the fractals is met only at magnetic field values as high as 10,000 T. To address this, Hofstadter proposed that one could synthetically create materials with

relatively larger lattice spacing to realize this self-recursive structure at an experimentally attainable magnetic field.

When two isostructural crystals with a slight lattice mismatch are placed on top of each other with an alignment angle θ between their respective crystal directions, the interaction between their crystalline periodicities generates a large-scale modulation of their local stacking, termed the moiré superlattice. The advent of graphene rapidly sparked interest in graphene superlattices. The principal novelty of such superlattices is in the Dirac-like spectrum and the fact that charge carriers are not buried under the surface, which allows for a relatively strong superlattice potential on the nanometre scale. One promising approach to creating nanoscale graphene superlattices involves inducing a potential through another crystal. When graphene is placed on top of h-BN, it exhibits a moiré pattern, with a maximum wavelength of 14 nm for perfect alignment; thus, it is well suited to access the Hofstadter physics at lab scale magnetic field [52].

1.4.1 Hofstadter effect in a square lattice

Harper [53] investigated the effect of conduction electron subject to a uniform magnetic field in a 2D square lattice with lattice constant a. Generalized tight-binding Hamiltonian for a single particle on a 2D square lattice subjected to a magnetic field is defined as

$$\hat{H} = \frac{\left(\hat{p} - e\vec{A}/c\right)^2}{2m} + U(\vec{r}). \tag{1.35}$$

The Hofstadter original spectrum arises from injecting the full canonical momentum operator, $\mathbf{p} + e\mathbf{A}$, under perpendicular magnetic field into the single band Bloch energy function,

$W(\vec{k})$, for a cubic lattice, given by

$$W(\vec{k}) = 2E_0(\cos(k_x a) + \cos(k_y a)) = E_0(e^{ik_x a} + e^{-ik_x a} + e^{ik_y a} + e^{-ik_y a}). \tag{1.36}$$

Utilizing Peierl's substitution, the Bloch energy function $W(\vec{k})$ for a cubic lattice is transformed into an effective Hamiltonian. Under the Landau gauge $\vec{A} = eBx\hat{y}$, the tight binding Hamiltonian can be written as:

$$\hat{H} = E_0 \left(e^{\frac{i\hat{p}_x a}{\hbar}} + e^{\frac{-i\hat{p}_x a}{\hbar}} + e^{\frac{ia}{\hbar}(\hat{p}_y - eBx)} + e^{-\frac{ia}{\hbar}(\hat{p}_y - eBx)} \right). \tag{1.37}$$

The translation operators $e^{-i\vec{x}.\hat{p}/\hbar}$ act on the 2D wavefunction $\psi(x, y)$. The Schrodinger equation, $\hat{H}\psi(x, y) = E\psi(x, y)$ can be rewritten as

$$E_0 \left(\psi(x + a, y) + \psi(x - a, y) + e^{-i\frac{e}{\hbar}aBx}\psi(x, y + a) + e^{i\frac{e}{\hbar}aBx}\psi(x, y - a) \right) = E\psi(x, y). \tag{1.38}$$

This equation establishes a link between the wavefunction, $\psi(x, y)$, and its neighbors a full lattice period away. Facilitating the substitution $(x, y) = (na, ma)$ for further analysis gives a solution to the wavefunction of the form $\psi(ma, na) = e^{i\nu n}g(m)\alpha$. For a single particle in a 2D lattice in the presence of a magnetic field, the Schrodinger equation transforms into Harper's equation of the form:

$$g(m + 1) + g(m - 1) = [\epsilon - 2\cos(2\pi m\alpha - \nu)]g(m). \tag{1.39}$$

Here $\epsilon = E/E_0$ is normalised energy and

$$\alpha = \frac{e}{hc}a^2 B = \frac{\Phi}{\phi_0}, \tag{1.40}$$

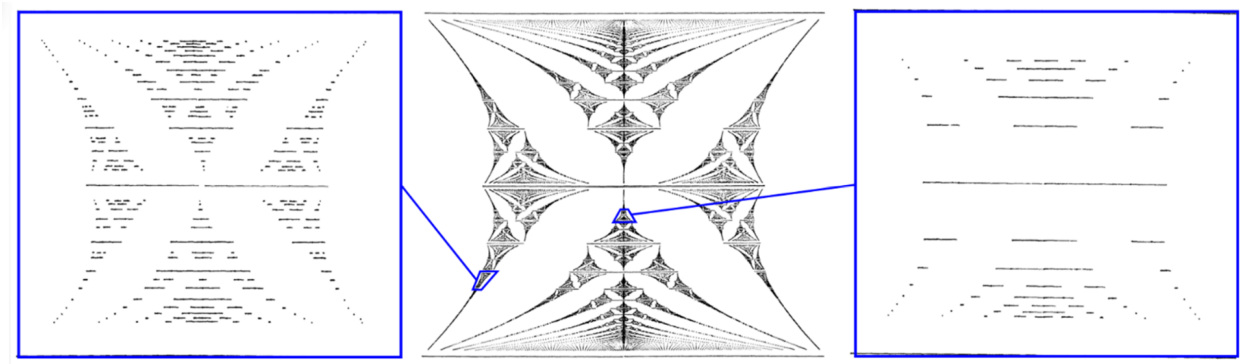

Fig. 1.5: The plot depicts a unit cell of the fractal spectrum, containing within it sub-cells that are equivalent of the entire cell itself. Two of these sub-cells are expanded and rectangularized to highlight their self-similarity [51].

is dimensionless, being the ratio of flux through a lattice cell to one flux quantum. Here, $\Phi = Ba^2$ is the magnetic flux per unit cell for a square lattice, and ϕ_0 is the magnet flux quanta. Hofstadter solved Harper's equation for rational values of $\alpha = p/q$, where p and q are co-prime integers. Energy spectrum calculated by Hofstadter at magnetic fields corresponding to $\alpha = p/q$, q contains q distinct block bands as shown in Figure 1.5 adopted from Hofstadter's original publication [51]. Beyond the inherent mirror symmetries within the spectrum, certain segments display resemblances to others. The unit cell is composed entirely of these smaller "sub-cells" each of which mirrors the entire spectrum (and each other). Consequently, these sub-cells contain additional sub-cells indefinitely. This recursive nesting structure, infinitely dense, forms a fractal set of spectrum.

Wannier provides a simplified description of the Hofstadter energy-field diagram using a density-field diagram. In Figure 1.6a, red and blue lines along the diagonal denote wide gaps of forbidden energies in the Hofstadter's spectrum, interrupted at $\Phi/\phi_0 = 1/2 = p/q$. Secondary gaps emerge for $q > 3$ and $q > 4$, marked by pink and blue lines; these gaps do not close for higher values of q [54].

In Figure 1.6b, the line plot by Wannier addresses the issue of rationality by focusing on

the gaps in Hofstadter's spectrum, marked by colored lines in Figure 1.6a. Wannier discovered that by replacing the energy axis ε with the cumulative weight W of four subregions separated by diagonal lines in Hofstadter's spectrum, regions bounded by gaps or bands would collapse into straight lines [54]. This transformation converts the gaps in Hofstadter's energy spectrum into a network of straight lines shown in Figure 1.6b.

However, Wannier acknowledged that such simplification comes at a cost. He stated, "A simplification of this sort cannot be accomplished without certain loss. There is first an aesthetic loss, but there's also a loss of information", as the description no longer contains the actual value of the energy but only its location in terms of input parameters and quantum numbers. Nevertheless, assigning a constant energy value to each section of Hofstadter's spectrum may provide a reasonable approximation.

While Hofstadter's butterfly represents the energy-field diagram, Wannier's spectrum represents the density-field diagram. The Wannier diagram can be experimentally accessed through transport measurements, as it parameterizes the problem by W and α, quantities proportional to experimental parameters such as carrier density and magnetic field strength.

Moon and Koshino [55] theoretically investigated the electronic spectrum within moiré superlattices formed by monolayer graphene stacked on an h-BN layer, examining various rotational angles in a magnetic field. Their investigation revealed a hierarchical self-similar structure in the energy spectrum under conditions of perfect alignment. Notably, at low magnetic fields, the spectrum mirrors that of pristine graphene, while at higher fields, pronounced reconstruction occurs, yielding nested self-similar Landau levels.

Given that Wannier's simplified description loses information about the associated energies of the gap, which has been widely measured with transport probes, theoretical investigation of the optical properties of the graphene-h-BN lattice strongly motivates our work to probe the self-similar energy-field diagram employing cyclotron resonance measure-

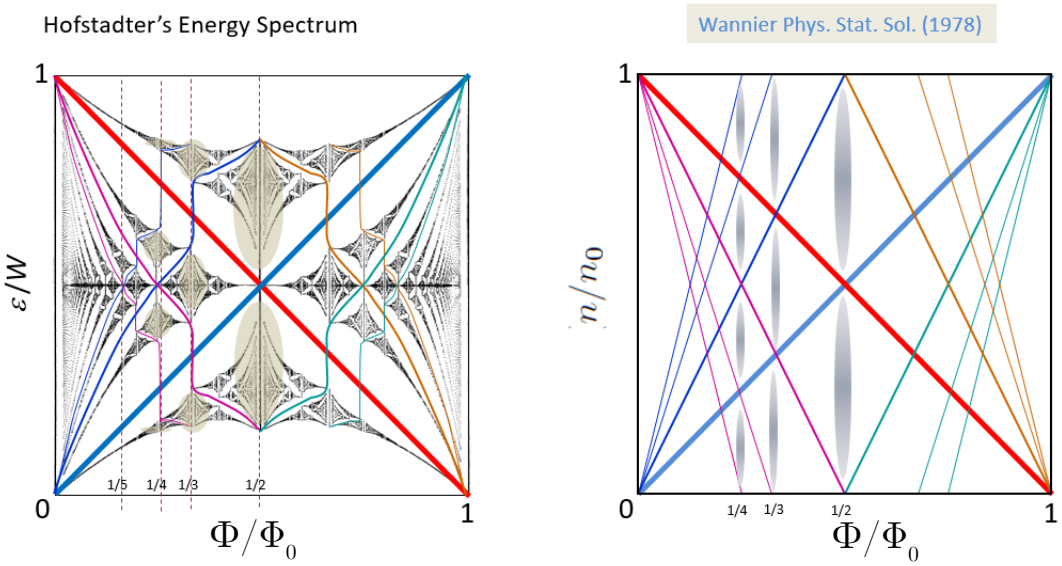

Fig. 1.6: Left is the Hofstadter Butterfly spectrum, calculated for a square superlattice. The right image shows the Wannier spectrum plotted as normalized carrier density versus magnetic field [52].

ments. In this thesis, we experimentally investigate these fractal levels using magneto-optical spectroscopy, measuring optical transitions across the reconstructed Landau levels in the graphene/h-BN moiré superlattice in Hofstadter's butterfly regime.

1.5 Overview of this work

The remaining sections of this dissertation are organized as follows:

Chapter 2 presents a system capable of conducting broadband far-to-mid-infrared CR spectroscopy in magnetic fields up to 14 T and temperatures down to 0.1 K. The infrared detector plays a central role in spectroscopic measurements, detecting changes in the spectral radiance of the incoming radiation. In this work, we provide a comprehensive overview of the development and integration of the 1.6 K Far-IR detector setup.

Chapter 3 explores the infrared cyclotron resonance in a high-quality graphite-gated

monolayer graphene device to investigate the interplay of many-particle interactions and broken symmetries.

Chapter 4 presents CR measurements in the Hofstadter butterfly regime in G/h-BN superlattices to investigate the reconstructed LLs in moiré modulated graphene.

In Chapter 5, we report on infrared spectroscopy measurements of Landau-level transitions in dual-gated bilayer graphene and discuss possible future research directions that can be explored using the spectroscopic technique.

Finally, Appendix A describes the details of the infrared measurement setup, outlining the operation of the dilution fridge in the specific configuration when setting up the infrared measurement. Appendix B discusses the nano-fabrication technique we perform to turn layered vdW materials into measurable devices.

Chapter 2

Confocal Optics for Broadband Infrared Spectroscopy below 1K

Fourier-transform infrared (FTIR) spectroscopy and magneto-spectroscopy have played pivotal roles in understanding the band structure and charge transport mechanisms in metals and semiconductors [56, 57]. While these techniques are commonly applied at temperatures as low as liquid helium temperatures (∼4 K) and even at the boiling point of ^{3}He (∼0.3 K), the exploration of many correlated electron phenomena requires even lower temperatures achievable in dilution refrigerators. These phenomena include fractional quantum Hall effects, exotic forms of superconductivity, and spin liquid physics, among others [58, 59]. Although some of these systems have been investigated using infrared spectroscopy [60], the lowest temperatures routinely achieved often must be increased to access the most intriguing physics. The challenge arises from the limited cooling power and heat capacities of samples at lower temperatures, making the introduction of broadband infrared radiation detrimental to experiments.

In this chapter, we describe a system that enables broadband far- to mid-infrared spectroscopy in magnetic fields up to 14 T and sample temperatures down to 0.1 K. Pairs of back-to-back parabolic reflectors are placed in the optical path of an infinity-focused broad-

band infrared beam. The reflectors share a common focus, so they admit infinity-focused infrared light into the well-thermally-shielded interior of a cryogen-free dilution refrigerator cryostat while rejecting the majority of off-axis thermal radiation. This enables broadband spectroscopy of atomically thin materials across the far- and mid-infrared regime at very low sample temperatures.

At the core of these measurements lies the infrared detector, which detects changes in the spectral radiance of the incoming radiation. Throughout our work, we utilized two distinct infrared detectors: a 4.2 K high-res bolometer for the measurements discussed in Chapter 3 and a 1.6 K Far-IR bolometer for those in Chapter 4. However, the previously deployed 4.2 K bolometer, after nearly a decade of operation, experienced significant degradation in its performance and ultimately failed due to prolonged operation and exposure to multiple magnetic field quenches. This chapter describes modifications to address this issue, including designing and implementing a new detector module with a robust readout electronic circuit. This approach resulted in a seven-fold improvement in the signal-to-noise ratio of our spectroscopic measurements. Herein, we provide a comprehensive overview of the development and integration of the new detector setup.

2.1 Broadband Infrared Spectroscopy

Our FTIR magneto-spectroscopic setup, shown in Figure 2.1C and D, is based on a precision Bruker Vertex 80v FTIR spectrometer coupled with a closed cycle dilution refrigerator (DR) that houses a 14 T cryogen-free superconducting magnet. Figure 2.1d shows the optical beam path starting with a home-built beam-shaping box containing a set of moveable off-axis parabolic mirrors. These refocus the diverging beam that exits the spectrometer, enabling the beam to travel the $\sim$ 2 m to the sample without losing intensity. An off-axis parabolic mirror

re-routes the light into the DR through a transparent window (either KBr or polyethylene), where it is focused to the sample by a parabolic mirror and afterward defocused to continue traveling up to where a compound parabolic collector gathers the light for detection by an infrared detector. The sample stage is in the bore of a 14 T magnet (not shown). The design goal for our magneto-optical setup is to direct the light out of an FTIR spectrometer into a cryostat. The design overcomes several critical challenges, including (1) rejecting background radiation to operate the system at millikelvin temperatures using back-to-back parabolic cones, (2) geometric filtering that allows for focusing the light on sampling with a typical linear dimension of $\sim$ 10 um and extracting a sizeable optical response (3) minimizing heat load on the magnet to achieve maximum field up to 13 T and (4) simultaneously performing standard transport measurements on gate (carrier density) tuned high-quality 2D devices.

The spectrometer generates broadband infrared radiation using a globar light source, a silicon carbide filament operating at 1370 K under vacuum. This light travels through a Michaelson interferometer. The spectrometer has a step-scan mirror on a delay stage to modulate the incoming light, allowing the mirror to move in discrete steps repeatedly. This movement creates a time-dependent modulation of light of all wavenumbers, $\bar{\nu} = 1/\lambda$ in the spectrometer. The precision of an FTIR spectrometer hinges on the accuracy of the scanning speed of the mirror. The sum of the modulated light leaving the interferometer as a function of mirror position creates an interferogram shown in the inset in Figure 2.2a.

At the center of the interferometer resides a beam splitter, which we choose accordingly based on the spectral range of interest. In this study, we employ two types of beamsplitters: a potassium bromide (KBr) beamsplitter for the mid-IR range and a multilayer mylar beamsplitter for far-IR applications. This combination, paired with the optical window, whether it be another KBr crystal or a sheet of white polyethylene, facilitates selecting the appropriate spectral range for the experiment. Typically, the spectral range spans from 6 to 90 meV

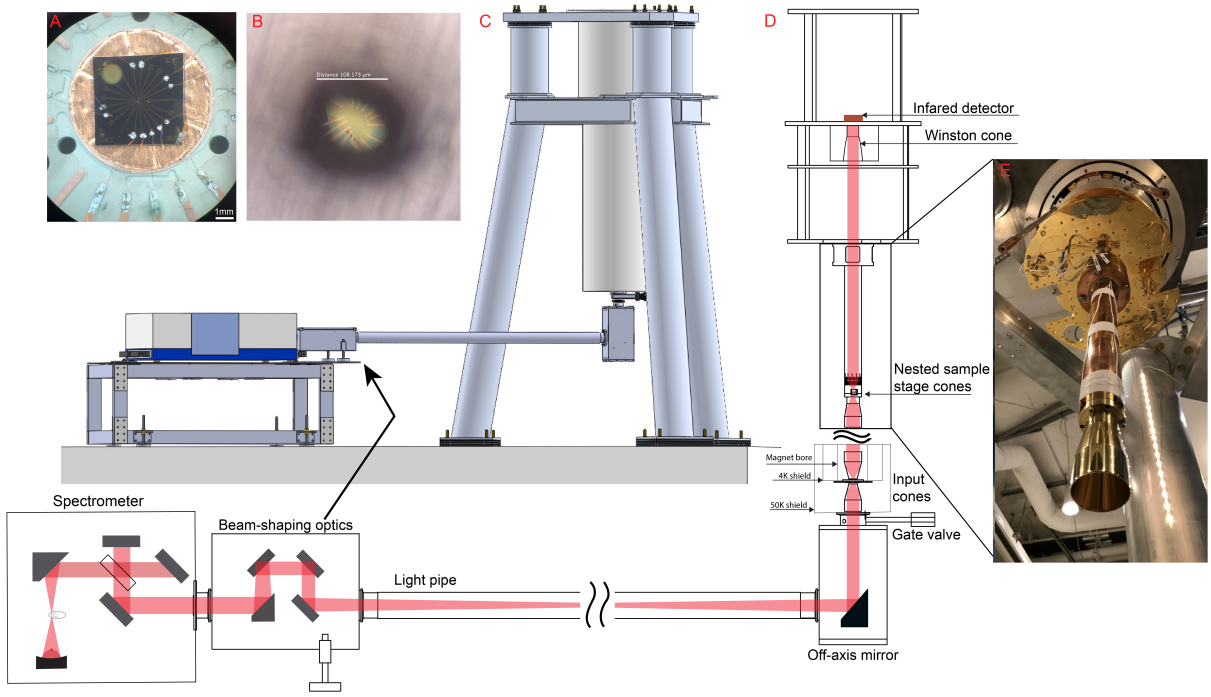

Fig. 2.1: A. Finished device wired to the sample mount and placed on a copper foil bottom aperture. B. Optical image of the device as viewed through ~ 90 μm top aperture. C. Schematic of the infrared magnetospectroscopy setup made using computer-aided design. D. Beam propagation through different components of the optical setup. E. Bottom view of infrared sample stage with a suspended copper tube holding the top stage cone.

for the far-infrared (FIR) region and 60 to 930 meV for the mid-infrared (MIR) region.

The interferogram is Fourier transformed and plotted as a raw transmission signal as a function of the wavelength of the light. Figure 2.2 illustrates typical raw transmission spectra measured in two different spectral ranges, where $1/\lambda$ is converted to energy scale in meV. As part of our ongoing efforts to enhance measurement capabilities, we incorporate a diamond window into our setup, providing access to the entire spectral range from FIR to MIR, eliminating the need to switch between optical windows.

The spectrometer is placed at a 2 m distance from the cryostat to protect the electronics inside the spectrometer from any stray magnetic field. After leaving the spectrometer, the collimated beam of modulated light is redirected to focus it onto a sample that lives inside the DR. The optical design resembles a telescope with unity magnification, directing the light from the spectrometer to the base of the DR. The near-collimated light exiting the spectrometer is brought to an intermediate focus roughly halfway between the spectrometer and the cryostat inside a guiding tube. This is achieved using a custom off-axis (OAP) gold-coated paraboloidal mirror with a 1m focal length. To re-collimate the light before it enters the DR, an identical OAP is positioned at the base of the cryostat to change the axis of light from horizontal to vertical. To avoid absorption of infrared light due to atmospheric gases, the spectrometer operates under a vacuum of $\sim$ 1 mbar, while the DR operates under a high vacuum of $\sim e^{-6}$ mbar. This set of two vacuum chambers is separated by an infrared transparent optical window. Additionally, a pneumatically operated gate valve is mounted at the base of the DR, allowing it to be completely isolated from the external optics while cooling it down to base temperature and pressure.

Cyclotron resonance is a bulk effect, with a signal proportional to the sample area. One of the primary concerns of the spectroscopic measurement is the macroscopic size of a typically exfoliated graphene sheet. Traditionally, cyclotron resonance measurements are conducted

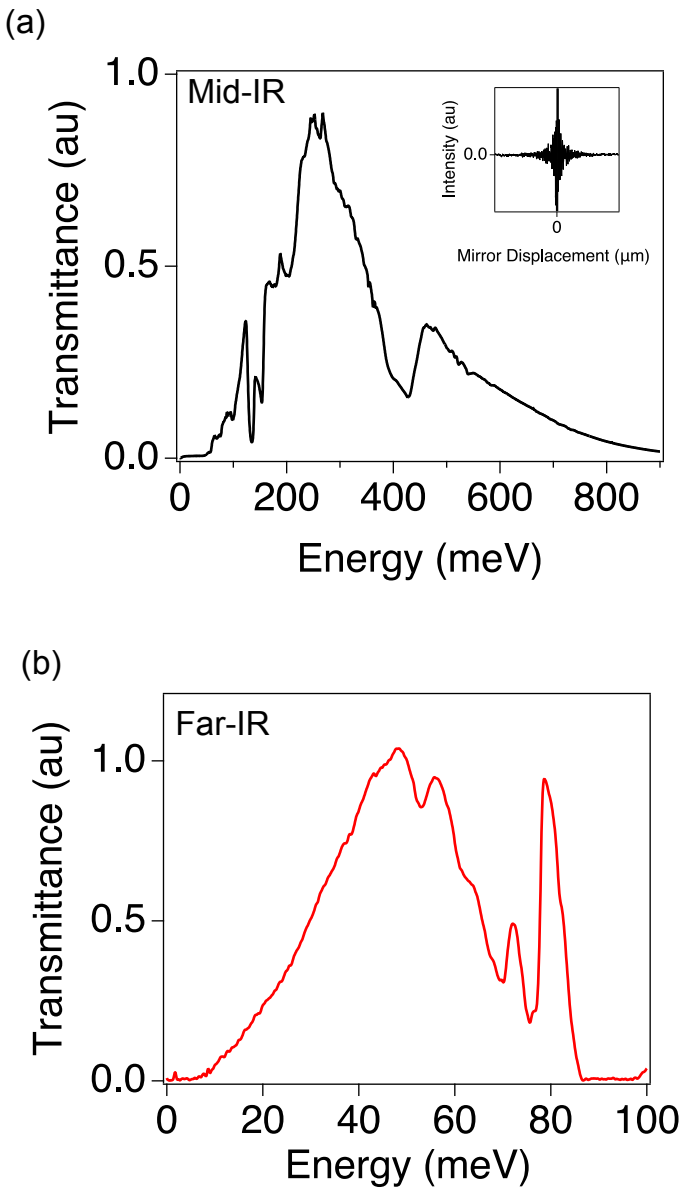

Fig. 2.2: (a) Raw transmission collected in mid-infrared (MIR) range using a KBr beam splitter and KBr optical window. The transmission data shows a sharp absorption feature at $\approx$ 130 meV from thermal oxide (SiO_2) on the Si substrate. The inset shows the typical interferogram, which is characteristic of a broadband light source. The large signal seen at zero mirror displacement, or zero path difference (ZPD), occurs when all wavelengths of the light source inside the spectrometer interfere constructively. (b) Raw transmission collected in the mid-infrared (FIR) range using a mylar beamsplitter and polyethylene optical window.

on samples with characteristic lengths of a few millimeters, where the sample size does not constrain transmission of the incident light. It is difficult to obtain a focal spot the size of our graphene samples, typically a few microns in length. The requirement of focusing a 40 mm diameter beam to a point 1 mm across is achieved using nested parabolic cones. We employ a small aluminum aperture on the sample to further focus the beam down to several hundred microns to block extraneous light. An optical microscope image of the device as seen through a 100-micron aperture is shown in Figure 2.1B.

2.1.1 Nested parabolic reflectors and beam propagation

The sample stage consists of two nested paraboloid cones, referred to as sample stage cones, aligned along the same axis but facing opposite directions. These cones intersect to form a reflective surface [61] and share a common focal point. As illustrated in Figure 2.1E, the hollow oxygen-free copper tube, attached to the mixing chamber plate of the DR, suspends the sample stage cone assembly to ensure precise alignment of its focal point with the center of the bore of the magnet. Moreover, the top cone integrates the necessary wiring for electronic transport measurement.

Within the framework of ray optics, the paraxial light beam directed towards the bottom cone reflects and subsequently gets focussed at the diffraction-limited spot on the shared foci of two back-to-back parabolas. Then, the light rays hit the reflective surface of the top cone and exit the cone, maintaining a one-to-one mapping with the entering beam.

To allow infrared light into the DR, 2-inch diameter holes are cut into the radiation shield of the DR. Unwanted radiation entering the DR, either in the form of background radiation or non-paraxial light from the spectrometer, presents a significant challenge to maintaining mK temperature for measurements where the most interesting physics can be seen. Left

unaddressed, much of this unwanted light deposits onto the inner surface or underside of the bore of the magnet, limiting the maximum achievable magnetic field and overwhelming the cooling capacity of the DR. This problem is addressed by adding a second pair of nested back-to-back parabolic cones, referred to as the input cones installed on the 50 K shield. These cones converge at a shared focal point set at a 1mm aperture, dramatically reducing the radiative load by approximately $(50/300)^4 \approx 0.001$ compared to a 2-inch ($\approx 50.8mm$) hole. Moreover, external light enters solely through the aperture with intensity reduced by $(1/50.8)^2 \approx 0.0004$. With a smaller aperture and differential thermal sinking of the parabolas (connecting the top one to 4 K and the bottom to 50 K), we have achieved a temperature of $\sim$ 200 mK in the mixing chamber.

Mounted below the infrared detector, on the still plate of the DR (which sits at 0.8 K), is a compound paraboloidal concentrator, also known as the Winston cone shown in Figure 2.1D. It collects the light, which is nominally collimated by the top cone of the sample stage, over a distance of approximately 0.5 m. Achieving precise alignment of the optical components is paramount for optimal performance.

Figure 2.3 illustrates the ray-tracing simulation of the optical beam path inside the DR. As shown in Figure 2.3a, the paraxial light enters the input cones, representing the first stage of geometric filtering. When the apertures of the input cones are properly aligned, the light proceeds to subsequent focusing at the stage cones, where the sample is situated. Once the apertures of the sample stage cones are precisely aligned, the paraxial light is effectively collected at the Winston cone.

Conversely, Figure 2.3b illustrates the consequences of offset apertures at the input stage cones: the light bounces off the cones, failing to pass through the sample at the stage cones. In Figure 2.3c, with aligned input cones, a slight misalignment of approximately 1 mm of the sample stage cones can prevent the light from reaching the Winston cone. These scenarios

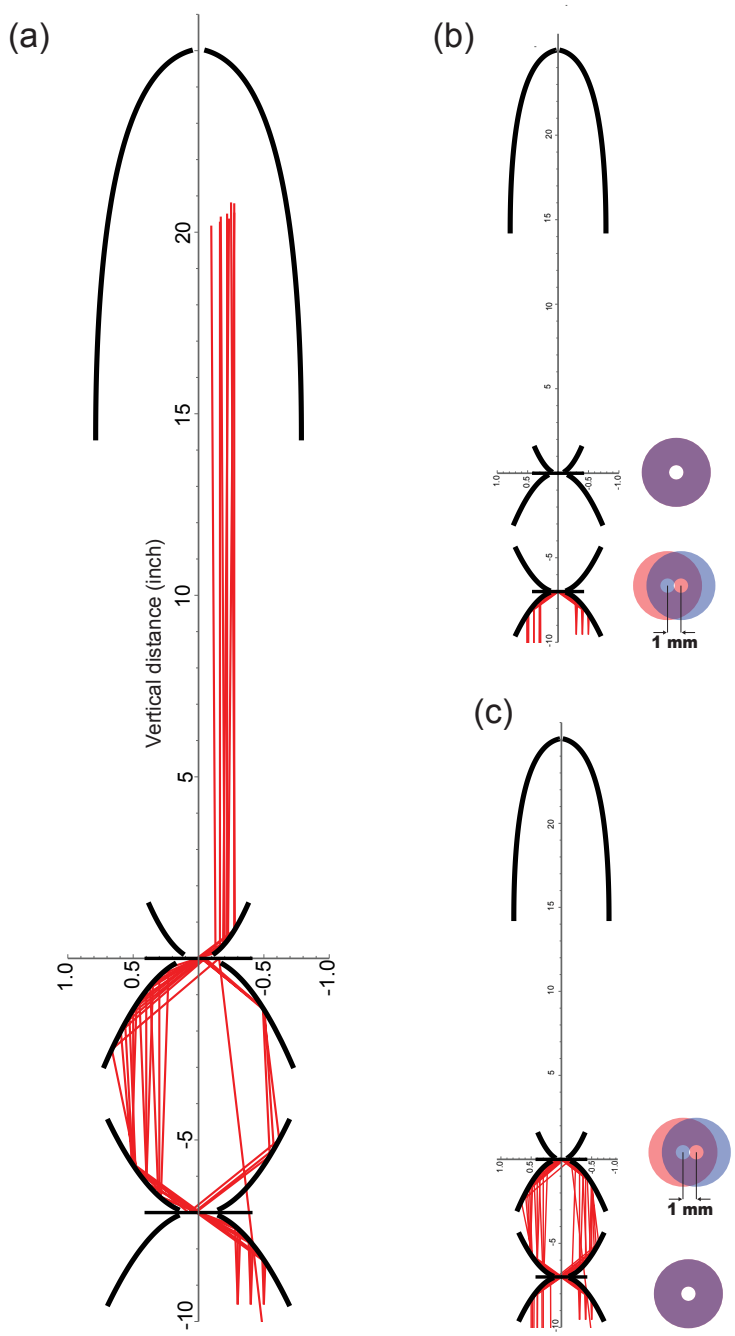

Fig. 2.3: (a) Paraxial light undergoes geometric filtering upon entering the input cones, focuses at the stage cones housing the sample, and is ultimately collected at the Winston cone. (b) With approximately 1 mm offset of the input cones, the light reflects off the cone and fails to reach the sample. (c) Paraxial light entering the input cones is hindered by a 1 mm misalignment at the sample stage cones, preventing it from reaching the Winston cone.

emphasize the critical importance of optical alignment, as even minor offsets can lead to a notable loss of signal detected by the detector, highlighting the significance of alignment at each stage along the optical path.

2.2 Infrared detector

The Winston cone condenses the collected collimated light to an infrared detector known as a bolometer, which accomplishes infrared detection. A typical bolometer is a temperature-sensitive resistor heated by incoming radiation and cooled by thermal conduction through its electrical lead wires. Any thermal radiation that impinges upon the detector causes a temperature change, subsequently altering its resistance. This change in resistance is then amplified and measured as a voltage difference. Since the bolometers measure a temperature change, the incident radiation must be modulated, which allows it to excite and relax. Thus, a measurement of the change in resistance corresponds to the energy of the incident radiation. Operating at 1.6 K, the bolometer covers a broad range of frequencies spanning mid- and far-infrared. It can detect less than a 1% change in the spectral radiance of a small amount of incident light. While the operating temperature of 1.6 K is provided by the manufacturer (IR labs), we conduct performance characterization of the detector to evaluate the optimum temperature for maximum response from the bolometer.

This section discusses the design and implementation of the custom-built bolometer module and readout electronics, intending to minimize the electrical and mechanical noise coupled to the infrared measurement. We engineered the module to replace the general-purpose 4.2 K bolometer previously utilized for spectroscopic measurements. Various factors, including electrical nonlinearities, optical load, thermal noise, Johnson noise, and noise in readout electronics, can compromise the sensitivity of bolometers. One frequently used figure of

merit is the noise equivalent power (NEP), which depends on its sensitivity (responsivity) and the noise sources in the bolometer readout circuit. Here, we discuss the performance characterization and noise analysis of the 1.6 K Far-IR bolometer to optimize its operation for the highest NEP. Additionally, we will highlight the improvements in spectroscopic measurements achieved with the new detector compared to the previous one.

2.2.1 Design considerations and readout electronics

Commercially available infrared detectors from IR labs are typically housed in a liquid helium dewar with a liquid nitrogen-cooled radiation shield and come with attached low-noise electronics. We have custom-built the bolometer housing and read-out electronics to integrate the bolometer into the DR. A key consideration in designing the bolometer module is protection from unwanted radiation, mainly from two sources: blackbody radiation from components within the DR and stray light reaching the detector from outside the cryostat. Additionally, the design of the thermal circuit for the bolometer readout considers incorporating sections held at different temperatures. Appendix A discusses more details of the wiring of the bolometer circuit inside the DR.

We design and machine the infrared detector mount in-house using oxygen-free high purity copper (OFHC), which we further electropolish and gold plate to ensure optimal thermal contact and low emissivity. The mount includes three plug-in SMP connectors for connections to the bolometer bias, the amplifier gate, and the cold ground. Additionally, it accommodates a dedicated heater and thermometer for independently heating the detector to the desired temperature. The heater consists of Nichrome (NiCr) wire wound non-inductively around copper bobbins with a total resistance of 16 Ω, able to heat the detector to its operating temperature. The thermometer is an in-house calibrated thick film

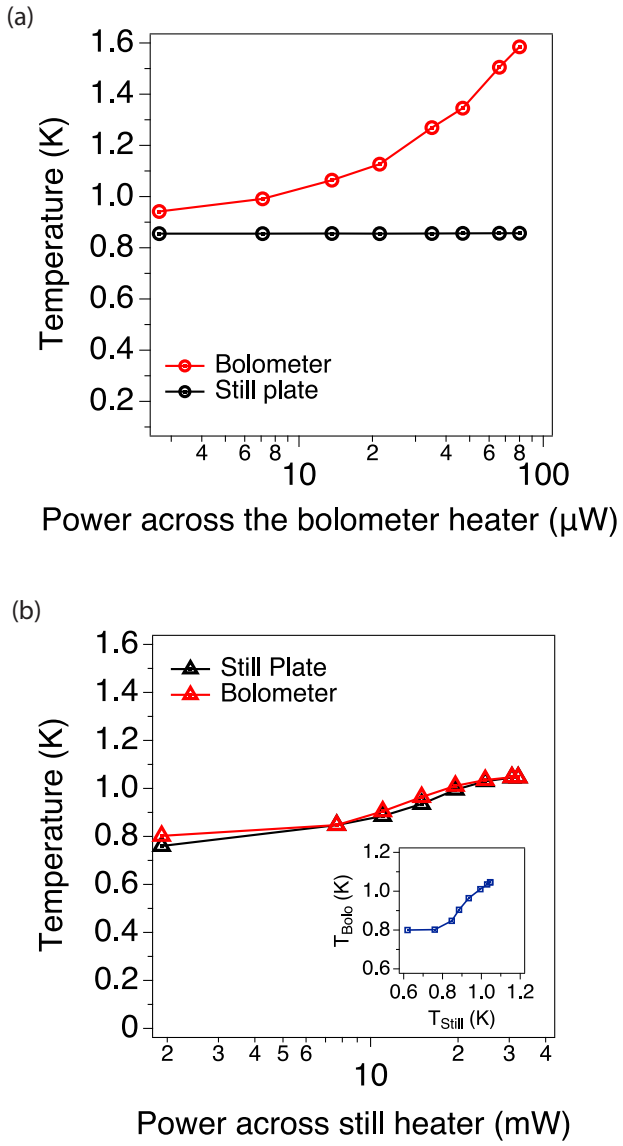

Fig. 2.4: (a) Temperature profiles of the bolometer and still plate in response to the heating of the bolometer housing. Notably, the base temperature of the still plate experiences minimal change, remaining within 1%. (b) As heat is applied to the still plate, the temperature of the bolometer and still closely track each other, indicating good thermal contact between the two. The inset demonstrates a linear increase in the temperature of the bolometer with the still plate.

chip resistor based on Ruthenium oxide (RuO_x) varnished on a copper bobbin, suitable for sensing temperatures down to 50 mK. Following this, we dispatch the custom-built housing to Infrared Laboratories, Inc., where the bolometer installation occurs. The image of the bolometer housing is shown in Figure 2.6b. The left panel displays the highly sensitive doped Si thermistor bonded to a 3 mm diamond absorber to enhance collection efficiency. Subsequently, we mount the bolometer housing on the 0.9 K cold stage (Still plate) of the DR. The bolometer is thermally isolated from the still plate using a 0.0010-inch thick nylon sheet, preventing excessive heat transfer to the still when heating the bolometer to its desired temperature. As heat is applied to the bolometer, less than one percent change in the still plate temperature was observed, as shown in Figure 2.4a.

The bolometer, which acts as a variable resistor whose resistance depends on temperature, is connected in series with a 20 $M\Omega$ load resistor, forming a voltage divider circuit. The voltage change across the bolometer undergoes two-stage amplification in a voltage feedback composite amplifier configuration. Figure 2.5 shows the schematic of the readout electronics. A small signal voltage fluctuation at the bolometer in the form of optical load modulates the JFET gate voltage V_{G1}. JFE2140 JFET is the first gain stage in the amplification circuit, configured as a matched differential pair. JFE2140, combined with a room-temperature operational amplifier, forms the feed-forward gain stage. Adding feedback maintains a predictable closed-loop gain of 2 of the entire circuit. Resistors R_{f1} and R_{f2} shunt the output of the op-amp and provide feedback to generate a proportional voltage V_{gs2}, ensuring $V_{gs1} = V_{gs2}$. The feedback loop is located on the same PCB board as the JFET circuit inside the DR to prevent capacitive loading of the feedback network and minimize temperature-dependent Johnson noise from the feedback resistors.

As is customary in low-noise systems, the grounding configuration for the detector readout is meticulously analyzed and executed to reduce the electrical crosstalk. The dilution

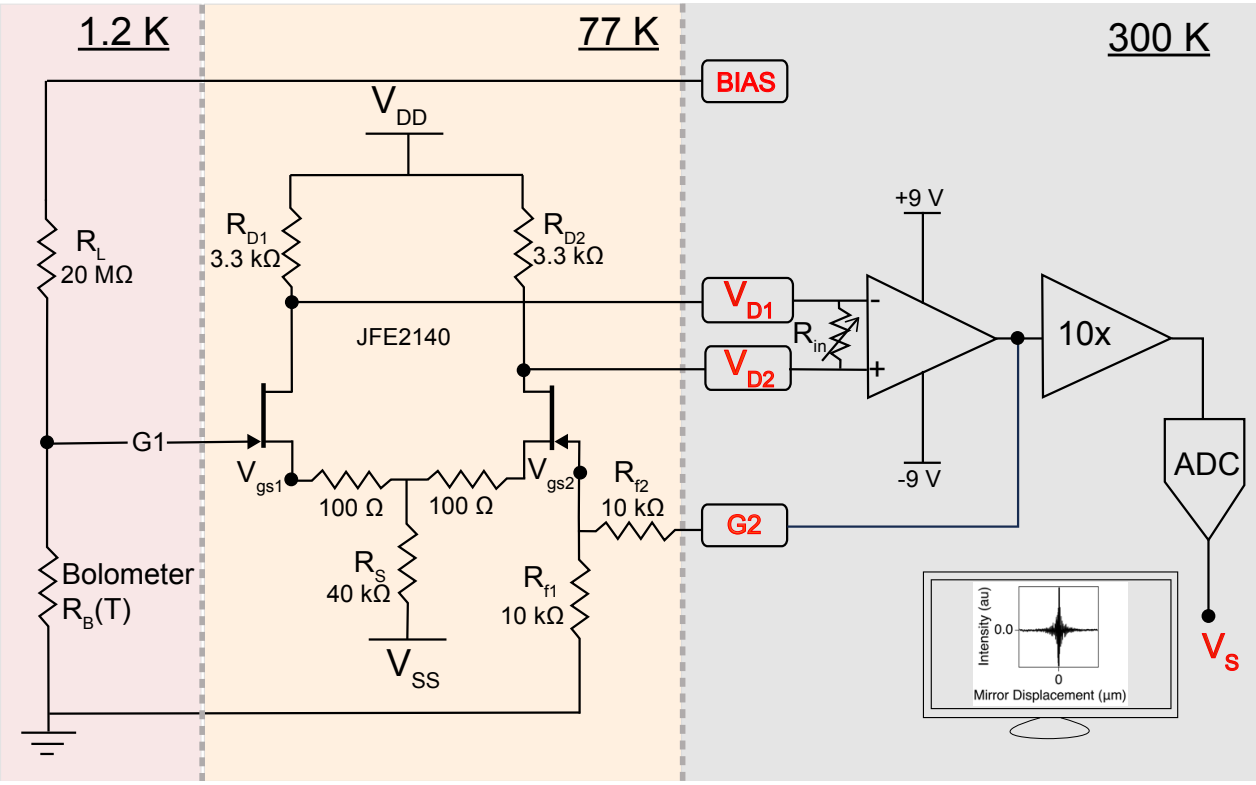

Fig. 2.5: Schematic illustrating the readout electronics across different thermal stages at 1.2 K, 77 K, and 300 K. While the operating temperature of the bolometer may fluctuate based on optical configurations, it typically remains within the range of 1.2-1.4 K. The first stage gain amplification circuit of the JFET preamp is heated to its operating temperature of 77 K, while the second stage operational amplifier and third stage preamp are situated at room temperature.

fridge serves as the low-noise ground point of a "star circuit", connected to the clean ground available in the lab. Details of DR ground configuration are illustrated in Appendix A (Figure A.1). Utilizing a composite amplifier configuration in a differential setup significantly reduces the voltage noise of the amplifier circuit. Additionally, differential measurements minimize sensitivity to microphonics, grounding issues, and other common mode noise sources. Connections to the JFET gate G_2, drain V_{D1} and V_{D2} and the bolometer bias extend to room temperature as shown in Figure 2.5 and are thermally anchored at all the cold stages of the DR.

We construct the JFET preamplifier (preamp) circuit on a double-layer 0.032" thick PCB board coated with 2 oz copper to minimize radiative heat load from the board. Figure 2.6a displays the board in a custom-built oxygen-free copper enclosure. The JFETs have a noise minimum at 77 K, and are mounted on a weak thermal link. We integrate a local thermometer and metal film resistor to the board to heat the JFET at stable operating temperature of 77 K. Securing the enclosure to the still plate and thermally anchoring it with copper wire ensures that it stays close to the base temperature of the still plate. Four 0.009" hypodermic stainless-steel tubes support the PCB board inside the enclosure, preventing excessive heat flow to the enclosure.

The temperature profiles of the still and bolometer are shown in Figure 2.7 as a function of electrical power across the JFET board. We observe approximately a 3% change in the temperature of the still plate as we apply the necessary heat to bring the preamp to its operating temperature. However, we observe that using semi-rigid co-axial cables across the bolometer housing and the enclosure inadvertently established a thermally conductive path across the two. As shown in Figure 2.7b, the base temperature of the bolometer increases from 0.9 K to 1.2 K when heat is applied to the circuit board. Nonetheless, the temperature of the bolometer remains well below its operating temperature (1.6 K).

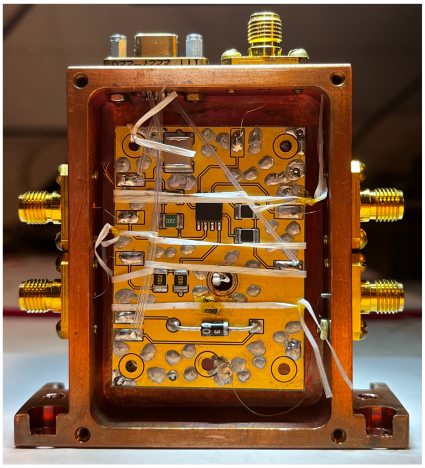

(a) JFET circuit board inside an enclosure

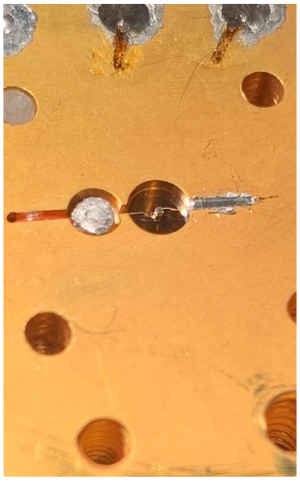

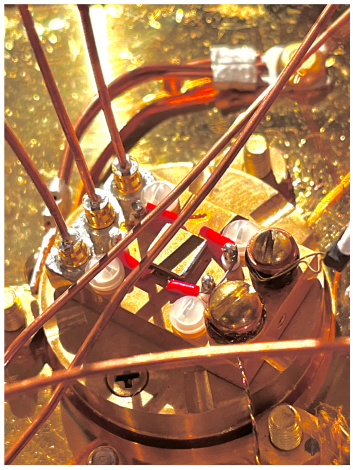

(b) (Left) Back side of the bolometer housing with composite Si bolometer bonded to a diamond absorber and suspended between two wires. (Right) The front side of the housing mounted on the still plate

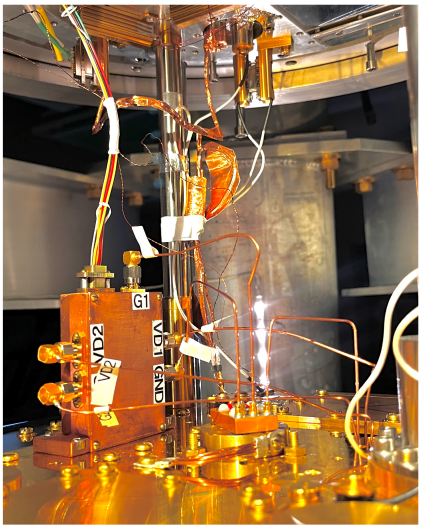

(c) Assembly of bolometer module on the still plate of the dilution fridge

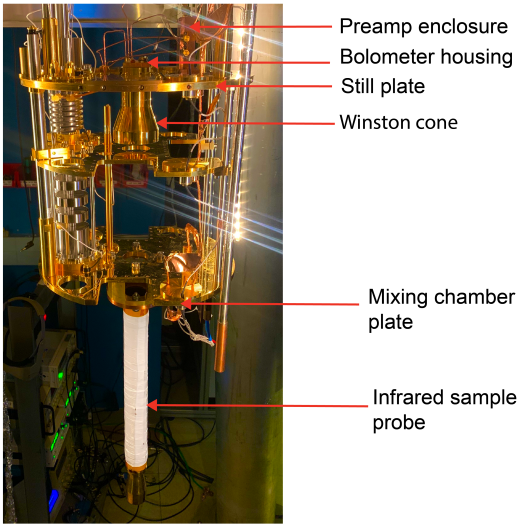

(d) Internal assembly of thr dilution fridge integrated with bolometer module and infared sample probe

Fig. 2.6: (a) Photograph of the JFET preamp circuit consisting of the Cu-coated PCB board inside an enclosure. (b) Far-IR Si bolometer housing featuring: (Left) Si bolometer bonded to a diamond absorber and suspended between two wires, and (Right) Load resistor with three plug-in SMP connectors for connections to V_bias,$G1$, and cold ground. Additionally, it accommodates a heater and thermometer mounted on copper bobbins. (c) Bolometer housing and preamp enclosure mounted on the sill plate of the dilution fridge. (d) Internal assembly of the DR integrated with infrared sample probe and bolometer module.

The second stage of amplification utilizes a room-temperature operational amplifier. The op-amp circuit is encased in a rigid aluminum enclosure to shield it from electrical pickup. Appendix A provides a detailed description of the op-amp circuit. The figure in the appendix shows the overall grounding configuration of the output signal. The output signal from the op-amp then undergoes the final stage of room temperature amplification through an analog EGG&G preamplifier with bandpass set to 3 and 300 Hz cutoff frequency. Subsequently, it is digitized by a Bruker ADC converter, transmitted to the spectrometer, and ultimately conditioned, and Fourier transformed by a computer. The schematic of the readout electronics is shown in Figure 2.5.

2.2.2 Performance characterization of 1.6 K Far-IR Bolometer

The basic function of a bolometer is to convert radiant input power to a convenient output signal. For our purpose, that output is always electrical in terms of voltage. A fundamental metric for evaluating the response of the bolometer to changes in electrical power is its electrical responsivity, which quantifies the change in voltage drop per watt of absorbed signal power. Bolometer characterization aims to determine this responsivity and other operational parameters to its optimize performance during operation. To achieve this, we conduct measurements to analyze sensitivity and noise across various levels of radiant background power. These measurements involve acquiring a series of DC I-V curves at different voltage, current biases, and stage temperatures. Subsequently, we utilize a thermal model derived from reference [62] to calculate the responsivity of the bolometer under different temperature and bias conditions.

The thermal model assumes the bolometer as a simple thermal device, shown schematically in Figure 2.8. A typical bolometer is a temperature-sensitive resistor $R_B(T)$, heated

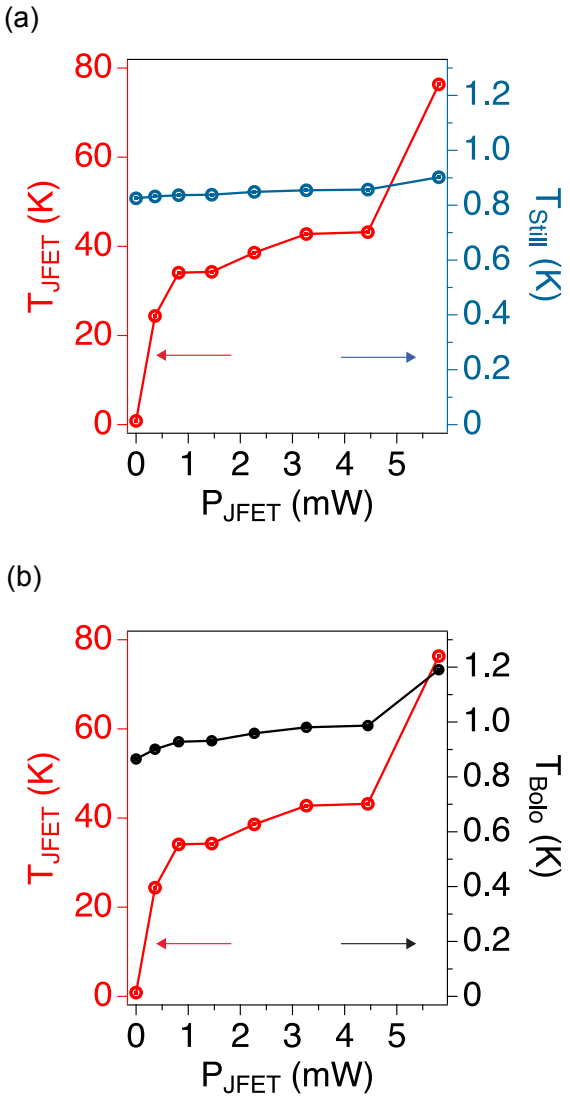

Fig. 2.7: (a) Temperature profiles of the preamp and still plate in response to the heating of the JFET circuit board. Notably, the base temperature of the still plate experiences minimal change, remaining within 5%. (b) Applying heat to the JFET board causes the bolometer temperature to rise from 0.9 K to 1.2 K. Semi-rigid co-axial cables connecting the two inadvertently establish a thermal conductive channel between the preamp enclosure and the bolometer housing.

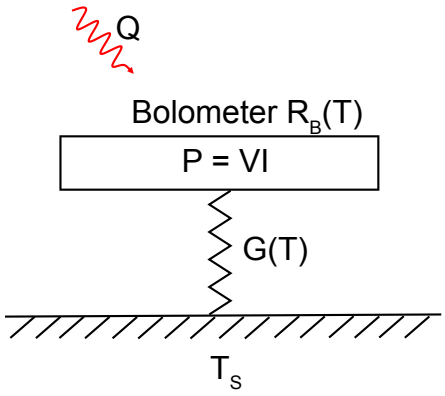

Fig. 2.8: Ideal bolometer detector model with an absorber at temperature T weakly thermally linked to a heat sink at temperature T_S, characterized by the thermal conductance $G(T)$

by incoming radiation and coupled to a heat sink at bath temperature T_S through a thermal link and static thermal conductance G_0. The bolometer absorber dissipates two sources of power: electrical power P from biasing and optical load from the radiant optical power Q. Any change in the absorbed power gives rise to a change in the bolometer resistance R_B and consequently in T_B.

Figure2.9a shows the family of DC I-V curves across a range of voltage and current biases at various stage temperatures, 1.1 K to 1.6 K, by stepping the total bias voltage and measuring the current across the bolometer. The I-V curve exhibits non-linearity due to self-heating caused by the bias voltage. By extrapolating the low-current sections of the load curve, we determine the zero bias resistance (in the absence of self-heating) for various stage temperatures. This process allows us to calculate the resistance versus temperature characteristics of the thermometer element in the bolometer. In the absence of electrical non-linearities, the thermistor resistance R_B varies with temperature T_B as

$$R_B = R^* \exp\left(\frac{T_g}{T_B}\right)^n, \tag{2.1}$$

where R^* and T_g are constants depending on the material and device geometry. In Figure 2.9b, we plot the zero bias resistance as a function of stage temperature T_S; the gradient and the offset of a linear fit give us T_g and R^*. We also look at the fit residuals to see if the value of n is applicable. If not, we can do a non-linear fit to obtain the best-fit values of n, T_g, and R^*. Our measurements correspond well to this relationship 2.1, with $n = 0.5$ as shown in Figure 2.9b.

For any given stage temperature, the model assumes that thermal conductance has a power law dependence on temperature

$$G(T) = G_0 T^{\beta}, \tag{2.2}$$

where G_0 represents the static thermal conductance at the stage temperature, and β denotes the power law coefficient for the variation of G_0 over the range of absorber temperature.

A simple model of thermal conductance is used to determine $G(T)$. The electrical biasing causes the bolometer to self-heat. It loses power to the heat sink through the thermal conductance, G; we can simply write electrical power dissipated at the bolometer thermistor as $P = G\Delta T$, where ΔT temperature difference across the thermistor element. More broadly, we can express this as

$$P = \int_{T_S}^{T_B} G\, dT = \frac{G_0}{\beta + 1} \left(T_B^{\beta+1} - T_S^{\beta+1} \right). \tag{2.3}$$

Values of β and G_0 obtained from (2.3), along with constants R^* and T_g can predict the behavior of the bolometer for temperatures at which it was not measured. For each load curve, taken at stage temperature T_S, we determine the parameters β and G_0 using power law dependence. Figure 2.9c shows the correlation of dynamic thermal conductance with

bolometer resistance.

Several key parameters are defined to determine bolometer responsivity S. The temperature coefficient of resistance (TCR) of the thermistor can be written as

$$\alpha = -\frac{1}{R}\frac{d}{dT} = -\frac{nT_g^n}{T^{n+1}}. \tag{2.4}$$

The dynamic load impedance Z, is given by

$$Z = \frac{dV}{dI} = R_B\left(\frac{G(T)+\alpha P}{G(T)-\alpha P}\right). \tag{2.5}$$

The DC responsivity, S, is then defined as

$$S = \frac{dV}{dQ} = \left(\frac{Z-R_B}{2V_B}\right)\left(\frac{R_L}{Z+R_L}\right), \tag{2.6}$$

or equivalently,

$$S = \frac{\alpha V_B}{G_{\text{eff}}(T)}\left(\frac{R_L}{R_L+R_B}\right). \tag{2.7}$$

where $G_{\text{eff}}(T)$, the effective thermal conductance. A small increase in optical loading induces a small increase in the temperature of the bolometer. Due to negative TCR, these small temperature changes create a sizable change in bolometer resistance. Consequently, the Joule heating from the bias circuit, determined by $V^2/R_B(T)$, increases the resistance of the bolometer. This process establishes a negative electro-thermal feedback. In terms of thermal conductance, this effect can be expressed as

$$G_{\text{eff}}(T) = G(T) - I^2\frac{dR}{dT}\left(\frac{Z+R_B}{Z-R_B}\right). \tag{2.8}$$

Figure 2.9d shows the difference in the dynamic and effective thermal conductance value as

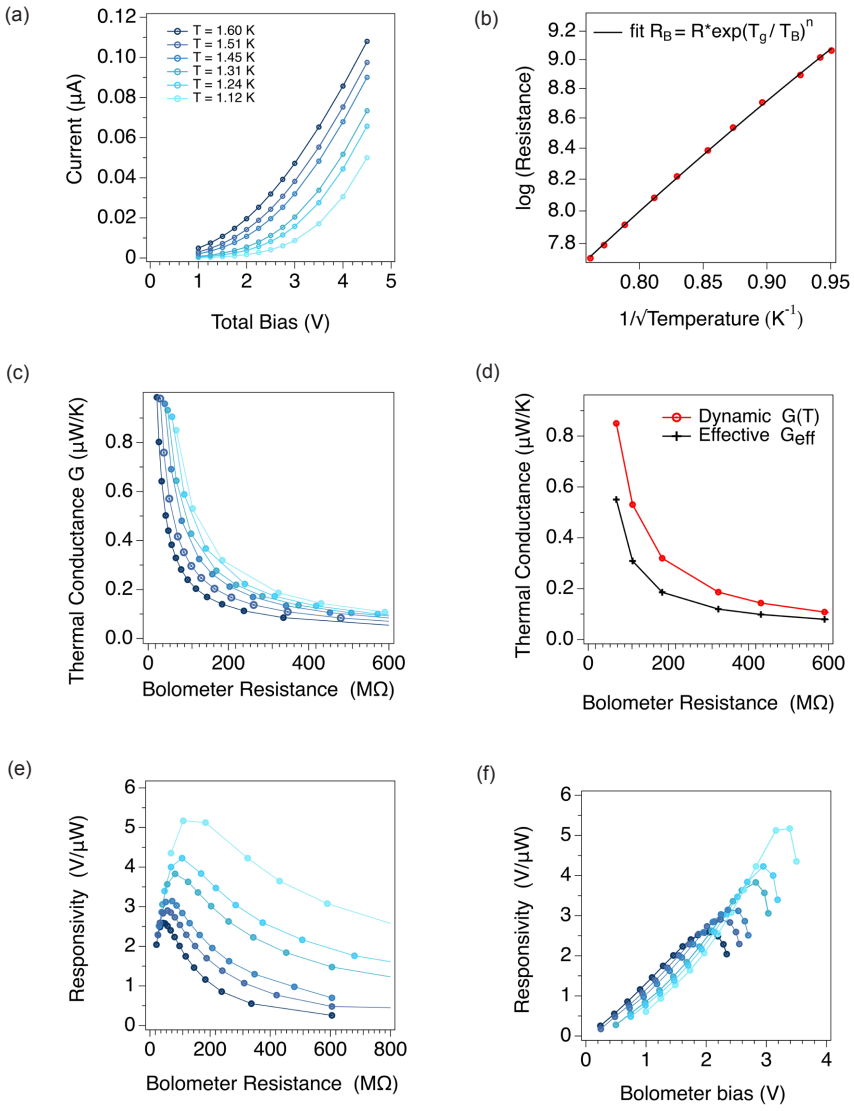

Fig. 2.9: (a) Family of DC I-V curves at different stage temperatures. (b) Dotted lines represent experimentally measured zero bias resistance versus stage temperature, while solid lines denote fits to Equation 2.1. (c) Family of conductance curves obtained from Equation 2.2 for different stage temperatures versus bolometer resistance. (d) Difference between dynamic thermal conductance $G(T)$ and effective thermal conductance G_{eff} due to negative electro-thermal feedback at $T_S = 1.6$ K. (e) Responsivity calculated from Equation 2.7 for the family of DC curves versus bolometer resistance. (f) Replotting Responsivity versus bolometer bias.

a function of bolometer resistance at $T = 1.3$ K.

The response of the bolometer depends on the steady infrared background power loading Q through a shift in the operating temperature. Since $G(T)$ increases with temperature, and TCR decreases, the responsivity decreases rapidly as the bolometer is heated, as shown in Figure 2.9e. The model used to characterize the bolometer assumes no background infrared power. However, these measurements are taken in a non-blanked configuration with 300K background radiation from that gate valve. The model is still valid to obtain electrical responsivity for any given background [63].

In Figure 2.9f, we show the bolometer responsivity calculated from Equation 2.7 as a function of bias voltage across the bolometer. Under low bias conditions, bolometer resistance is significantly higher compared to the load resistor. As bias across the bolometer increases, its resistance decreases, leading to a less negative value of α and increased responsivity. However, for higher bias, when bolometer resistance becomes comparable to the load resistor, further bias increase enhances the effective thermal conductance, causing a decrease in the responsivity. To optimize bolometer performance, we operate at a temperature and bias voltage depending on the optical load where the bolometer responsivity curve is maximized.

2.2.3 Noise analysis

Noise is defined as the rms deviation of the detector output from its average value. Once noise enters the output, it can obscure or hide small signals. Here, we systematically investigate various noise contributions encountered during the operation of the detector. Measurement of voltage noise levels presented here shows that under illumination, the bolometer is photon noise limited. This implies that the noise of the absorbed signal is higher than the total internal noise of the detector, including the amplifier noise.

The bolometer is subjected to many sources of noise, including noise in the incident radiation originating from a black body background at 300 K, Johnson noise from the resistance R_B of the bolometer, voltage and current noise contribution from the amplifier, and photon noise from the incident radiation [64]. In our noise analysis, we assume that the contribution of each term to the bolometer voltage is statistically independent; total noise contribution is obtained by adding all these noise sources in quadrature, which we can compare from an electrical evaluation of the bolometer under operation. It is convenient to summarize all major contributions to the total voltage noise density E_0 in a bolometer as the sum of 4 independent terms

$$E_0^2 = (e_N)^2_{\text{Johnson}} + (e)^2_{\text{amplifier}} + (e)^2_{\text{photon}} + (e)^2_{\text{background}}. \tag{2.9}$$

Jonhson-Nyquist Noise: A bolometer is a temperature-sensitive resistor connected in series with the load resistor; therefore, the Johnson Nyquist noise (or simply Johnson noise) of their effective resistance $R_{\text{eff}} = R_L||R_B$ in thermal equilibrium at temperature T can be easily calculated by the Nyquist theorem [65]

$$e_N = \langle V^2 \rangle / \Delta f = \sqrt{4 k_B R_{\text{eff}} T} \quad [V/\sqrt{Hz}], \tag{2.10}$$

where $\langle V^2 \rangle$ is the time-averaged mean-squared voltage and Δf is the measurement bandwidth.

Amplifier Noise: We configure JFE2140 as a differential pair in a voltage-feedback composite amplifier to provide a low-noise, high-input impedance single-ended amplifier stage for the bolometer. We select operating parameters (current and voltage) for JFE2140 to ensure that the total noise contribution from the gain stage of the amplifier in Equation

2.9 is significantly lower than any other noise source in the readout circuit, particularly the Johnson noise contribution from the bolometer resistance.

Photon noise on bolometers arises from the random fluctuations in the absorbed power because of the quasi-random arrival of the photons. The bolometer, unlike photon detectors, reacts to power rather than photon flux. The mean-square fluctuation in electrical bandwidth Δf of incident radiation in terms of absorbed power is given by

$$\frac{(\Delta P_\nu)^2}{\Delta f} = 2h^2\nu^2\Phi_\nu\eta(\nu)(1+\bar{n_\nu}), \tag{2.11}$$

where quantity $\eta(\nu)$ is interpreted as the absorptivity or equivalently as the emissivity of the detector element. Due to the highly efficient diamond absorber used in the detector module, we assume nearly unity absorptivity of detection. Quantity Φ_ν is the average rate at which photons are incident on the detector in a narrow optical bandwidth given by the following expression,

$$\Phi_\nu = \alpha\frac{\nu^2}{c^2}\bar{n_\nu}, \tag{2.12}$$

where α represents the propagation of total light power emitted by the SiC globar light source while experiencing losses in the optical path that reaches the bolometer and $\bar{n_\nu}$ is the effective photon mode occupation number given by

$$\bar{n_\nu} = \frac{1}{e^{h\nu/kT}-1}. \tag{2.13}$$

The total mean-squared power fluctuation is then given by integrating the above expression 2.11 over all the frequencies. Voltage noise density is calculated by the following expression

$$e_{\text{photon}} = \left(\sqrt{\int_{\nu 1}^{\nu 2} P_\nu \, d\nu}\right) S, \tag{2.14}$$

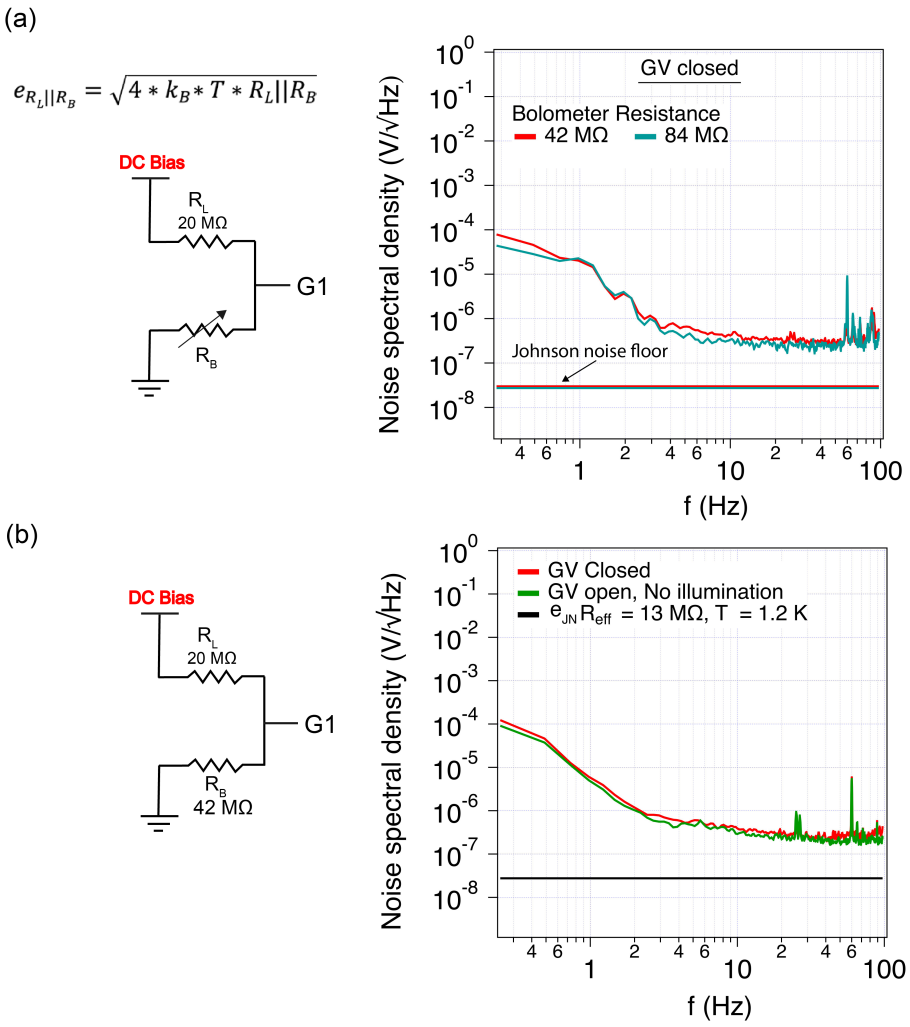

Fig. 2.10: (a) Noise spectral density with the gate valve closed is shown for two different values of the bolometer resistance. (b) Noise spectral density with the gate valve open, where light is not directed to the bolometer. The Johnson noise floor is marked for reference. Notably, the total noise in the dark configuration is five times higher than the Johnson noise floor.

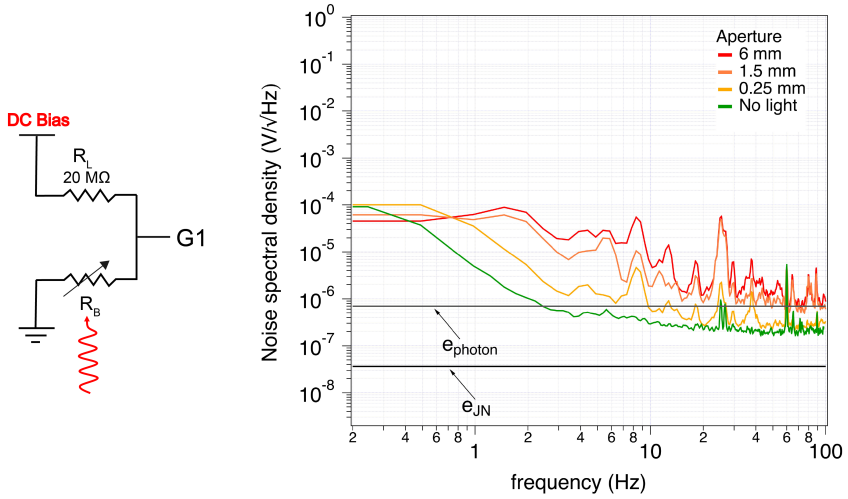

Fig. 2.11: As the optical power throughput increases with the source aperture size, the total noise spectral density also increases. The Johnson noise floor calculated from equation 2.10 and photon noise from equation 2.14 are marked for reference. For aperture $>$ 1 mm, the noise spectral density is dominated by photon noise

where S is the responsivity calculated for the detector in the previous section.

We evaluate the total voltage noise spectral density (NSD) of the bolometer under different optical configurations: initially, in the absence of infrared illumination, known as dark noise, and then under illumination. During tests under illumination, the bolometer is subjected to radiation from a source outside the DR, with an optical path opened through the radiation shields. Radiation enters the DR through a KBr window, which has a transmission of approximately 95 % over the wavelength range utilized. In the dark configuration, the radiation shields remain unblanked, hence it does not constitute a "true dark" setup.

To obtain measurements of the Noise Spectral Density (NSD) in our experiment, we begin by closing the pneumatically operated gate valve. This effectively sets the system in a dark configuration, isolating the DR from any external light sources and optics. In Figure 2.10a, we present the NSD measurements for two distinct bolometer resistances with gate valve

closed. Subsequently, we open the gate valve, establishing a connection between the external optics and the DR. The comparison of noise density measured under no illumination in both gate valve open and closed configurations is shown in Figure 2.10b. Ideally, without any optical load, the primary noise source should be the Johnson thermal noise of the bolometer. This noise component should be frequency-independent white noise. However, in practical conditions, we observe a noise floor approximately five times greater than the calculated noise from (2.10) as shown in Figure 2.10a and b. This discrepancy is likely attributed to the exposure of the bolometer to background load, given that the radiation shields of the DR are unbanked. Such exposure suggests that the fourth term in (2.9) dominates the total noise density. We further analyze the NSD for two different values of bolometer resistance, noting that the combination of $R_L||R_B$ remains relatively consistent. As a result, the change in spectral noise is negligible for bolometer resistances of 42 and 84 MΩ.

Following this baseline assessment, we measure the noise density under illumination. The broadband infrared emission from a SiC globar light source enters the DR through a KBr optical window. This optical power modulates on a timescale faster than the bolometer speed of response. We measure noise for varying source apertures below the cutoff frequency of the optical window (where no appreciable blackbody signal is expected) to avoid mixing the signal with noise.

Figure 2.11 illustrates the measurement of the noise spectral density as the diameter of the source aperture inside the spectrometer increases. When the optical power throughput increases sufficiently, the bolometer response becomes limited by photon noise. In this regime, the third term in Equation (2.9) dominates, and the contributions from detector Johnson noise or amplifier noise become indistinguishable. With an aperture size larger than 1 mm, the noise floor is primarily dominated by photon shot noise, establishing a fundamental limit on the lowest achievable noise from the detector under illumination.

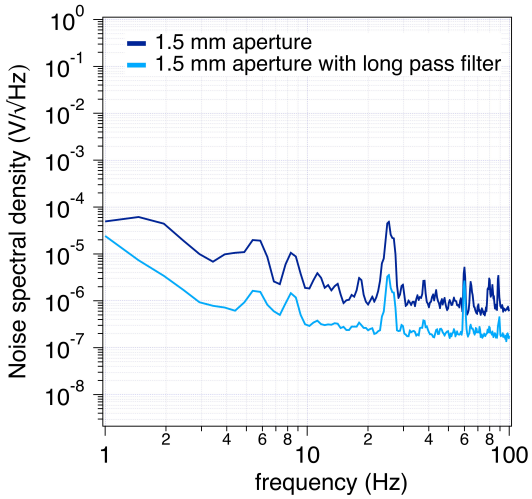

Fig. 2.12: Comparison of the noise spectral density under illumination with and without a long pass filter (LPF). The addition of the LPF results in a significant reduction in noise, showing a factor of three reduction compared to the configuration without the LPF.

Utilizing optical filters significantly mitigates photon noise, as the limit of integration in Equation 2.14 can be tailored to the frequency range of the filters. A substantial portion of the blackbody spectrum contributes to noise rather than the signal, particularly frequencies above 1500 cm^{-1} (40 THz). As illustrated in Figure 2.12, incorporating a long-pass filter with a cutoff frequency of 40 THz can reduce the noise spectral density by a factor of 3.

2.2.4 Improvements in spectroscopic measurements

Films just a few microns in size and single-atom-thick exhibit low light absorption, where the aperture or focus typically cannot be smaller than $\lambda/2$, exceeding the sample dimensions. For instance, a typical ratio of the sample area to the aluminum foil aperture is 1:10. Consequently, detecting signals in a far-field configuration with a sample positioned deep inside a magnet, several meters away from the spectrometer, yields relatively small signals, presenting a significant challenge for infrared transmission spectroscopy. Given that the cyclotron

resonance signal scales with the device area, these measurements necessitate large-area samples. However, the restricted size of exfoliated 2D materials and measurement resolution limitations result in inconveniently long spectroscopic measurements, typically averaging 8 to 10 hours for a single trace at a given field or carrier density.

Improvements in SNR can substantially reduce acquisition time, as SNR, a crucial metric for spectroscopic measurements, depends on acquisition time t as SNR $\propto \sqrt{t}$. To calculate SNR, we measure the 100 % line, a typical indicator of the noise level in the spectroscopic system. We determine the 100 % line by measuring the ratio of two transmission spectra collected under identical optical settings. We acquire the second spectrum immediately after the first. Ideally, the 100 % line should be a straight line at 100 %. Deviations from this line indicate noise and system instability as a function of energy. Figure 2.13a and b show the raw transmission and subsequently measured 100 % line calculated for two different detectors employed in this work. We then determine SNR by calculating the standard deviation σ or RMS noise from the 100 % line using the following equation

$$\text{SNR} = \frac{1}{\sigma_{\text{std.dev.}}}. \tag{2.15}$$

Conventional practice in MIR spectroscopy [56] involves measuring the noise level between 2000 cm^{-1} ($\sim$250 meV) and 2200 cm^{-1} ($\sim$ 270 meV). This region is preferred because the amplitude of the single beam spectrum is typically highest here, and there is minimal interference from water vapor and CO_2 absorption.

It is important to note that SNR or standard deviation varies across different energy ranges due to their respective magnitudes. Lower intensities correspond to smaller SNR and greater noise. Figure 2.13c compares SNR for two different detectors across various energy ranges.

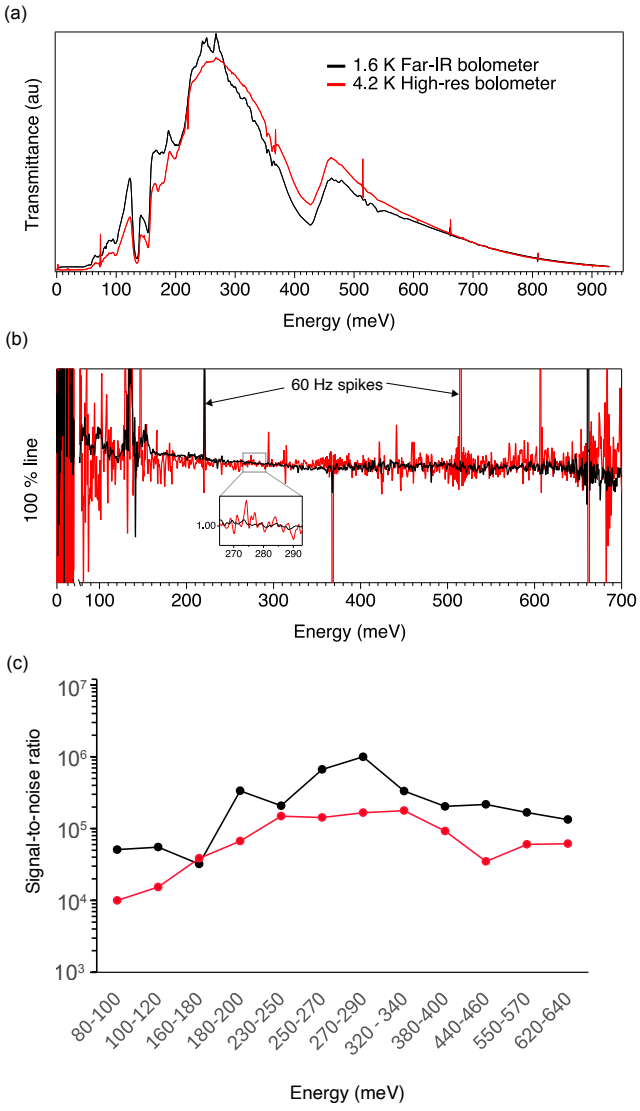

Fig. 2.13: (a) Two sets of raw transmission spectra under identical optical settings for two different detectors. (b) 100 % line obtained by rationing two back-to-back spectra from (a). (c) The signal-to-noise ratio comparison is made by calculating the standard deviation from the ratio of two spectra as a function of the energy range.

A six-fold improvement in SNR is observed with the 1.6 K Far-IR bolometer in the range conventionally utilized for MIR performance evaluation. This enhancement theoretically translates to approximately 30 times reduction in spectral acquisition time. Moreover, efforts to mitigate noise sources, particularly the persistent 60 Hz line noise, have yielded positive results. This interference, manifesting as sinusoidal oscillations in interferograms, historically obscured low signal levels, posing practical challenges. However, integrating more robust read-out electronics into the new detector module has notably diminished these 60 Hz spikes, as depicted in Figure 2.13b. CR absorption is also constrained by the area of the device. Therefore, the combination of large sample size and low-noise measurements is essential to reduce the acquisition time.

2.3 Magneto-optical measurements

We conduct transport measurements at a specific magnetic field for magneto-optical measurements to determine the carrier density for each Landau level filling factor. As an illustrative example of optical transitions, we consider the case of measurements in single-layer graphene such that the carrier density is tuned to pin the Fermi energy in the zeroth Landau level as shown in Figure 2.14b. At B = 5T, the expected resonance energy is $\Delta E_{01} \approx 90$ meV for CR transition $LL_0 \rightarrow LL_1$. We utilize a global light source, a KBr beam splitter, and a KBr optical window to facilitate these measurements.

The microscopic size of the sample results in relatively small CR signals, rendering the direct analysis of raw IR transmission impractical for studying graphene CR. Instead, its necessary to normalize the "real" CR signal to the transmission through the device without any CR signal. Typically, this normalization entails measuring the raw transmission at a specific field and normalizing it with transmission spectra obtained at zero field. However, in this

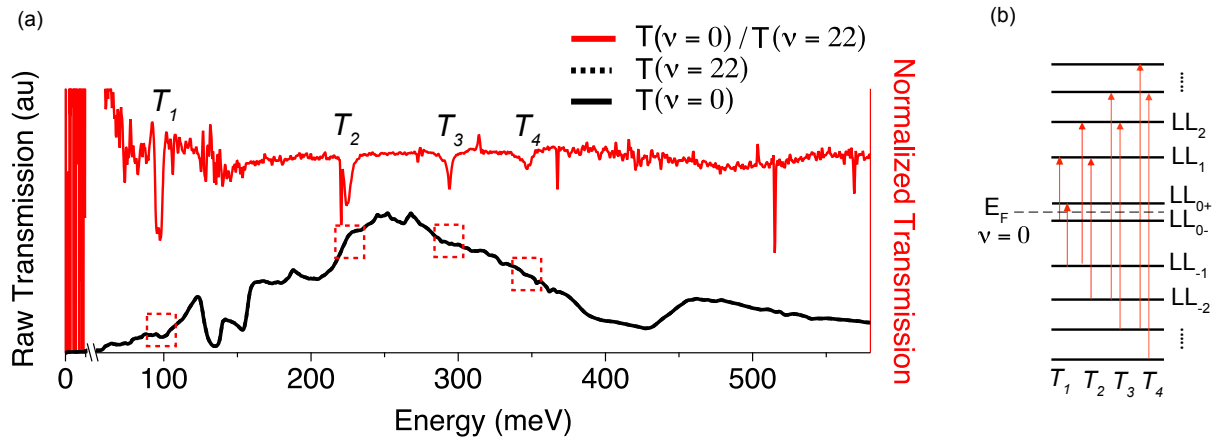

Fig. 2.14: (a) The dotted black and solid curves are raw infrared transmission collected at two gate voltages corresponding to Landau level filling factors $\nu = 0$ and 22. The red curve illustrates the normalized transmission data obtained by dividing the trace at $\nu = 0$ by that at $\nu = 22$. Four interband transitions (T_1, T_2, T_3, and T_4) appear as sharp dips in the normalized spectra. (b) A schematic illustrates Landau levels and allowed transitions consisting of nominally degenerate pairs at $\nu = 0$ when the Fermi energy is pinned to the zeroth Landau level.

scenario, other components in the optical path may exhibit magnetic field-dependent characteristics. For example, the bolometer response may exhibit significant magneto-resistance, and varying field strength can influence the interferometer mechanism. Thus, assuming only the sample changes in the field is not a valid assumption. To address this issue, at any given field, using the gate voltage to measure CR energies by adjusting the carrier density proves to be a more reliable approach.

To eliminate sample-independent features in the raw IR spectra, we employ a method that divides traces obtained at the filling factor of interest by those measured at high filling factors, where all observable interband transitions are Pauli blocked. This method electronically manipulates the allowed transition in the sample, thereby eliminating any substrate-induced absorption features during the normalization of the spectra.

To generate a normalized spectrum, we collect time-averaged raw infrared transmission

data at two different gate voltages (corresponding to different Landau level filling factors), as illustrated in Figure 2.14a. The raw infrared light curve originates from a blackbody source, with various absorptions primarily attributed to the Si/SiO_2 substrate (approximately 150 meV) and exchangeable protons (approximately 400 meV). Normalization is achieved by dividing the trace at $\nu = 0$ by that at $\nu = 22$, resulting in the normalized transmission data, shown as the red trace in Figure 2.14. Absorption in the $\nu = 0$ trace is observed as dips in the normalized spectra, while all other absorption processes occurring anywhere in the beam path, not varying with gate voltage, are normalized to unity. This process is repeated for any ν of interest.

2.4 Discussion

It is critical to control the background radiation that reaches the bolometer to obtain high sensitivity. To fully understand the true baseline noise limit of the detector in the dark, a similar analysis must be done while blanking the radiation shield of the DR and eliminating any source of background load on the bolometer. In practice, this means that the effect of absorbed power on the bolometer temperature must be negligible and bolometer performance should be limited by Johnson noise.

When discussing the temperature of the bolometer, we refer to the temperature of the bolometer housing. Due to bias and optical load, the bolometer thermistor might be at a higher temperature than the housing. In such cases, a careful assessment of the Johnson noise is essential. If the load resistor and bolometer are at different temperatures, the total Johnson noise will be calculated accordingly,

$$e_{JN} = \sqrt{4k_B \frac{R_L R_B}{(R_L + R_B)^2} (T_B R_B + T_S R_L)} \tag{2.16}$$

As part of our ongoing efforts to improve measurement capability, we are designing a cold filter mount integrated with a long-pass filter. This improvement aims to reduce the thermal load on the detector further, thereby enhancing its performance by providing additional rejection of blackbody radiation emitted from higher temperatures.

Chapter 3

Broken Symmetry States and Interaction Induced Effects in Graphene

3.1 Introduction

Graphene, since its discovery, has been the focus of extensive experimental and theoretical investigations. While significant progress has been achieved through various experimental techniques, such as angular resolved photoemission spectroscopy (ARPES) and scanning tunneling spectroscopy (STS), conventional electronic transport remains a primary method for studying the electronic properties of this remarkable material. However, optical spectroscopy offers a complementary approach, providing a powerful and versatile tool for directly verifying the electronic band structure of graphene.

Cyclotron resonance occurs when charge carriers, undergoing circular motion in a strong magnetic field, absorb light resonantly. As previously discussed, the low-energy effective theory of charge-neutral graphene describes two types of massless Dirac quasiparticles localized

at the two inequivalent corners of the Brillouin zone, known as valleys. When a perpendicular magnetic field is applied to the crystal plane of graphene, the continuum of electronic states in the graphene band structure breaks into a series of discrete Landau levels. The valley degeneracy and the physical electron spin result in four-component degenerate Landau levels.

In the absence of electron-electron interactions, the energy of the Landau levels is given by $E_n = \mathrm{s}_n\hbar\omega_c\sqrt{|n|}$, where $\omega_c = \sqrt{2}vl_B^{-1}$ represents the cyclotron frequency, $v{\sim}10^6$ m/s denotes the band velocity, $l_B = \sqrt{\hbar/eB}$ signifies the magnetic length, $\mathrm{s}_n = \mathrm{sign}(n)$, and $n = 0, \pm1, \pm2...$ represents the LL index [66, 67]. The linear and particle-hole symmetric dispersion of graphene introduces a myriad of new inter- and intra-band resonances spanning a wide range of energies. In graphene, the ease of controlling the charge carrier density (or Fermi level) allows for precise control over which transitions are active, facilitating clear assignment to specific levels of the electronic structure.

In graphene subjected to a quantizing magnetic field, the strong Coloumb interaction and fourfold spin/valley degeneracy lead to an approximate SU(4) isospin symmetry within individual Landau levels [17]. The energy scales governing cyclotron motion, $E_n = \hbar v_F\sqrt{2}/l_B$, and long-range interparticle Coulomb interactions, $E_C = e^2/\epsilon l_B$, both of which reflect physics independent of spin or valley degree of freedom, dominate over any spin or valley anisotropies [68]. The precise SU(4) symmetry for a given experimental condition in graphene hinges on the interplay between anisotropies arising from the Zeeman effect characterized by $E_Z = g_s s\mu_B B$, where μ_B is the Bohr magneton, $s = \pm1/2$ is the spin quantum number and $g_s = 2$ is the electron gyromagnetic ratio, and lattice-scale interactions and disorder, quantified by energy $E_{SR} = E_C(a/l_B)$. Despite their small magnitudes, these anisotropies are experimentally adjustable, providing an avenue for exploring symmetry-breaking phenomena.

The emergence of vdW heterostructures has significantly addressed a longstanding challenge in the field of 2D materials: the limited electronic performance observed when these materials are placed on amorphous SiO_2 substrates. Early explorations into vdW heterostructures have illuminated a remarkable enhancement in the quality of graphene devices upon the integration of an h-BN substrate [69]. This notable improvement is primarily attributed to the atomically flat nature of h-BN. Both graphene and h-BN exhibit hexagonal lattice structures. When stacked together, they adopt the lowest-energy lattice configuration, where one sublattice of carbon atoms is positioned above boron atoms while the other sublattice rests atop the center of a hexagon. This configuration of atoms breaks the sublattice symmetry in graphene, consequently leading to the formation of a band gap. Initial theoretical calculations [70] have proposed a band gap of approximately 50 meV. Consequently, beyond serving as a passive dielectric substrate, h-BN plays an active role in modifying the electronic properties of graphene.

The phenomena of symmetry breaking in graphene have been explored by a variety of experimental probes including electronic transport, quantum capacitance, and scanning probe microscopy experiments [68, 71–76]. However, the excited states of this system due to collective excitations between Landau levels (LLs) in the broken symmetry regime have been little explored to date [40, 77]. In translationally invariant systems with a parabolic dispersion, cyclotron resonance is typically insensitive to electron-electron interactions, a phenomenon known as Kohn's theorem [30, 78, 79]. However, graphene presents an ideal platform for investigating such phenomena. Unlike traditional 2D electron systems, linear dispersion of graphene allows for the direct modification of LL transition energies by many-particle interactions in CR measurements. This unique characteristic enables the spectroscopic exploration of the interplay between interaction effects and broken symmetries in graphene.

In this chapter, we investigate CR in high-quality monolayer graphene by modulating

the carrier density n via the back gate voltage V_g with a few layers of graphene. The manipulation of carrier density n in the presence of a magnetic field B allows us to control the Landau level filling factor, $\nu = nh/eB$, where h represents Planck's constant. Our observations reveal several interband transitions exhibiting non-trivial dependence on the filling factor and reveal the evolution of underlying many-particle-enhanced gaps. Analysis of the cyclotron resonance peaks shows a complete lifting of the four-fold degeneracy of Landau levels in graphene, due in part to the interaction of graphene with its encompassing boron nitride flakes but also in part to the effect of electron-electron interactions. We propose that contact between graphene and the encapsulating layers of hexagonal boron nitride (h-BN) breaks translation symmetry and serves to lift the remnants of Kohn's theorem, enabling direct contributions to the CR energy by interaction effects. This provides an unprecedented spectroscopic view of the impact of many-particle interactions in the regime of broken spin and valley symmetry in graphene.

3.2 Experiment

The sample used in this study is an 820 μm^2 sheet of monolayer graphene encapsulated between ≈40-nm-thick flakes of hexagonal boron nitride, assembled using a dry-stacking technique [80] and placed on a 4-nm-thick flake of single-crystal graphite lying on a lightly-doped, oxidized Si wafer. Electrical contacts to the edge of the graphene were made using 3/60-nm-thick films of Cr/Au, defined by standard electron beam lithography fabrication. A 90-μm aluminum foil aperture restricts the infrared light to the region surrounding the sample. Spectroscopy was performed at a base temperature of 300 mK (estimated sample temperature of < 2 K) for fixed values of the magnetic field using a broadband Fourier-transform infrared spectrometer with an instrumental resolution of 0.5 meV.

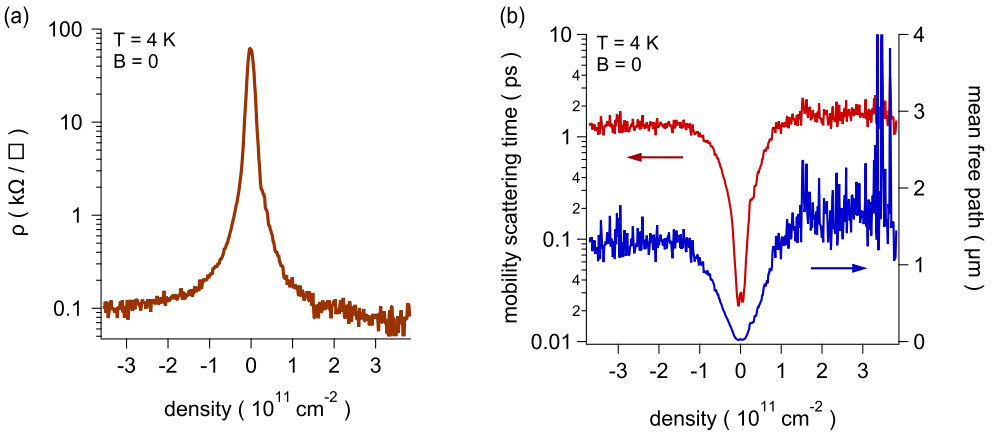

Fig. 3.1: (a) resistivity vs carrier density at 4 K. (b) the transport scattering time and mean free path derived from the resistivity data.

3.2.1 Interplay of symmetry breaking and electron-electron interaction effects

If the sublattice symmetry of graphene is broken, the valley-polarized $n = 0$ level is split by $E_{0,K}(E_{0,K'}) = +(-)M$, where M is the Dirac mass [81], and the $|n| > 0$ levels are shifted according to $E_n = \mathrm{s}_n\hbar\omega_c\sqrt{|n| + \mu^2}$, with $\mu = M/\hbar\omega_c$. The CR energies of inter- or intra-band transitions from LL m to n are then given by the level separation

$$\Delta E_{m,n} = \hbar\omega_c \left(\mathrm{s}_n\sqrt{|n| + \mu^2} - \mathrm{s}_m\sqrt{|m| + \mu^2}\right), \tag{3.1}$$

with the selection rule $|n| - |m| = \pm 1$. In graphene, these energies can also include contributions from many-particle interactions, in contrast to materials with a parabolic dispersion where the center-of-mass and inter-particle coordinates are separable and CR becomes insensitive to electron interactions, a result known as Kohn's theorem [30–32]. The linear dispersion of graphene mixes these coordinates so that interactions can directly impact LL

transitions [27, 33–37], leading to deviations from Eq. 3.1 [28, 38–41] and dependence of CR on the LL filling factor, $\nu = 2\pi n_s l_B^2$, where n_s is the charge carrier sheet density [42].

3.2.2 Evolution of cyclotron resonance transition in the broken symmetry regime

In graphene, several interband CR transitions T_i can be observed simultaneously at fixed filling factor, comprising nominally degenerate pairs of inter-LL excitations $n = -i \rightarrow i-1$ and $1-i \rightarrow i$ with energies given by Eq. 3.1. Figure 3.2(a) shows a color map of transitions T_1 through T_5 acquired as a function of ν, in which the square-root dependence of the energies on the LL indices is immediately apparent. A schematic of the allowed transitions at half-filling is drawn in Fig. 3.2(b), and a representative linecut at $\nu = 0$ is shown in Fig. 3.2(c). The very narrow resonances follow from recent improvements in sample fabrication [69, 82] and are key to enabling our observations. In Fig. 3.2(d) we show T_1 at $\nu = 0$ in devices from the present and two prior works [38, 42], revealing a clear decrease in the half-width at half-max, Γ. The lower two traces in Fig. 3.2(d) provide a comparison of two common gating methods: the middle trace is acquired in a sample with a distant, doped Si/SiO_2 substrate on which the encapsulated monolayer rests [42], while the lower trace from the present work uses a local graphite gate. By chance, these two devices have similar charge carrier mobilities of 200,000 cm^2/Vs, but the graphite-gated device shows greater values of the quantum scattering time τ_q extracted from Shubnikov-de Haas oscillations [83]. This likely reflects improved screening of charged impurities in the SiO_2 by the graphite. The CR lifetimes $\tau_{CR} = \hbar/\Gamma$ in Fig. 3.2(e) are similarly improved, and in fact, the value of ~600 fs quoted for the present device is a lower limit as even narrower lines with $\tau_{CR} \approx 2.5$ ps ($\Gamma = 0.26$ meV) are seen at higher instrumental resolution. This latter value is close to the

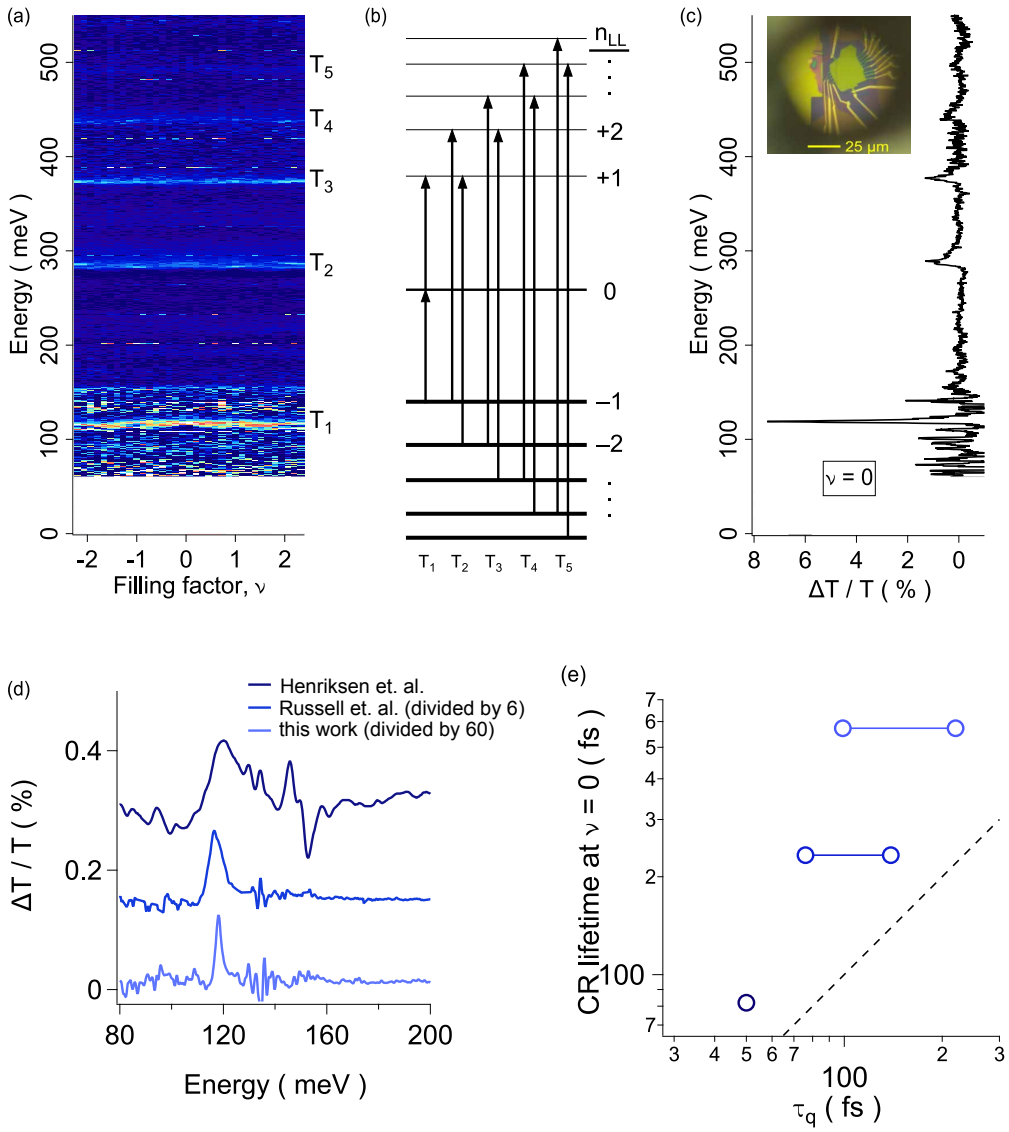

Fig. 3.2: (a) Color map of the normalized transmission spectra $\Delta T/T$ in the mid-infrared as a function of the LL filling factor, ν, measured in the device shown inset to (c). (b) Schematic showing the allowed Landau level transitions at $\nu = 0$. (c) Representative linecut of the color map at $\nu = 0$. (d) Evolution of CR lineshape at $\nu = 0$ with sample quality: the top trace is from a graphene-on-SiO_2 device [38], the middle is from an h-BN-encapsulated device on SiO_2 [42], and the bottom is the present graphite-gated, h-BN-encapsulated device. (e) CR lifetime $\tau_{CR} = \hbar/\Gamma$ at $\nu = 0$ (Γ the half-width at half-max) vs a spread of quantum scattering times τ_q acquired for a range of carrier densities at 3 K (colors correspond to traces (d). The dashed line marks $\tau_{CR} = \tau_q$.

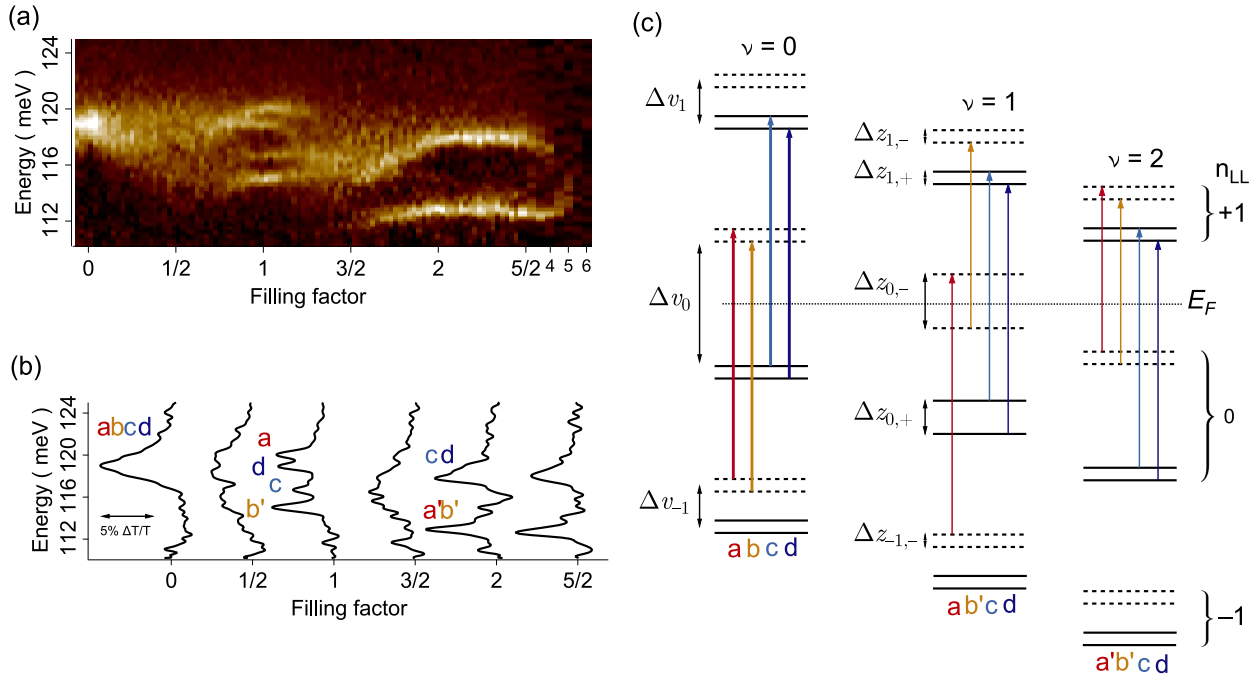

Fig. 3.3: Evolution of transition T_1 vs filling factor. (a) High-resolution map of T_1 vs filling factor from $\nu = -0.07$ to $\nu = +2.5$. (b) Detail of transitions by line cuts at half-integer fillings. (c) Schematic of transitions involving the $n = -1, 0$, and $+1$ LLs. Solid (dashed) lines indicate the K (K') valleys, with valley gaps Δv_i and spin splittings Δz_i explicitly included. The Fermi energy E_F is shown as a dotted line.

transport time derived from the mobility 3.1b, suggesting that impurity collisions limit the CR lifetime. Consistent with prior observations of CR in AlGaN/GaN heterostructures [84], τ_{CR} can be several times larger than τ_q which is reduced by variations in the carrier density across the sample.

In Figure 3.3 we focus on the T_1 transition over filling factors $\nu = 0$ to $+6$, where a marked non-monotonic evolution is seen from a single resonance at $\nu = 0$ to four resonances around $\nu = +1$, which reduce back to two for $\nu \gtrsim +2$ that both fade away as $\nu \to 6$ and the $n = +1$ LL is completely filled. Linecuts in Fig. 3.3(b) show details at half-integer ν. The resonances manifest in intriguing patterns: the higher energy peaks at $\nu = 1$ appear

and disappear at different ν values, while the lower energy pair appears simultaneously and then merges with increasing ν. At $\nu = 2$ the upper peak first appears at a lower energy near $\nu = 3/2$ and then rapidly rises before leveling off for $\nu \gtrsim 2$. Note these features at $\nu = 1$ and 2 persist over a wide range of ν. This is a real effect and not due, for instance, to small variations in the carrier density across the sample: from the width of the Dirac peak in the zero-field resistance vs density shown in 3.1a, we estimate a distribution of carrier densities $\delta n_s \approx 2 \times 10^{10}$ cm^{-2}, or $\delta\nu \approx 0.1$ at 8 T, rather smaller than the range over which the $\nu = 1$ and 2 features persist. At $\nu = 1/2$ and $3/2$, broad resonances appear that nevertheless maintain the full spectral weight, suggesting all transitions are present but unresolved. This could indicate the presence of dark magnetoexciton modes serving as additional scattering channels: there are up to 16 distinct transitions between the 0 and ±1 LLs although only the four that conserve spin and valley are optically active [27].

The CR energy is given by the energy *difference* of participating levels, with the restriction that the spin and valley orientations are preserved. Without interactions or symmetry-breaking mechanisms, the energies of the four component transitions of T_1 are degenerate and equal to the LL separation. Any gap, e.g., due to Zeeman splitting that is the same in both LLs, is invisible to CR. Thus, the multi-peak structure in Fig. 3.3, particularly at $\nu = 1$, requires that both spin and valley symmetries are broken to a differing extent in the $n = 0$ and ±1 LLs. In the present device architecture, an obvious valley-symmetry-breaking mechanism results from contact of graphene with the encompassing h-BN [48, 74], generating a mass M that splits the $n = 0$ level and shifts the higher levels. Additionally, the spin splittings of the $n = 0$ and $n = \pm1$ levels must also differ in energy, which is most readily achieved by invoking Coulomb interactions. But as noted above, the remnant of Kohn's theorem in graphene allows only for a filling-independent renormalization of the velocity, $v \to \tilde{v}$, for T_1. Thus, Eq. 3.1 should apply, and even with finite μ, the T_1 energy

at $\nu = 0$ should be precisely the same as the higher energy peak when T_1 splits at $\nu = 2$ [85]. Yet in Fig. 3.3 it is higher, by 1.3 meV. Thus, even this surviving part of Kohn's theorem must be broken. This cannot be due to non-parabolicity. Disorder is a potential culprit, although it is quite weak as seen by how narrow the CR linewidths are compared to the observed shifts and splittings. On the other hand, the interaction of graphene with the h-BN substrate gives rise to a long wavelength moiré pattern that breaks the translation symmetry of the graphene lattice [48, 86]. Thus, we propose that the h-BN be responsible for lifting the final restrictions of Kohn's theorem, enabling all interaction effects to contribute to the CR energies on an equal footing. This is a fortunate outcome, as interactions are relatively strongest for the T_1 transition.

In Figure 3.3(c), we introduce schematics representing the simplest model of transitions between the $n = 0$ and ± 1 LLs that align with the observed CR. These are drawn for $\nu = 0, +1$, and $+2$, with each of the four spin- and valley levels shown explicitly albeit with greatly exaggerated level shifts and gap sizes. In graphene, the inapplicability of Kohn's theorem implies the CR transition energies will reflect the single-particle LL separations plus many-particle shifts of the levels, along with excitonic and exchange corrections due to the excited electron and remnant hole [27, 33, 34, 85, 87]. Of course the measured energies do not indicate which portion is due to level shifts vs exciton corrections. Therefore, we model each transition energy as a sum of the LL separation plus the difference of any valley and Zeeman gaps in each level, with the understanding that these gaps are meant to represent both single- and many-particle energies.

For instance, at $\nu = +2$ two resonances are observed although up to four transitions (two each for valley and spin, labeled a', b', c, and d in Fig. 3.3(c)) are allowed. All LLs are either completely filled or empty so that interactions are expected to be minimized. If we assume that the Zeeman splittings in the $n = 0$ and 1 LLs are equal, then the observed

CR splitting $\Delta E^{\nu=2} = E^{c,d} - E^{a',b'}$ arises from transitions originating on either side of the valley gap in $n = 0$. Note if the $n = 1$ LL also has a non-zero valley gap, it is still the *difference* of these gaps, $\Delta v^{\nu=2} \equiv \Delta v_0 - \Delta v_1 = \Delta E^{\nu=2}$ that is detected. If the Zeeman splitting were also enhanced in one level over another, this picture would predict additional resonances not present in the data. Fitting the two peaks at $\nu = 2$ with Lorentzians, we find $\Delta E^{\nu=2} = 5.0(1)$ meV. Since any valley splitting of the $n = 1$ LL is likely to be small, this should be a good measure of the valley gap in the ZLL. We identify this gap as due to sublattice symmetry-breaking from the presence of h-BN [74], and calculate a Dirac mass $M = 2.5$ meV.

At $\nu = 0$, the single peak indicates the four allowed transitions are all degenerate. By the schematic in Fig. 3.3(c), the CR energy is given by the LL separation plus half the difference of the valley gaps in the zeroth and ± 1 LLs. That a single resonance is seen implies the valley gaps in the $n = \pm 1$ levels must be equal, and all of the Zeeman gaps must also be the same, or else additional CR lines would be seen. Actually, the $\nu = 0$ resonance is the broadest in T_1, suggesting there may be unresolved lines due either to a differential enhancement of these gaps or a level repulsion between the two degenerate pairs labeled $\{a,b\}$ and $\{c,d\}$ in the figure if lattice-scale interactions couple the K and K' valleys. Indeed, such a splitting appears at 13 T as discussed below. For now we determine the valley gap difference to be $\Delta v^{\nu=0} = 2\ (E^{\nu=0} - E^{\nu=2}_{avg}) = 7.3(5)$ meV, where $E^{\nu=2}_{avg}$ is the average energy of the two peaks at $\nu = 2$. This yields a Dirac mass of 3.7 meV, substantially enhanced over its value at $\nu = 2$.

Finally, four resonances are seen at $\nu = 1$, which requires each transition to comprise a unique combination of valley and spin gaps in the initial and final LLs. In Fig. 3.3(c) we sketch a scenario where, for instance, the two transitions $\{c, d\}$ (that are degenerate at $\nu = 0$ and $+2$), now gain distinct energies at $\nu = 1$ when the Zeeman gaps in the $n = 0$

and 1 LLs become unequal. Moreover, the two Zeeman gaps in the $n = 0$ level marked $\Delta z_{0,-}$ and $\Delta z_{0,+}$ must be differentially enhanced, or else the transitions marked a and d will remain degenerate. The difference of the valley gap energies in the $n = 0$ and ± 1 LLs, namely $\Delta v^{\nu=1} = \Delta v_0 - \Delta v_{\pm 1}$, and the two Zeeman differences $\Delta z_- = \Delta z_{0,-} - \Delta z_{\pm 1,-}$ and $\Delta z_+ = \Delta z_{0,+} - \Delta z_{1,+}$, can be extracted by inverting a matrix that records the contribution of each gap to the transition energy. The full procedure is described in the next section. Note we assume that gaps in the $n = \pm 1$ levels are identical. While the size of this valley gap is close to that found at $\nu = +2$, the spin gaps are significantly larger than the bare Zeeman energy at this field, $E_Z = 0.93$ meV, indicating a clear role for electron interactions. The enhanced Δz_+ splitting is notable, as both levels are occupied and well below the Fermi energy. This is reminiscent of indirect exchange splitting in the spin sector seen in GaAs quantum wells [88], except that here, the splittings occur in different valleys, indicating the presence of lattice-scale interactions coupling valleys K and K'. Meanwhile, the size of Δz_- at the Fermi energy compares well to a transport gap of ~ 5 meV, for $\nu = -1$ at 9 T, found in Ref. [68]. Casting these as effective g-factors, we find the spin gap at the Fermi level has $g^*_{z;-} = \Delta z_-/\mu_B B = 9.3$, and the buried spin gap (in the K valley) has $g^*_{z;+} = 4.5$.

3.2.3 Model for gap energies and their evolution in field

In Fig. 3.4, an expanded version of the transition schematic in Fig. 3.3c is shown. At left, three lines mark the energy of the non-interacting $n = 0$ and ± 1 Landau levels (taken to be particle-hole symmetric). On the right, the same LLs are shown with valley and Zeeman gaps (greatly exaggerated). Solid (dashed) lines indicate the K (K') valleys. Each valley and spin splitting is labeled and can, in principle, be different. The four allowed transitions that conserve spin and valley are shown, labeled a, b', c, and d. We assume each transition

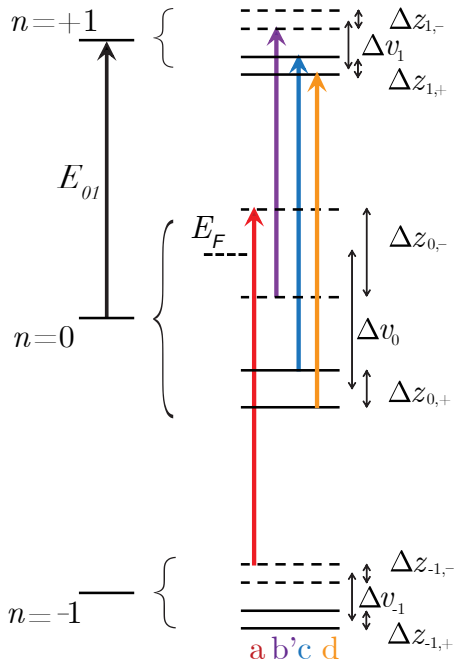

Fig. 3.4: Schematic showing single-particle LL energies (left) and the interaction-enhanced valley and Zeeman gaps (right), for filling factor $\nu = +1$. Four spin- and valley-conserving transitions are labeled a, b', c, and d for consistency with the main text. Each possible spin and valley gap is individually marked.

energy can be given by the LL separation E_{01} plus or minus half of the relevant valley and spin gaps:

$$\begin{aligned} E_a &= E_{01} + 1/2\,(\Delta v_0 - \Delta v_{-1} + \Delta z_{0,-} - \Delta z_{-1,-}) \\ E_b' &= E_{01} + 1/2\,(-\Delta v_0 + \Delta v_1 + \Delta z_{0,-} - \Delta z_{1,-}) \\ E_c &= E_{01} + 1/2\,(\Delta v_0 - \Delta v_1 - \Delta z_{0,+} + \Delta z_{1,+}) \\ E_d &= E_{01} + 1/2\,(\Delta v_0 - \Delta v_1 + \Delta z_{0,+} - \Delta z_{1,+}) \end{aligned} \tag{3.2}$$

where $+(-)$ is shorthand for the $K(K')$ valleys. Although the schematic contains 10 unknown parameters, only 9 are employed since there are no transitions from valley K in level $n = -1$, and $\Delta z_{-1,+}$ can be ignored. Meanwhile, four CR peaks are observed at $\nu = +1$, with the peak energies E_i. Inspection of Eqs. 3.2 shows that all the parameters come in pairs

that give the *difference* of gaps of the same kind in different LLs, so with new notation $\Delta v_{0,1} = (\Delta v_0 - \Delta v_1)$, &c., we can write

$$\begin{aligned} E_a &= E_{-1,0} + 1/2\,(\Delta v_0 - \Delta v_{-1} + \Delta z_{0,-} - \Delta z_{-1,-}) \\ E'_b &= E_{01} + 1/2\,(-\Delta v_{0,1} + \Delta z_{0,1;-}) \\ E_c &= E_{01} + 1/2\,(\Delta v_{0,1} - \Delta z_{0,1;+}) \\ E_d &= E_{01} + 1/2\,(\Delta v_{0,1} + \Delta z_{0,1;+}) \end{aligned} \tag{3.3}$$

There are now 6 unknowns and four measured energies. To go further, we must make some assumptions about the differences between the various gaps. It is not obvious how to proceed since, for instance, the valley gaps in $n = +1$ and -1 are not necessarily the same once interactions are included due to the asymmetric location of the Fermi energy. However, the Zeeman energies are generally small, and it is reasonable to assume that they remain so in the $n = \pm 1$ levels. Thus let Δz_+ (Δz_-) describe the difference between spin gaps of the $n = 0$ and $n = \pm 1$ LLs in the K (K') valley. Finally, since E_{01} is the same for all four transitions, we define $\Delta E_i = E_i - E_{01}$ (here we will take E_{01} to be the average of the split resonance at $\nu = 1$, but in fact, we will soon) and rearrange to find:

$$\begin{pmatrix} \Delta E_a \\ \Delta E'_b \\ \Delta E_c \\ \Delta E_d \end{pmatrix} = \frac{1}{2} \begin{pmatrix} 0 & 1 & 0 & 1 \\ -1 & 0 & 0 & 1 \\ 1 & 0 & -1 & 0 \\ 1 & 0 & 1 & 0 \end{pmatrix} \begin{pmatrix} \Delta v_{0,1} \\ \Delta v_{0,-1} \\ \Delta z_+ \\ \Delta z_- \end{pmatrix}$$

which can be inverted to yield values for the gap differences in terms of the measured transition energies E_i, so long as we can identify which resonance energy belongs to which transition in the schematic. To do so, we assume the enhanced gaps follow the size hierarchy sketched

in Fig. 3.4 (consistent with expectations from transport measurements [68]). Then the four peak energies E_i are extracted by fitting with Lorentzian lineshapes to the $\nu = +1$ data, which yields $\Delta E_a = 2.8$ meV, $\Delta E_b = -2.2$ meV, $\Delta E_c = -0.4$ meV, and $\Delta E_d = 1.7$ meV. Inverting the matrix above gives

$$\begin{aligned}
\Delta v_{0,1} &= \Delta E_c + \Delta E_d &&= 1.3 \text{ meV} \\
\Delta v_{0,-1} &= 2(\Delta E_a - \Delta E_b') - (\Delta E_c + \Delta E_d) &&= 8.7 \text{ meV} \\
\Delta z_+ &= -\Delta E_c + \Delta E_d &&= 2.1 \text{ meV} \\
\Delta z_- &= 2\Delta E_b' + \Delta E_c + \Delta E_d &&= -3.1 \text{ meV}
\end{aligned}$$

While this procedure works in principle, the negative value is problematic. In fact, these results are sensitive to the value of E_{01} because while $E_{-1,0} = E_{0,1}$ in principle, in fact, we clearly observe a small but finite particle-hole asymmetry. This suggests we should eliminate E_{01} by using the *differences* between the observed peak energies instead. This reduces the number of measurements to three, so the number of parameters also must be reduced. Assuming the valley gaps of the $n = \pm 1$ levels are small leads to $\Delta v_{0,1} = \Delta v_{0,-1} \equiv \Delta v$. Then the difference of each peak energy is $\Delta E_{ij} = \Delta E_i - \Delta E_j$, and

$$\begin{aligned}
\Delta E_{ab'} &= \Delta v \\
\Delta E_{b'c} &= -\Delta v + {}^1\!/_2\,(\Delta z_- + \Delta z_+) \\
\Delta E_{cd} &= -\Delta z_+
\end{aligned} \tag{3.4}$$

The matrix is now

$$\begin{pmatrix} \Delta E_{ab'} \\ \Delta E_{b'c} \\ \Delta E_{cd} \end{pmatrix} = \begin{pmatrix} 1 & 0 & 0 \\ -1 & 1/2 & 1/2 \\ 0 & -1 & 0 \end{pmatrix} \begin{pmatrix} \Delta v \\ \Delta z_+ \\ \Delta z_- \end{pmatrix}$$

The (measured) peak energy differences are $\Delta E_{ab'} = 5.0$ meV, $\Delta E_{b'c} = -1.8$ meV, and $\Delta E_{cd} = -2.1$ meV; and inverting the matrix we find

$$\begin{aligned} \Delta v &= \Delta E_{ab'} && = 5.0 \text{ meV} \\ \Delta z_+ &= -\Delta E_{cd} && = 2.1 \text{ meV} \\ \Delta z_- &= 2\Delta E_{ab'} + 2\Delta E_{b'c} + \Delta E_{cd} && = 4.3 \text{ meV} \end{aligned}$$

We briefly note that although Kohn's theorem does not hold in graphene in general, a limited version is predicted to survive for the T_1 transition [27, 33, 34]. However, the filling-factor-dependent shifts and splittings found here strongly imply that even this remnant does not hold. We speculate that either the h-BN-induced moiré pattern (with a length scale comparable to the magnetic length) or the lattice-scale interactions invoked to explain the $\nu = 0$ ground state [75] are sufficient to break translation invariance and render Kohn's theorem inoperable.

To better understand the nature of these splittings, we show the magnetic field dependence of the extracted spin and valley gaps at $\nu = 1$ in Fig. 3.5(a). The measured spin gap energies are substantially larger than the Zeeman energy, which suggests an interaction enhancement consistent with the ferromagnetic ground state at quarter filling in Ref. [68]. The gaps exhibit a sub-linear increase with the magnetic field, close to the $\sqrt{B}$ dependence expected for interaction effects, although further work is needed to understand the precise field dependence. Unlike the spin gaps, the $\nu = 1$ valley gap is observed to decrease with

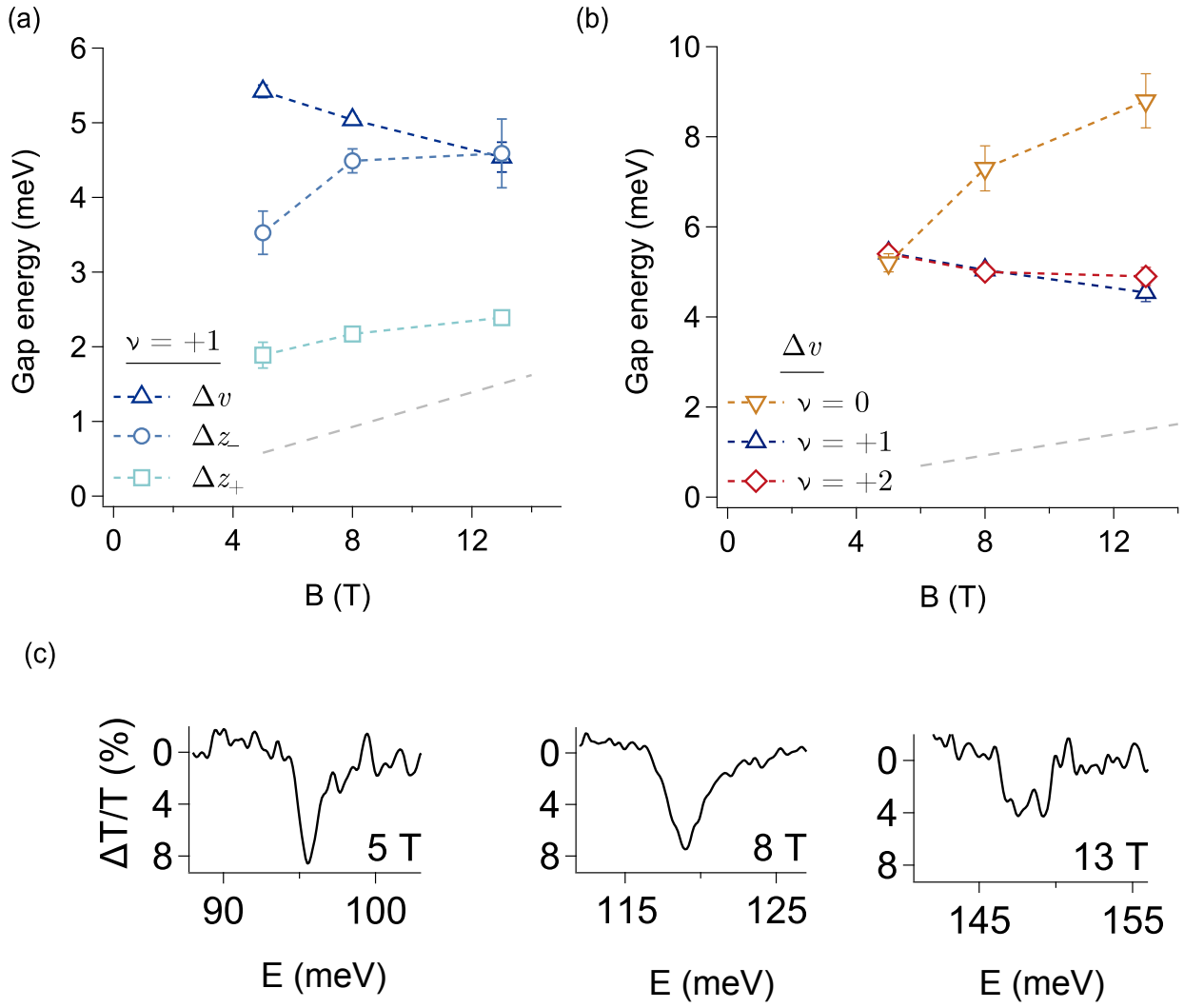

Fig. 3.5: The magnetic field dependence of the observed gaps at $\nu = 1$. The valley gap Δv appears to decrease with increasing field while the spin gaps Δz_- and Δz_+ increase with increasing field. (b) Comparison of the valley gaps calculated at integer filling as a function of the magnetic field. (c) The T_1 resonance at $\nu = 0$ for three magnetic fields. The T_1 resonance at $\nu = 0$ for three magnetic fields. With increasing field, the resonance broadens and shows an incipient splitting.

increasing magnetic field. In Fig. 3.5(b) this valley gap is compared with those for the half- and fully-filled $n = 0$ LL, where we find the gaps at $\nu = 1$ and 2 remain closely matched as the field changes. Since interaction effects should be weakest at $\nu = 2$, this agreement suggests the valley gap at $\nu = 1$ is hardly impacted by interactions. In contrast, the valley gap extracted for $\nu = 0$ increases dramatically with increasing magnetic field, consistent with the understanding that the ground state at $\nu = 0$ involves an interaction-driven breaking of valley symmetry, which drives an enhancement of the gap [68, 75, 89]. A closer look at $T_1(\nu = 0)$ for multiple fields in Fig. 3.5(c) shows the resonance broadens at 8 T compared to 5 T and develops a clear splitting by 13 T (note $\Delta v^{\nu=0}$ in Fig. 3.5(b) uses the average value of this splitting). As noted previously, this is perhaps due to the level repulsion of degenerate transitions in the two valleys by short-ranged Coulomb interactions, known to be important in the study of quantum Hall ferromagnetism but not yet studied in the context of CR in graphene [89].

3.2.4 Higher interband channels

Finally, in Figure 3.6 we explore the evolution of the second interband transition, T_2. Inspection of the color map and line cuts shows that splitting is just resolved at $\nu = 0$, with peaks of approximately equal strength. This evolves into a bright and sharp peak at $\nu = +1$ accompanied by a much weaker resonance on the high energy side, while at $\nu = +2$ the splitting persists but most of the spectral weight has shifted to the higher energy peak. Similar to T_1, at half-integer fillings, only a single broad resonance is seen, although the integrated intensity remains constant over this range of ν [**Note1**]. The peaks are split by 2.8 meV at $\nu = 0$ and 4.7 meV at $\nu = +2$. The behavior with changing magnetic field shown in Fig. 3.6 (d) is rather different than for T_1. For T_2, a single $\nu = 0$ peak at 5 T gains a splitting

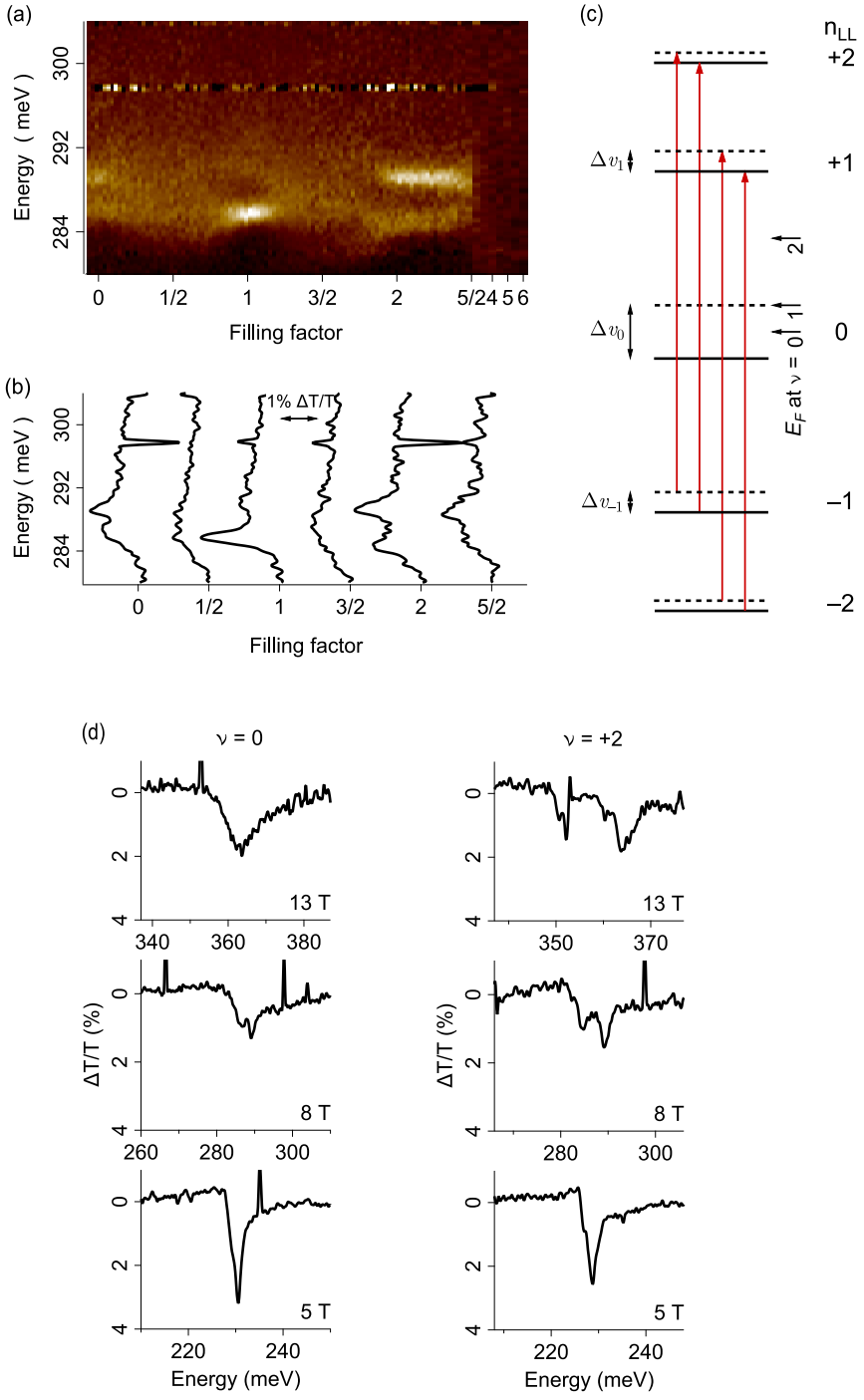

Fig. 3.6: (a) High-resolution map of T_2 for the same filling factor range as Fig. 3.2. (b) Line cuts at half-integer filling factors. (c) Schematic of T_2 transitions, with the K (K') valley shown as a solid (dashed) line. (d) Spectra at $\nu = 0$ and $+2$ as a function of magnetic field. A remarkably large splitting, nearly 13 meV in size, appears at $\nu = +2$ at 13 T.

at 8 T but reverts to a broader single resonance at 13 T. Since the T_2 transition comprises two nominally degenerate pairs of transitions $n = -2 \rightarrow +1$ and $-1 \rightarrow +2$ in each valley, as above a weak valley coupling may split the degeneracy. Whether the splitting is observed may depend on the width of the resonances, which increases with the field. For instance, at 8 T, the splitting is greater than the width and can be seen but is likely masked by further broadening of the resonance by 13 T. In contrast, at $\nu = 2$, the sharp single peak at 5 T evolves by 13 T into an unexpectedly large splitting, nearly 13 meV, far larger than any other splitting seen in this work. In the many-particle theories of Ref. [33, 85], interactions alone suffice to break the degeneracy of the $n = -2 \rightarrow +1$ and $-1 \rightarrow +2$ transitions at both $\nu = 0$ and 2; further small corrections are expected for a finite Dirac mass. For T_2, Ref. [85] predicts an approximately 3 meV splitting for a 5 meV gap. This roughly matches the scale of splittings at 8 T but greatly underestimates the $\nu = 2$ splitting at 13 T. This large splitting is a surprise since for $\nu = 2$, all orbital levels are filled or empty, and interaction corrections should be minimal. At this time no mechanism is clearly responsible for such a large splitting at $\nu = 2$. The next higher interband transition, T_3, also shows an intriguing and larger-than-expected sequence of splittings. A map of the transition energies vs filling factor along with line cuts at integer filling factor is shown in 3.7. The signal-to-noise in even higher interband transitions is not sufficient to resolve splittings.

Figure 3.7(a) shows a colormap of transition T_3, with the same filling factor resolution of $\delta\nu = 0.026$ as used in 3.2 and 3.3. T_3 shows a significant brightening around $\nu = 2$ due to a narrowing of the resonance since the integrated intensity does not change until $\nu \gtrsim 2.5$. In Fig. 3.7(b) various patterns can be discerned, in particular a splitting at 5 T that persists for all filling factors and shows a shift of weight from the lower to upper resonance. These splitting do not seem to exist at 8 T (except possibly at $\nu = 0$) but are resurgent for $\nu = 1$ and 2 at 13 T. The gaps at 5 T, $\nu = 0$ and 13 T, $\nu = 2$ are each approximately 6.5 meV.

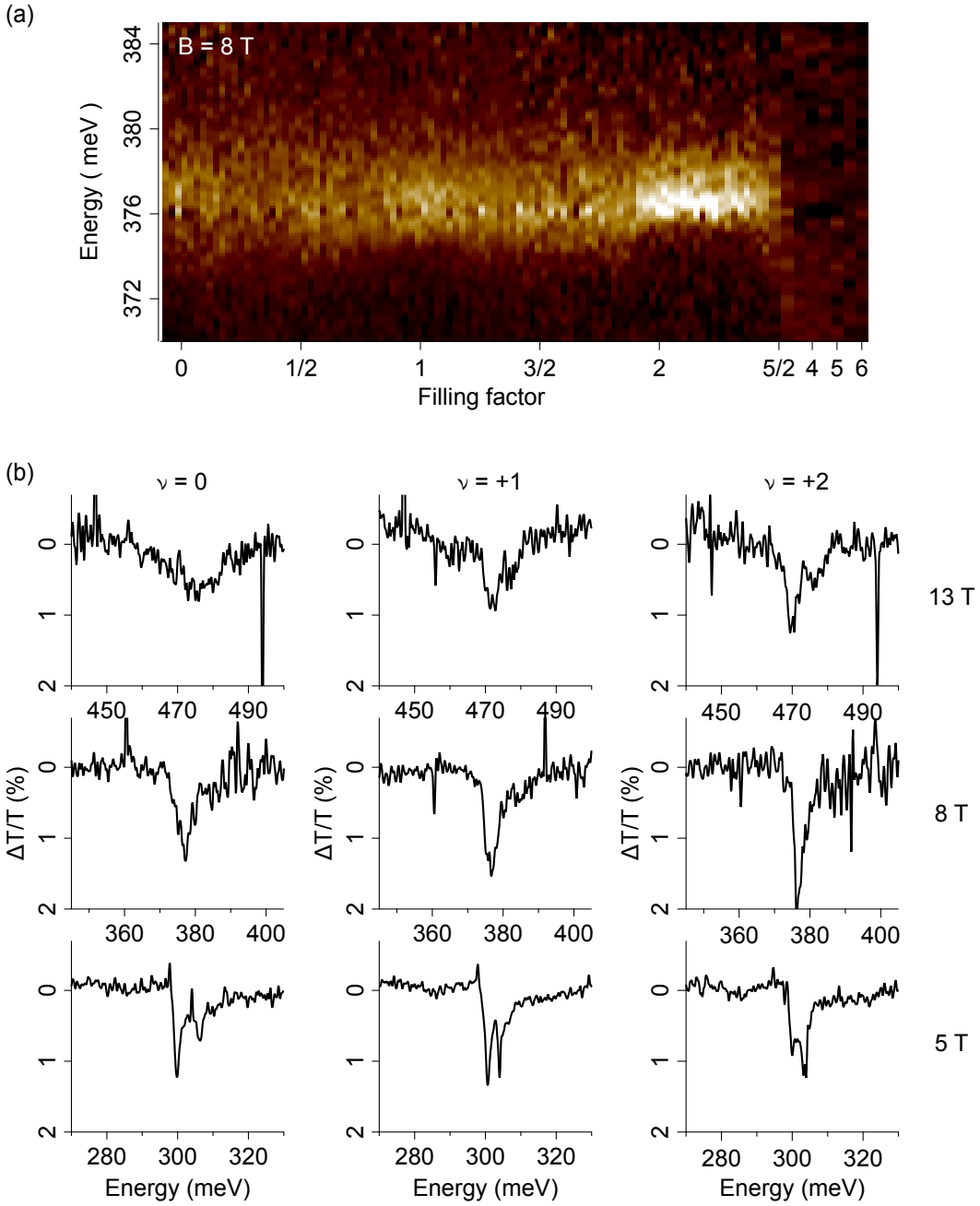

Fig. 3.7: (a) Colormap of T_3 at $B = 8$ T. (b) Linecuts vs filling factor and magnetic field.

3.2.5 Particle-hole asymmetry

In Fig. 3.8(a), we zoom out to show T_1 over an equal range of positive and negative filling factors and find a small but clear particle-hole asymmetry. For example, while the size of the $\nu = \pm 2$ splittings is virtually identical at 5.0 meV, the hole-side peaks lie a full 1.0 meV lower in energy. Moreover a closer look at $\nu = -1$ and $+1$ in Fig. 3.8(b) and (c) shows the two lower energy transitions are both separated by 1.7 meV and exhibit a slow ramp-up with increasing $|\nu|$, but the hole-side pair is found 1.1 meV lower than the electron-side pair. Meanwhile, the two higher-energy peaks on the hole side nearly overlap, compared to $\nu = +1$ where we have seen they are individually resolved. Additionally, the relative shift of these higher-energy peaks with increasing $|\nu|$ shows opposing trends near $\nu = -1$ and $+1$, with both pairs lying close together at the left side of the graphs (more negative ν) and separating toward the right (for more positive ν), breaking $\nu \to -\nu$ symmetry. Finally, the highest energy peak on the hole side is only 0.4 meV lower than the electron side. Relative to the CR energy, this symmetry breaking is a $\sim 0.8\%$ effect, too small to have been noticed in early broadband spectroscopic studies [28] but matching an asymmetry apparent in the data of Ref. [38, 42]. However, in terms of the many-particle-enhanced valley and spin gaps, these small shifts are quite significant. For instance, applying the same analysis used in the discussion of Fig. 3.3, we find for $B = 8$ T that $\Delta v^{\nu=-1} = 5.7$ meV; $\Delta z_+^{\nu=-1} = 1.2$ meV (or effective g-factor $g^*_{z;+} = 2.6$); and $\Delta z_-^{\nu=-1} = 6.7$ meV ($g^*_{z,-} = 14.4$).

Such particle-hole asymmetry is not predicted by many particle theories to date but may arise at the single-particle level due to next-nearest-neighbor hopping [90]. In this picture, a field-dependent asymmetry between the $-n \to n-1$ and $1-n \to n$ transitions was derived for the high-n limit in Ref. [91], giving $E_{asym} = 3\sqrt{2}\hbar\omega_c t' a/t l_B \approx 0.56$ meV at 8 T (where t (t') is the nearest (next-nearest) neighbor hopping, and a the C-C atom distance

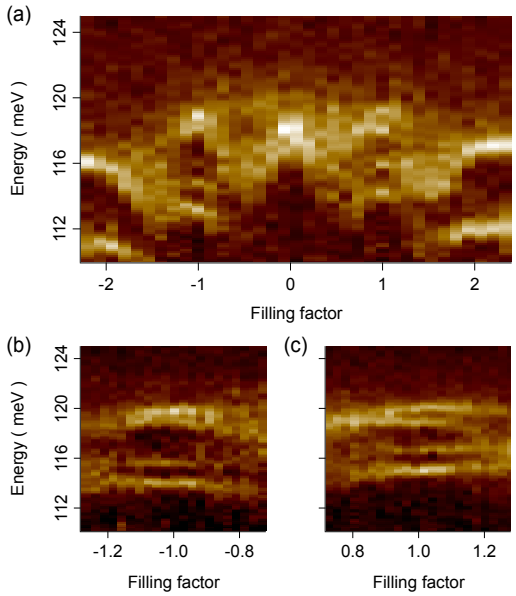

Fig. 3.8: (a) Closeup of T_1 transition from Fig. 3.2(a), showing a clear asymmetry for positive vs. negative filling factors. (b) and (c) show higher resolution (finer abscissa spacing) maps at $\nu = -1$ and $+1$, respectively, revealing particle-hole symmetry breaking in the four-fold splittings.

in graphene). This value lies within a factor of two of the asymmetry energies seen here, suggesting we are seeing an intrinsic property of the underlying band structure. In contrast, far larger particle-hole asymmetries up to a few percent of $E_{0,1}$ have been reported in swept-field CR studies of graphene-on-oxide, monolayer and multilayer epitaxial graphene, and encapsulated graphene with double moiré potentials [40, 77, 92, 93].

3.2.6 Many body contribution to CR energies

In Figure 3.9(a) the transition energies at $\nu = 0$ and 8 T are plotted as a function of transition number T_i, parameterized as an effective velocity $v_{eff}(T_i) = \Delta E^{meas}(T_i)/\Delta E^{calc}(T_i)[v = 10^6; \mu = 0]$. We see that v_{eff} rises from T_1 to T_2 and thereafter gradually decreases in agreement with previous measurements [42]. We fit these data in two ways: first, in the

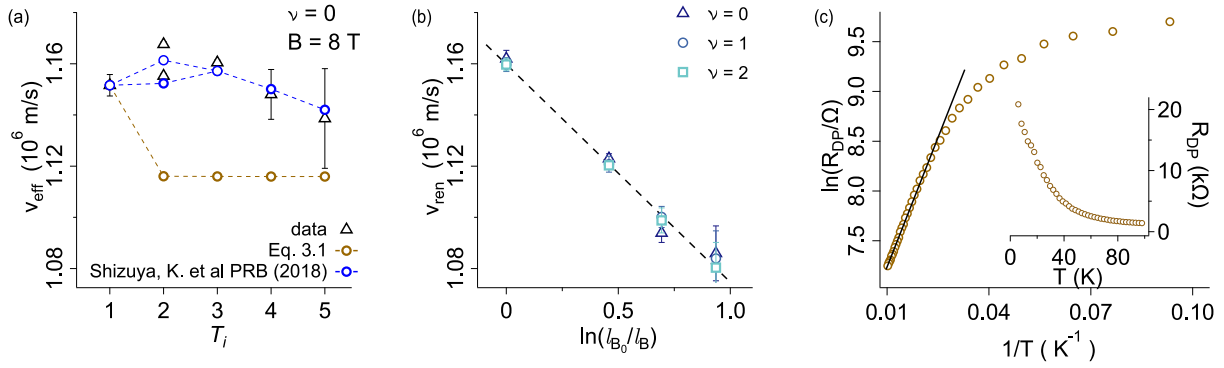

Fig. 3.9: (a) The transition energies parameterized as effective velocities $v_{eff} = \Delta E^{meas}(T_i)/\Delta E^{calc}(T_i)[v = 10^6; \mu = 0]$ at $\nu = 0$. (b) The renormalized Fermi velocity v^{ren}, extracted from fits to the theory of Ref. [85] (c) Arrhenius plot of the device resistance at charge neutrality and zero magnetic field

basic non-interacting picture with energies given by Eq. 3.1, using fixed band velocity v and mass μ (with μ set to the splitting at $\nu = 2$). This model clearly does not capture the measured variation in v_{eff}. Far better results are found using the theory of Ref. [85] which accounts for many-particle contributions to CR in a single-mode approximation [94]. The fit has three parameters: an interaction-renormalized band velocity v^{ren}, the Dirac mass, and an overall Coulomb interaction we fix at $V_C = \sqrt{\pi/2}\ e^2/(4\pi\epsilon l_B) = 50$ meV [1]. This provides a good account of the variation in v_{eff} vs. T_i and also the size of the T_2 splittings and yields $v_{ren} = 1.105 \times 10^6$ m/s and $M = 2.76$ meV, close to the value at $\nu = 2$. Carrying out this procedure at other magnetic fields and filling factors yields the v^{ren} values in Fig. 3.9(b). There, the resulting linear decrease against $\ln(\sqrt{B/B_0})$ is anticipated in Ref. [34], which predicts the slope is given by $-(\alpha c/4\epsilon)$ where α is the fine structure constant and c the speed of light. This running of the velocity with B is the generalization to the finite field

[1] The curve fits are not sensitive to the precise value of V_C. Specifically, changing the value of ϵ in V_C results in different values of v^{ren} returned by the fits in Fig. 3.9(a); but the slope of the new v^{ren} vs $\ln(l_{B_0}/l_B)$ is unchanged. That is, the relative variation of the measured v_{eff} at different fields has physical meaning independent of the particular renormalization employed, as discussed in Ref. [34, 85]

of the interaction-renormalized band velocity predicted before graphene was isolated [95] and seen in electronic transport [96]. The slope determines a dielectric constant of $\epsilon = 6.4$, which is likely dominated by the in-plane ϵ of hexagonal boron nitride [97], and is in good agreement with magneto-Raman measurements [36].

In Fig. 3.9(b) we show the extracted values of v_{ren} for multiple magnetic fields and filling factors. These data show no significant variation of v_{ren} with filling factor and reveal the predicted linear decrease with $\ln(l_{B_0}/l_B)$, in agreement with prior magneto-Raman studies [36].

3.3 Discussion and Summary

We analyze the data at $\nu = 2$ using two approaches and predict v_{eff} for the $\nu = 0$ data with the resulting fit parameters. First, we fit the data with the gapped but non-interacting model using Eq. 3.1 and find the velocity $\tilde{v} = 1.116 \times 10^6$ m/s and the Dirac mass $M = 2.51$ meV. By design, the splitting at T_1 is well-matched, but otherwise, this approach fails badly for both the $\nu = 2$ and $\nu = 0$ data. We find much better results with the theory of Ref. [85] that accounts for many-particle contributions to CR in a single-mode approximation [94]. The fit parameters are the velocity and mass and include an overall Coulomb interaction $V_C = \sqrt{\pi/2}\, e^2/(4\pi\epsilon l_B) = 50$ meV set by choosing $\epsilon = 4$ for h-BN [98]. This theory provides a good account of the variation of v_{eff} and the T_2 splittings using $\tilde{v} = 1.105 \times 10^6$ m/s and $M = 2.76$ meV. However, no single set of parameters can simultaneously match the T_1 data at both $\nu = 0$ and $\nu = +2$. This is presumably due to the limited version of Kohn's theorem active in the theory of Ref. [85], but not the data. The valley gap (extracted in the discussion of the LL schematic of Fig. 3.3, is 7.3, 5.0, and 5.0 meV for $\nu = 0, 1$, and 2, respectively. We note the h-BN-induced gap in graphene is expected to be enhanced by interactions at

half-filling [86, 99, 100], as we observe. Interestingly, these values are smaller than the 15 meV gap extracted from measurements of the thermally activated transport at zero field and half-filling, shown in Fig. 3.9(c). This discrepancy is not surprising due to the prediction that exchange interactions do not impact the T_1. However, it is not yet clear if CR of the T_1 transition sees the full strength of interaction contributions. On the other hand, the linear fit in Fig. 3.9(c) covers rather less than an order of magnitude change in temperature, so the gap size extracted from transport may not be accurate.

In a translationally invariant system with a parabolic dispersion, the energy of the long-wavelength $q = 0$ magnetoplasmon mode of the CR excitation is pinned to the LL separation $\omega_c = eB/m^*$, as required by Kohn's theorem [30, 31]. However, in practice band non-parabolicity [101–103], disorder [104, 105], multiple effective masses [106, 107], intense irradiation [108], or intentional breaking of translation invariance [109–111] all allow for many-particle contributions to the CR energy. Yet these end-runs around Kohn's theorem inevitably include effects beyond interactions [31, 102], due to whichever mechanism is used to evade it. In contrast, the linear Dirac dispersion of graphene can be considered an extreme case of non-parabolicity where the carriers have no center of mass, and Kohn's theorem ought no longer apply [27, 32–35]. In fact a limited version of the theory does survive, although just for transitions between the evenly-spaced $n = 0$ and ± 1 LLs, for which the direct Coulomb and exchange interactions cancel and leave just the overall renormalization of the band velocity [27, 34, 85, 87]. For all other transitions, it should be possible to directly observe interaction contributions to the magnetoplasmon spectrum, promising that minimally-disordered graphene devices can become a laboratory for exploring the excited states of interacting many-particle systems. However, our findings suggest that transitions involving the $n = 0$ LL exhibit clear evidence of symmetry-breaking and many-particle contributions, implying the breakdown of even this residual aspect of Kohn's theorem.

When applied to graphene, cyclotron resonance becomes a novel tool for spectroscopy of many-particle physics since Kohn's theorem no longer applies. Here, it enables us to follow the evolution of many-particle enhanced gaps in the broken symmetry regime of clean monolayer graphene, where we find a Dirac mass that is significantly enhanced at half-filling of the zeroth LL and Zeeman gaps both at and below the Fermi energy that are enhanced by direct or indirect exchange effects. These observations highlight the importance of lattice-scale interactions coupling the K and K' valleys in graphene. Moreover, a very small but finite particle-hole asymmetry is seen that underscores the device quality and sets upper limits on the symmetry of the linear dispersion in graphene. These results promise that with continually improving device fabrication techniques, it will soon be possible to perform spectroscopy of excited states in the fractional quantum Hall regime.

Chapter 4

Infrared Spectroscopy of Graphene/h-BN Moiré Superlattice

4.1 Introduction

In a spatially periodic lattice with lattice spacing a, electrons are described by Bloch bands. When subjected to a strong magnetic field, the electronic spectrum quantizes into discrete, highly degenerate Landau levels. The magnetic field B introduces a key length scale to the problem: the magnetic length $l_B = \sqrt{\hbar/eB} \approx 25.7 \text{ nm}/\sqrt{B}$, where $\hbar$ is Plank's constant divided by 2π, e is the electron charge. When the two characteristic lengths l_B and a become commensurate, electrons exhibit a complex self-similar energy spectrum called Hofstadter's butterfly [51]. However, achieving the commensurability conditions in typical crystals requires unfeasibly high values of B, in excess of 10,000 T. The main experimental effort, therefore, has been to define artificial superlattices. Patterned GaAs/AlGaAs heterostructures with 100-nm-period gates provided the first experimental evidence of the Hofstadter spectrum [112–115]. However, the limited range of carrier density in these samples has made it challenging to map the complete spectrum.

An important advancement in 2D vdW materials is layer-by-layer stacking of heterostruc-

tures. The lattice mismatch of these layered crystals provides an additional degree of freedom during fabrication: the twist angle between their crystallographic axes. Although the interlayer interaction between stacked 2D crystals is relatively weak, the extension of electron orbitals beyond the crystal plane affects charge carriers in neighboring 2D crystals. This manipulation results in moiré patterns, which vary based on the rotational angle between the joining crystals and their lattice mismatch.

In the case of graphene on h-BN, 1.8 % lattice mismatch between the two crystals and any misalignment between their respective crystallographic axes generate a large-scale quasi-periodic hexagonal pattern, known as the moiré superlattice (mSL). The perturbing effect of the moiré superlattice on Dirac electrons in graphene decreases with increasing misalignment between the h-BN and graphene lattices. Perfect crystallographic alignment (0°) of this layered structure leads to a maximum moiré wavelength λ of 14 nm. Figure 4.1a shows the critical value of the magnetic field B_0 for a hexagonal superlattice, meeting the condition when the magnetic length approaches the scale at which there is approximately one flux quantum per unit cell ($\Phi/\phi_0 \rightarrow 1$). Here Φ is the magnetic flux penetrating the superlattice unit cell, $\phi_0 = h/e$ is the magnetic flux quantum, and $A = \sqrt{3}\lambda^2/2$ is the area of the superlattice unit cell. With a superlattice wavelength of 14 nm, the critical field where $\Phi/\phi_0 \rightarrow 1$ condition is met is ≈ 25 T, a value achievable in lab-scale experiments. Therefore, G/h-BN heterostructures are well suited to investigate the Hofstadter phenomenon.

The long-wavelength periodic potential in the mSL induces Bragg scattering of electrons in graphene [116], which alters the electronic properties of graphene. As illustrated in Figure 4.1b [48], this potential gives rise to a miniband structure with the most significant effects observed at the edges of the first and second minibands. Here, the perturbation of the superlattice leads to the formation of secondary Dirac points (DPs). Spectral reconstruction occurs near the edges of the superlattice Brillouin zone (SBZ) and is characterized by a

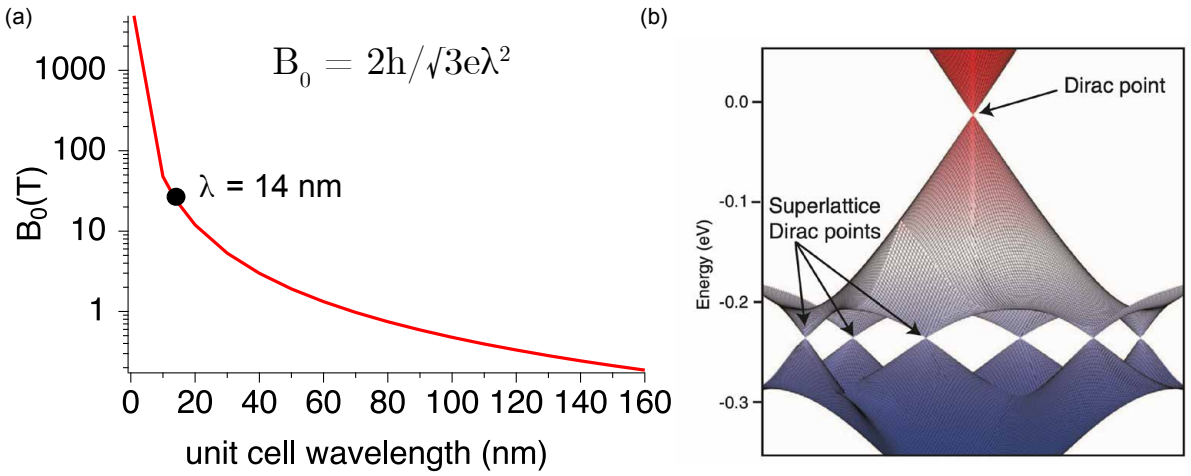

Fig. 4.1: (a) Critical field versus unit cell wavelength defined where the ratio $\Phi/\phi_0 \to 1$. (b) Energy of the valence bands showing the original Dirac point and the emergence of new superlattice Dirac points [48].

wavevector $G = 4\pi/\sqrt{3}\lambda$ and energy $E_S = \hbar v_F G/2$, where λ represents the moiré wavelength and v_F denotes the Fermi velocity of graphene. To observe the effects moiré minibands in transport measurements, graphene should be doped to a carrier density $n_s = 4\pi/3\lambda^2$ to ensure that the Fermi energy lies in the reconstructed portion of the spectrum. Longitudinal resistivity [52] measurements in graphene typically reveal the emergence of secondary peaks appearing symmetrically on either side of the main peak at the charge neutrality point at high doping levels (near E_S). These secondary peaks are attributed to the formation of minibands due to the mSL induced by h-BN. In the presence of a magnetic field, a series of Landau levels originate from multiple mini-replicas of the original spectrum that appear at rational flux values of $\Phi/\phi_0 = p/q = \alpha$, where p and q are integers [74]. Alternatively, the energy diagram is parameterized so each Landau level splits into p sub-bands at these rational values.

As previously discussed in Chapter 1, Wannier provides a simplified description of Hofstadter's energy-field diagram using a density-field diagram. The Wannier diagram has been

realized experimentally [52, 74], with transport probes, where statistical weight W in the Wannier diagram and α are accessed using charge carrier density and magnetic field. Wannier demonstrated that all spectral gaps follow linear trajectories in the density-field space, described by a dimensionless Diophantine equation

$$\frac{n}{n_0} = t\frac{\Phi}{\phi_0} + s, \tag{4.1}$$

where normalised density n/n_0 required to fill an entire bloch band, and s and t are topologically invariant integers. The Diophantine equation represents a universal set of constraints describing all possible gaps within the Hofstadter spectrum. The gaps that remain open for a particular device depend critically on the degeneracy of the system and lattice geometry. In the quantum Hall regime, spectral gaps appear as minima in longitudinal resistance (R_{xx}) and quantized plateaus in the transverse Hall resistance (R_{xy}) [117], as we will discuss in the following section.

Since the Wannier diagram loses information about the associated energies of the gap, this strongly motivates this work to probe the self-similar energy-field diagram directly employing cyclotron resonance measurements. This work uses infrared magneto-spectroscopy to investigate cyclotron resonance within the Hofstadter butterfly regime in G/hBN heterostructures. Infrared spectroscopy has proven to be a highly effective tool for probing the Landau level spectrum and, consequently, the band structure of graphene.

Our investigation begins with analyzing the moiré wavelength in the G/h-BN heterostructure using magneto-transport measurements, revealing a rotational alignment of 0.5 degrees. Electron-electron interactions in graphene and the incommensurability of G/h-BN heterostructures break the A-B sublattice symmetry in graphene, resulting in a gap in the otherwise gapless band structure of graphene. This gap is tunable by the superlattice wave-

length. Our optical study provides a direct spectroscopic determination of the gap by measuring the splitting of the Landau level transition peaks at a finite magnetic field. The maximum gap size is 12 meV for 0.5° rotational alignment. A key focus of this chapter is a systematic investigation of interband cyclotron resonance transitions across varying magnetic field strengths to understand the self-similar behavior of the Landau levels. Our findings reveal transitions not previously reported in monolayer graphene and likely attributable to the fractal nature of the LLs. Moreover, we identify asymmetric cyclotron resonance line shapes reminiscent of Fano resonances, which appear periodically in the magnetic field. These results enrich our understanding of the strong reconstruction of the Landau levels in the Hofstadter butterfly regime.

4.2 Experiment

4.2.1 Device architecture

We mechanically exfoliate monolayer graphene and h-BN flakes from bulk crystals with well-defined crystalline edges. Initially, we focus on achieving the controlled alignment between hBN and graphene. Both graphene and hBN consist of hexagonal sheets, allowing the optically straight edge of a graphene flake (or h-BN) to represent two crystallographic orientations, zigzag or armchair, as shown in Figure 4.2a. An optical alignment technique achieves the G/hBN moiré pattern by aligning the straight edges between graphene and hBN. The layered structure of G/h-BN, with nearly perfect alignment of the crystallographic axis, can form two basic moiré patterns: 0° and 30°. Aligning the straight edges yields a 50% of close to 0° alignment. This variability stems from the possibility of unintentionally aligning the zigzag (armchair) edge of graphene with either the zigzag (Z) or armchair edges (A) of h-BN.

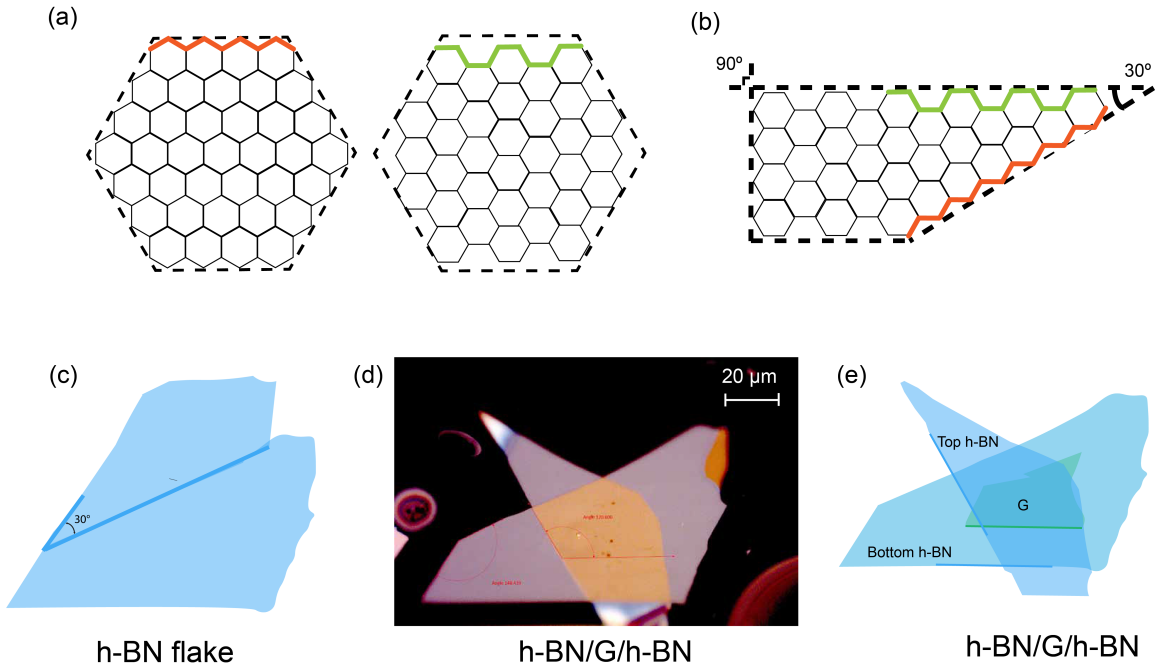

Fig. 4.2: (a) Two different crystallographic edges of a hexagonal sheet: red marks the zigzag edge, and green marks the armchair edge. (b) Orientation angle-dependent edges. (c) An example of an h-BN flake with straight edges. (d) Optical microscope image of the stack on a transfer slide. (e) The tear-and-stack technique involves tearing h-BN into two flakes, after which the highlighted straight edge of graphene is aligned with both torn h-BN flakes.

To overcome this challenge, we adopt a tear-and-stack approach [118], wherein we tear a single flake of h-BN having two straight edges at an angle of 30° into two pieces, as illustrated schematically in Figure 4.2c. The straight edge of the graphene flake is aligned with both torn flakes, guaranteeing one of the two aligned edges is Z-Z or A-A. Fig. 4.2d presents an optical image of such a stack, highlighting the straight edges of three flakes, with one torn flake used as the top h-BN and the other as the bottom h-BN to fully encapsulate graphene. The sample in this study comprises a 450 μm^2 sheet of monolayer graphene encapsulated with an approximately 40-nm-thick flake of h-BN, assembled using a dry-stacking technique and placed on a few-layer thick graphene. The layered stack is transferred to a lightly doped,

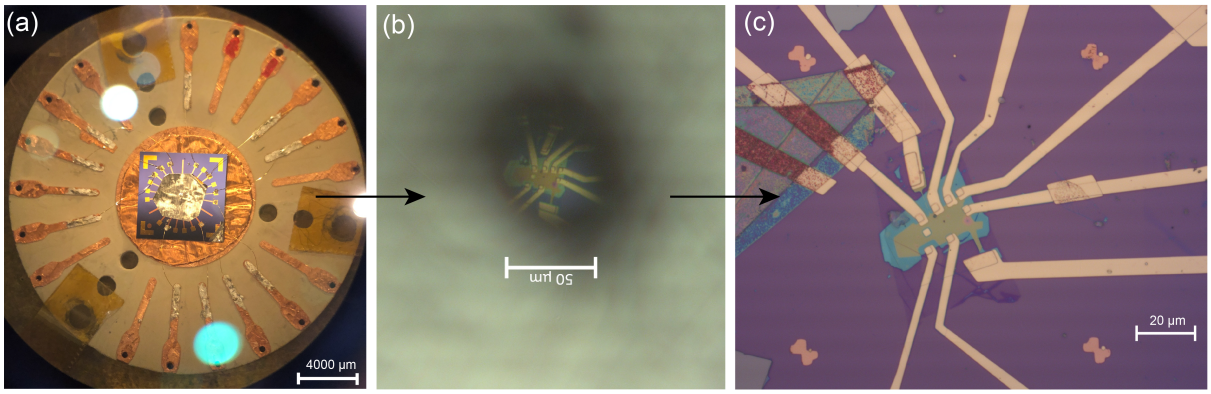

Fig. 4.3: (a) Device on an oxidized silicon wafer wired to a sample mount with ~ 90 μm top aperture. (b) Optical microscope image of the device through the top aperture. (c) Magnified image of the encapsulated device with electrical leads

oxidized Si wafer. We establish electrical contacts to graphene using 3/60-nm-thick films of Cr/Au. We utilize the graphene etch-stop technique [119] to selectively expose and contact the embedded graphene layer, with hBN being etched using XeF_2 gas. We align the finished device over a copper foil aperture $\approx$ 1 mm in diameter and hand-solder it to the sample puck. Before loading the sample into the dilution fridge, we place a second aluminum foil aperture with a diameter of ≈ 90 μm centered over the device. Images of these steps are shown in Figure 4.3. Appendix B discusses more details of the steps involved in the device fabrication.

4.2.2 Transport

4.2.2.1 Zerofield transport

We conduct four-terminal resistance measurements at mixing chamber T = 80 mK shown in 4.4a. In addition to the typical resistance peak at the charge neutrality point at gate voltage $V_g \approx$ -34 mV, two additional satellite resistance peaks emerged, symmetrically positioned at $V_{satl} \approx \pm$ 8V relative to CNP. These satellite features agree with previous transport

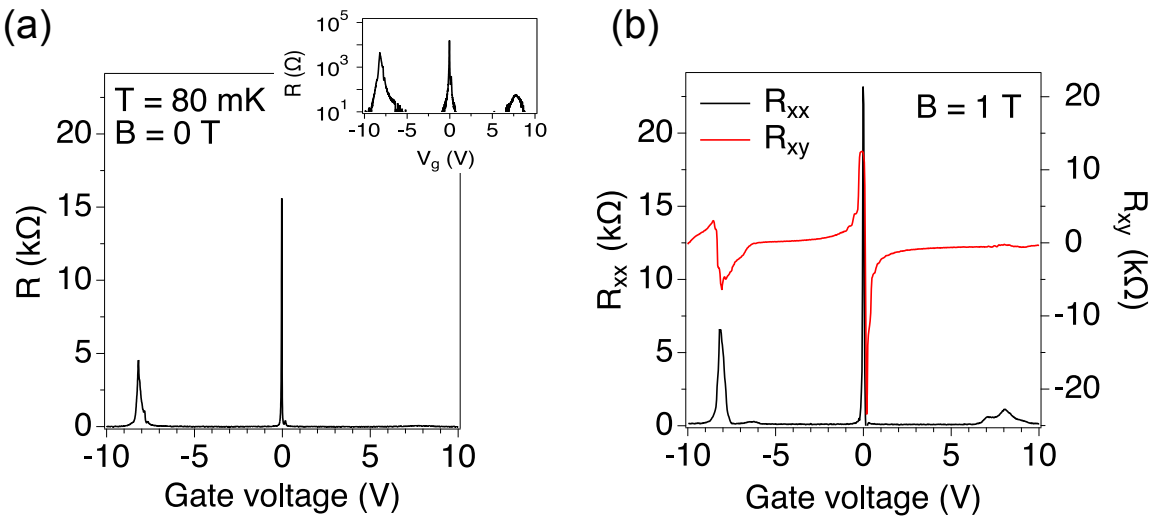

Fig. 4.4: (a) Four terminal resistance versus gate voltage at zero magnetic field. Inset: Resistance in log scale indicating peak at CNP and two additional satellite peaks. (b) Longitudenal resistance R_{xx}(left) and Hall resistance R_{xy} versus gate voltage at B = 1T and T = 80mK. The Hall resistance shows sign changes at mDP as well as sDP.

measurements [52, 74, 117] of single-layer graphene coupled to a moiré superlattice. In Figure 4.4b, we plot longitudinal resistance (R_{xx}) and transverse Hall resistance (R_{xy}) against gate voltage at $B = 1$ T. Near the primary CNP, the Hall resistance undergoes a sign change as the Fermi energy transitions from the electron band to the hole band. A similar feature is observed near V_{satl}, as the Fermi energy crosses through a second band edge. This observation proves that the moiré pattern, acting as a periodic potential superlattice, gives rise to a mini-Brillouin zone band. Additionally, we observe that the satellite peak is more prominent on the hole side than the electron side, consistent with previous experimental and theoretical findings [120, 121].

We determine the moiré wavelength from the location of the satellite resistance peak

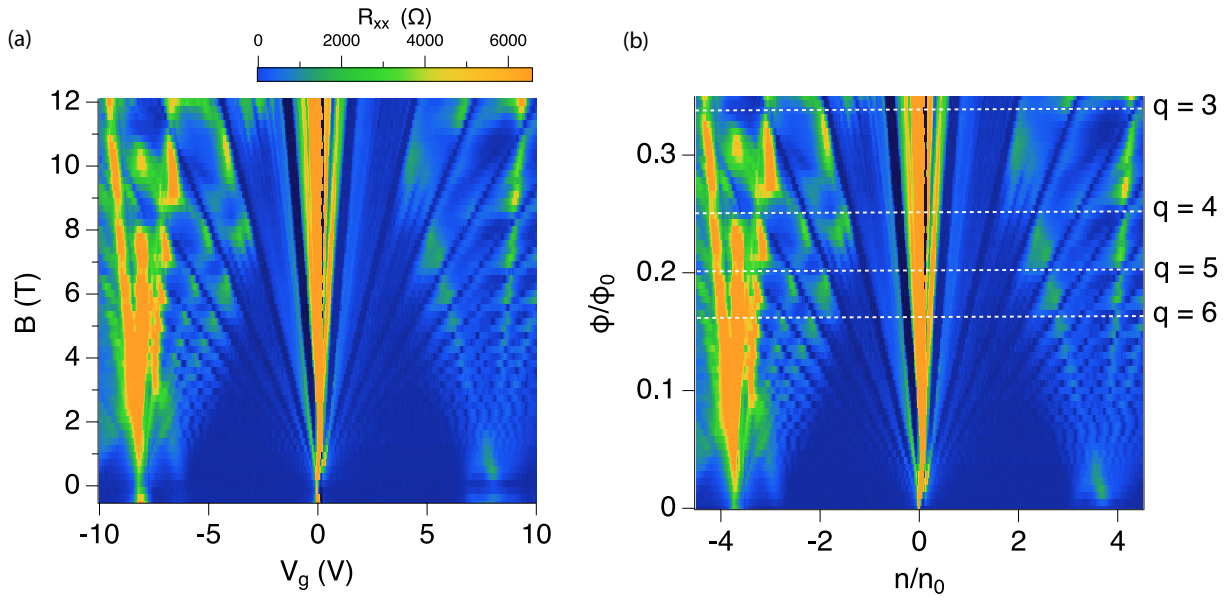

Fig. 4.5: (a) 2D map of four-terminal longitudinal resistance plotted against gate voltage and magnetic field. (b) The same data is represented in terms of dimensionless parameters, normalized carrier density and magnetic flux. The intersections between the central and satellite fans occur at $\Phi/\phi_0 = 1/q$.

V_{satl}. Assuming hexagonal symmetry filled band model:

$$\frac{n_s}{n_0} = g_s g_v, \tag{4.2}$$

where n_s is the field-effect density at the satellite peak positions, $n_0 = 1/A$ where $A = \sqrt{4}\lambda^2$ is the unit cell area of the moiré pattern, g_s is the eelctron spin degenracy and g_s is the valley, or pseudospin degeneracy. For the device mentioned in this work, the satellite peak appears at $\pm 8V$ as shown in 4.4, giving moiré wavelength of 12.56 nm. Using 1.33, we find rotational angle of $\approx 0.5°$.

4.2.2.2 Magneto-transport

Figure 4.5a represents longitudinal resistance measured as a function of magnetic field and gate voltage. Following the Diophantine equation 4.1, near the charge neutrality point in the weak-field regime, as shown in Figure 4.5b, we observe a typical Landau fan diagram where the trajectories of the energy gaps originate from the charge neutral point at $B = 0$ (i.e., $s = 0$). However, in a fractal band regime, we observe different trajectories with non-zero intercepts ($s \neq 0$) at $B = 0$, consistent with previously observed transport measurements. The intersections between the central and satellite fans occur at $\Phi/\phi_0 = 1/q$.

While transport measurements have been widely employed to access the Hofstadter's butterfly, spectroscopy of the fractal levels in graphene-hBN have not been explored much to date [77, 122].

4.2.3 Tunable gap in graphene superlattices

The coupling between carbon atoms in graphene and boron and nitrogen atoms in boron nitride is significant, ranging from 300 to 450 meV. This coupling enables substrate-induced distortions of the isolated graphene electronic structure when placed on a hBN substrate. Interacting Dirac particles exhibit varying responses to different external potentials. A scalar potential, which is insensitive to sublattice structure, induces interactions that produce a polarization effect, screening the potential. Conversely, a potential influenced by pseudospin, associated with the A-B sublattice modulation, triggers interactions that amplify the potential. This amplified potential leads to pseudospin-dependent Bragg scattering, resulting in gap formation at the Dirac point, denoted as Δ_0 at the charge neutrality point.

A visual representation of graphene/hBN moiré superlattice is shown in figure 4.6a with the red, blue, and black solid circles corresponding to boron, nitrogen, and carbon atoms.

An example of a superlattice cell is outlined in a yellow-shaded hexagon. The interplay between electron-electron interactions in graphene and the incommensurability of G/h-BN heterostructures breaks the A-B sublattice symmetry. Despite the weak interaction of graphene with the h-BN substrate when the honeycomb lattices of graphene and hBN are nearly perfectly aligned, the strengths of electronic couplings increase substantially and give rise to an energy gap Δ_0 at the charge neutrality point, introducing an effective mass for the Dirac fermions. This gap is tunable by the superlattice wavelength, offering opportunities for engineering interaction effects in graphene. The wavelength in moiré superlattices can be as long as 100 atomic distances, depending on both the lattice mismatch δ and twist angle θ between graphene and h-BN, $\lambda(\theta) \approx \lambda_0\delta/(\theta^2 + \delta^2)$. This gap is theoretically predicted to have a power law scaling given by the equation

$$\Delta_0(\theta) = \left(\frac{\lambda(\theta)}{a}\right)^{0.27}, \tag{4.3}$$

where a = 1.42 Å is the carbon-carbon spacing.

The effect of different local potentials generated by boron and nitrogen atoms, which induce local gaps, varies spatially. Theoretically, this variation is expected to be nearly averaged in a local moiré superlattice. However, the moiré potential breaks the inversion symmetry, resulting in a global spectral gap observed at CNP through transport studies. While ab initio theory [70] predicts significant gaps of approximately 50 meV when the two honeycomb lattices are perfectly aligned, deviations due to misorientation or lattice constant mismatch drastically reduce electronic coupling, leading to smaller gaps. Nonetheless, the substantial gaps observed at the CNP in graphene/h-BN heterostructures are not solely attributed to the orientation-dependent moiré pattern. Instead, the origin of the gap requires both orientation-dependent structural relaxation of the carbon atoms and nonlocal many-

body exchange interactions among electrons. The gapped spectrum and the tunability of the associated effective mass provide a new design parameter in the study of many-body effects in monolayer graphene.

Theoretically calculated [123] single-particle gaps, accounting for lattice relaxation effects, are estimated to be around 7 meV for rotational alignment. Various experimental techniques confirmed the emergence of energy gaps at the CNP in graphene/h-BN moiré superlattices, revealing significant variation in the measured gap values. Thermally activated gap [117] values obtained from transport measurements reach a maximum of around 30-40 meV. Capacitive probes [74] have measured a gap of $\approx$ 25 meV for perfectly aligned heterostructures of G/h-BN. On the other hand, electron tunneling spectroscopy observations [124] show a smaller gap size of around 16 meV, lower than that measured by conductance or thermodynamic probes.

In this work, we study the precise determination of energy gaps through magneto-optical spectroscopy of graphene/h-BN heterostructures. This involves monitoring cyclotron resonance in an external magnetic field. Similar to previous chapters, we measure cyclotron resonance by recording broadband infrared transmission through the device across various gate voltages or carrier density values (n). The control of n in the presence of a magnetic field B allows us to control the Landau level filling factor, $\nu = nh/eB$, where h represents Planck's constant.

Without Zeeman interaction, the Landau levels exhibit complete valley and spin degeneracy in pristine graphene due to intrinsic inversion symmetry. Consequently, the quantized Hall conductivity can only take on values of $4m + 2$ (where m is an integer). In the G/h-BN system, the valley degeneracy is broken by the inversion-asymmetric potential introduced by h-BN, leading to an energy gap in the zeroth Landau level. This gap does not lift the

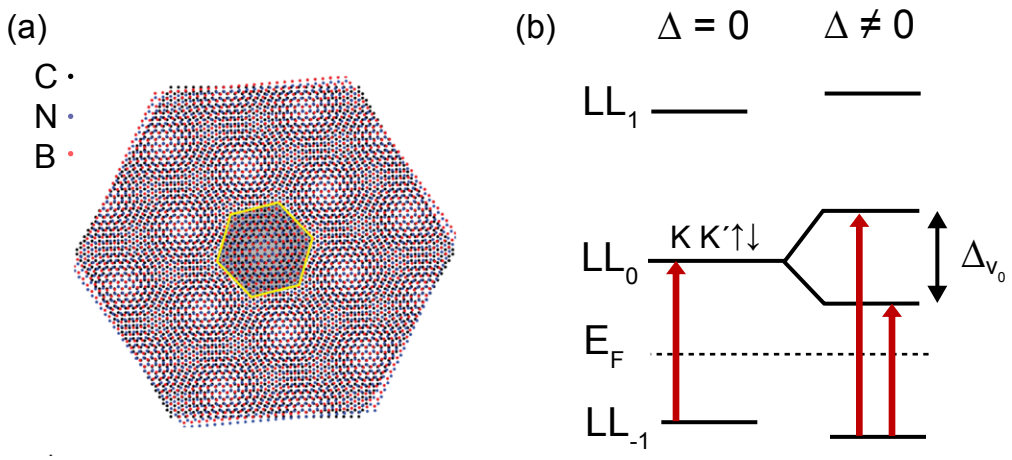

Fig. 4.6: (a) Schematic of the graphene/hBN moiré superlattice. (b) Active resonance channel for pristine graphene versus gapped graphene. Finite Δ causes lifting of the four fold-degeneracy of zeroth Landau level, giving rise to valley polarized zeroth LL and access to two CR transitions.

Landau level degeneracy for $|N| > 0$ but induces a shift according to

$$E_N = \pm\frac{\Delta_0}{2} \pm N\sqrt{2e\hbar {v_F}^2 B|N| + \left(\frac{\Delta_0}{2}\right)^2} \tag{4.4}$$

where Δ_0 is the gap energy and N is the LL index. When the Dirac point in graphene is gapped by such an inversion-asymmetric potential, the zeroth Landau level of one valley adheres to the top of the gap, while the zeroth Landau level of the other valley attaches to the bottom of the gap. Consequently, a larger energy gap in the Dirac spectrum is always accompanied by a larger valley splitting of the LL in the presence of a magnetic field.

When the Fermi energy is situated between Landau levels $N = 0$ and $N = 1$ in pristine graphene, and there is no energy gap present in the presence of a magnetic field, optical transitions from $LL_0 \rightarrow LL_1$ become accessible following the inter-Landau level selection rule $\Delta|N| = \pm 1$. This transition exhibits a four-fold degeneracy. However, with the introduction of a valley gap, another inter-Landau level transition is initiated. As a result, the optical

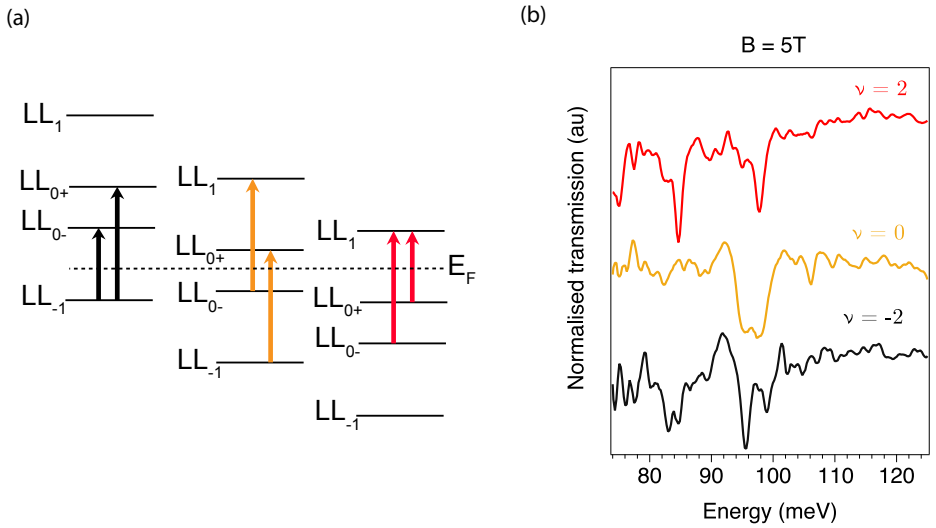

Fig. 4.7: (a) Schematic of transitions involving $N = -1, 0, +1$ LLs. The Fermi energy E_F is shown as a dotted line. Transitions associated with each of the filling factors are shown in different colors. (b) Allowed CR transitions (are offset for clarity) for three filling factors ν = -2, 0, and 2 appear as a dip in normalized IR spectra.

absorption spectrum displays two distinct transition peaks separated in energy by Δ_{v_0}, as illustrated schematically in Figure 4.6b.

In Figure 4.7a, we introduce schematics representing the simplest model of transitions involving $N = -1, 0, +1$ LLs that align with the obverse CR transitions. The schematics are drawn for ν = -2, 0, and 2, with greatly exaggerated level shifts and energy gaps. Figure 4.7b examines the inter-band Landau level transition T_1 for three filling factors ν = -2, 0, and 2 measured at $B = 5$ T. The CR transition is visible as a dip in all traces. At $\nu = 0$, when the Fermi energy resides in the zeroth Landau level, we observe a single resonance originating from the partially filled zeroth LL ($LL_{0(-1)} \rightarrow LL_{1(0)}$). Transitions at $\nu = 0$ are degenerate because of spin and valley degenerate $N \neq 0$ levels. At $\nu = 2$, as the Fermi energy is further adjusted to lie between $N = 0$ and $N = 1$ LLs, two distinct resonances are observed, widely separated by an energy greater than the peak width. These transitions stem directly from

the lifting of valley degeneracy and splitting of the ZLL ($LL_{0^+} \rightarrow LL_1$ and $LL_{0^-} \rightarrow LL_1$). By measuring the peak energies of these transitions, we can determine the valley gap to be $\approx$ 12 meV. We anticipate observing two distinct transitions ($LL_{-1} \rightarrow LL_{0^-}$ and $LL_{-1} \rightarrow LL_{0^+}$) when the Fermi energy is positioned between $N = -1$ to $N = 0$ LLs, corresponding to ν = -2. However, we observe a more complex structure reflecting additional distinct peaks. This observation suggests a significant electron-hole asymmetry, anticipated from the moiré superlattice, which will be discussed in later sections of this chapter.

We further examine the valley gap values obtained from Landau level transitions, comparing them with our previous studies [42] of cyclotron resonance (CR) in graphene. Figure 4.8 illustrates this comparison, focusing specifically on the gap value at $\nu = 2$ and $B = 8$ T. In our prior studies, the angle alignment of devices remained undetermined, as we did not observe signatures of satellite Dirac peaks. In CR measurements by B.J. Russell et al., the splitting of the T_1 transition was barely resolvable. However, clear splitting at $\nu = 2$ was observed in the work presented in Chapter 3 of this thesis. Notably, the maximum splitting of the T_1 transition is observed in the current work as shown in Figure 4.8. This trend is phenomenologically consistent with equation (4.3). Each transmission dip in the normalized spectra can fit well by a Lorentzian, shown by the black dashed lines in Figure 4.8. From these fits, we determine the peak positions of the resonances, and the difference in their values gives us the measured valley gap in the zeroth LL. The value of the gap energy from different experimental probes and *ab initio* calculation is summarized in 4.9.

4.2.4 Cyclotron resonance in the Hofstadter butterfly regime

Moon and Koshino calculated the band structure of the graphene/h-BN moiré system and analytically investigated several characteristic properties, as depicted in Figure 4.10. The

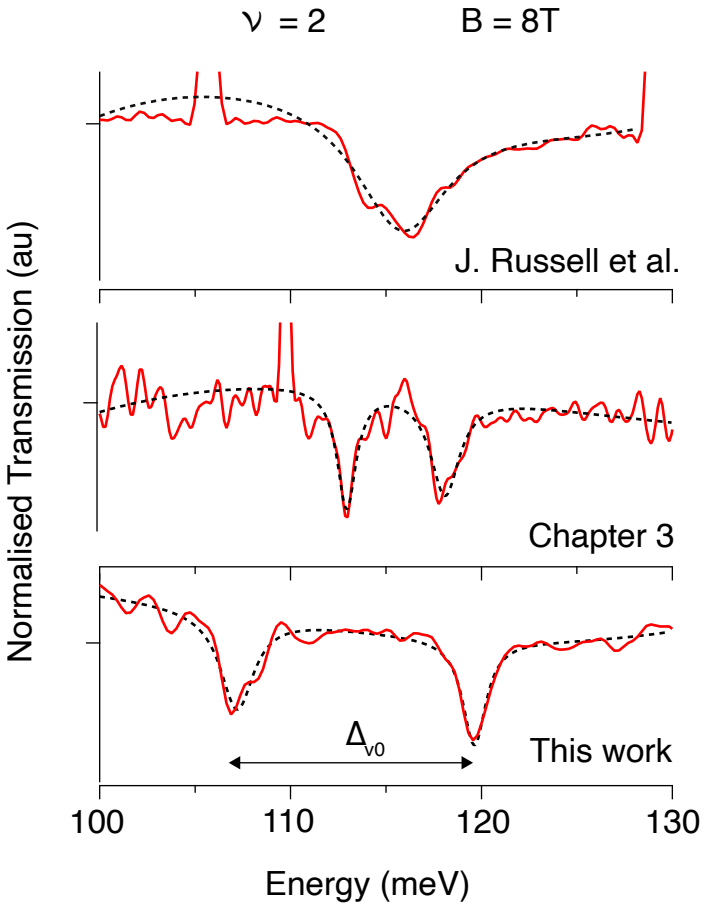

Fig. 4.8: Solid lines represent CR transitions measured for three different samples at $\nu = 2$ filling factor and $B = 8$ T. Dashed lines depict Lorentzian fits to the resonance. The splitting of the transition indicates the evolution of the valley gap, with negligible splitting observed in prior work[42]. A 4 meV splitting was observed in the work presented in Chapter 3 [125], while the current device exhibits the maximum splitting of ≈ 12 meV.

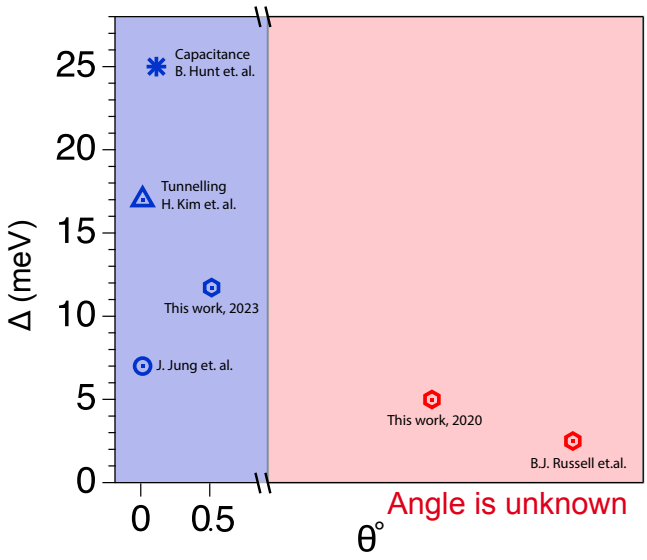

Fig. 4.9: Summary gap values extracted from Figure 4.8 and variation of gaps for different experimental probes and *ab initio* calculation [70].

black and red lines represent the spectrum for two valleys. The absence of spatial inversion symmetry in their calculation for the graphene-hBN heterostructure leads to the breakdown of the valley degree of freedom. In the presence of a magnetic field, the Landau levels of aligned graphene exhibit a hierarchical recursive pattern. The spectrum can be seen as Landau levels of intrinsic monolayer graphene on the electron side. Conversely, the monolayer Landau levels are significantly reconstructed on the hole side into a fractal spectrum. These findings serve as a strong motivation for this work. We aim to explore the self-similar energy-field diagram using cyclotron resonance measurements. In this thesis, our focus is on experimentally investigating these fractal levels using magneto-optical spectroscopy. This technique allows us to access the reconstructed energy levels by observing optical transitions across the Landau levels in graphene/h-BN moiré superlattice.

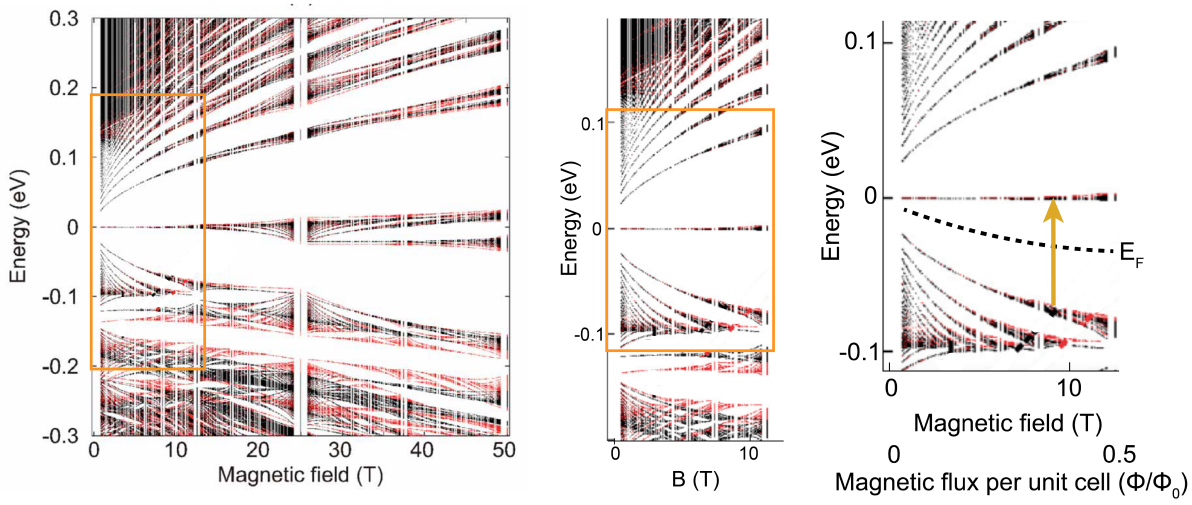

Fig. 4.10: (Left) Energy spectrum of monolayer graphene on h-BN system with an alignment angle of $\theta = 0°$ as a function of magnetic field strength. The red and black lines indicate the spectrum for the K and K' valleys, respectively [126]. (Middle) A closer look at the experimentally accessible region of the energy spectrum. (Right) Dashed-black line shows the position of the Fermi energy for filling factor $\nu = -2$. Arrow indicating the optical transition $LL_{-1} \rightarrow LL_0$.

4.2.4.1 Interband magneto-absorption

Figure 4.10, reprinted from [55], presents the Landau level spectrum derived from the continuum band model developed by Moon and Koshino, with a highlighted region relevant to our experimental investigation. The dotted lines in the right panel (added for clarity) indicate the position of Fermi energy for $\nu = -2$. In our study, to probe the fractal nature of the spectrum, we analyze optical transition T_1 denoted by the arrow and track its behavior as a function of magnetic field strength. Note that the position of the Fermi energy required for maintaining a constant ν shifts with increasing magnetic field. This shift occurs because LL filling factor ν depends on the magnetic field strength B and carrier density n ($\nu = eh/eB$), which governs the position of the Fermi energy. In their calculations, Moon and Koshino determined the single-particle gap (due to h-BN) of approximately $\sim$ 2meV. Consequently,

the valley splitting of the zeroeth Landau level is negligible and appears as a mixed state (red and black lines) in the spectrum 4.10 at $E \sim 0$ eV.

In Figure 4.11, we present CR transition T_1 for filling factor $\nu = -2$ and its development with increasing magnetic field, with each data point taken at intervals of 1/8 Tesla in the form of heatmap/colormap. As previously discussed, at a filling factor $\nu = -2$, the Fermi energy resides between the N = -1 and $N = 0$ LLs for monolayer graphene. Thus, we examine the optical transition $LL_{-1} \rightarrow LL_0$ from completely filled to completely empty Landau levels, for which interaction effects are minimized.

Due to the valley gap in the zeroth LL, we observe two distinct transitions, clearly identifiable in the colormap (Figure 4.11). The low-energy resonance displays a progression proportional to the square root of the magnetic field, consistent with Equation 4.3. However, the high-energy resonance at higher fields deviates from the expected $\sqrt{B}$ behavior. As illustrated in calculation 4.10, as the magnetic field increases, the Landau Levels (LLs) flatten out, diverging from the expected $\sqrt{B}$ behavior. This deviation corresponds to the observations in our spectroscopic measurements.

To seek intricate details down to the fractal nature of the levels, we further increase the resolution of the map B. This requires measuring the T_1 transition at smaller intervals at every 1/16th Tesla ($\Delta B = 0.0625$ T). Higher resolution maps in B discern increasingly subtle features. This methodology mirrors the process of observing fractals, where zooming into a structure reveals its self-similar behavior.

The color map in Figure 4.12 (Left) is measured with an energy resolution of 0.5 meV and a magnetic field resolution of 0.0625 T, covering the range of B from 4.5 to 9.5 T. Dotted lines on the map highlight two distinct regions: Region I (Middle) and Region II (Right). A closer look in region I involved an increased energy resolution of 0.25 meV and a magnetic field resolution of 0.0625 T. Meanwhile, measurements in region II maintained the original

energy resolution of 0.5 meV but with an increased magnetic field resolution of 0.03125 T.

Upon closer examination of the colormap in Figure 4.12, we identify transitions that have not been previously reported for monolayer graphene, including those perfectly aligned to h-BN [122]. Within each transition, $LL_{-1} \rightarrow LL_0+$, and $LL_{-1} \rightarrow LL_0-$ intricate structures became apparent. In the region of high-energy resonance, $LL_{-1} \rightarrow LL_0+$, we identify at least two distinct peaks spanning between 4.5 and 5.5 T. Furthermore, we observe three distinct peaks between 5.5 and 6.5 T. With increased finer resolution in E as shown in region I of the map 4.12, three high energy peaks becomes well resolved. Subsequently, as we further increased the magnetic field strength, the higher-energy resonance broadens, obscuring any distinguishable features as shown in the region II of the map 4.12.

Inspection of the low-energy resonance ($LL_{-1} \rightarrow LL_{0-}$) shows a rather different behavior. This resonance remains bright and sharp at higher fields. However, unusual broadening of this resonance is observed below $B < 7$ T. This discrepancy in observing detailed structure between the high and low-energy resonances can be attributed to the valley degree of freedom arising from sub-lattice symmetry breaking. As discussed previously, the zeroth Landau Level (LL) is valley-polarized due to sublattice symmetry breaking. Understanding how each of the valley-polarized LLs are reconstructed in the Hofstadter regime poses additional complexity.

The magneto-optical absorption studies of self-similar energy spectra in graphene-h/BN superlattices have received limited attention. While theoretical studies [127] have explored optical absorption in the Hofstadter butterfly within simple square lattices, understanding the optical selection rules in the complex recursive patterns of these systems requires a more detailed theoretical framework. The optical spectrum calculated by Koshino and Moon [128] for twisted bilayer graphene provides a foundation for understanding similar dynamics within the G/h-BN system.

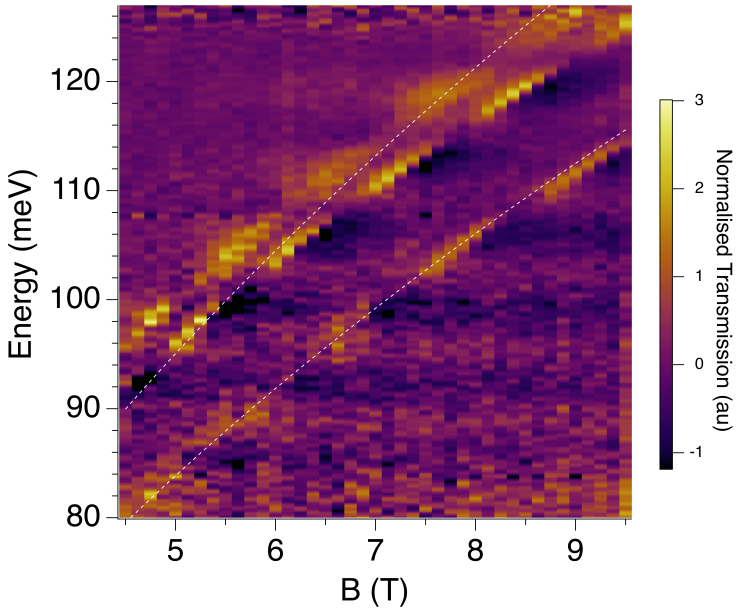

Fig. 4.11: Normalized transmission spectrum with increasing magnetic field displaying two distinct resonances $LL_{-1} \rightarrow LL_{0-}$ and $LL_{-1} \rightarrow LL_{0+}$. Both transitions exhibit a progression proportional to $\sqrt{B}$.

When two sheets of monolayer graphene are rotationally aligned, they create a long-range moiré pattern similar to those observed in G/h-BN heterostructures. This suggests that these systems are equally fertile for studying self-similar energy spectra. In the presence of a magnetic field, Landau Levels (LLs) in twisted bilayer graphene (TBG) undergo significant reconstruction to sub-generation of levels. According to theoretical calculations [128], the optical spectrum also exhibits a hierarchical recursive pattern. This reconstruction allows optical transitions within the same parent level previously forbidden in weak magnetic fields. These transitions occur because daughter levels gain additional angular momentum (n') and can absorb the angular momentum of the photon. The selection rule inside the same valley

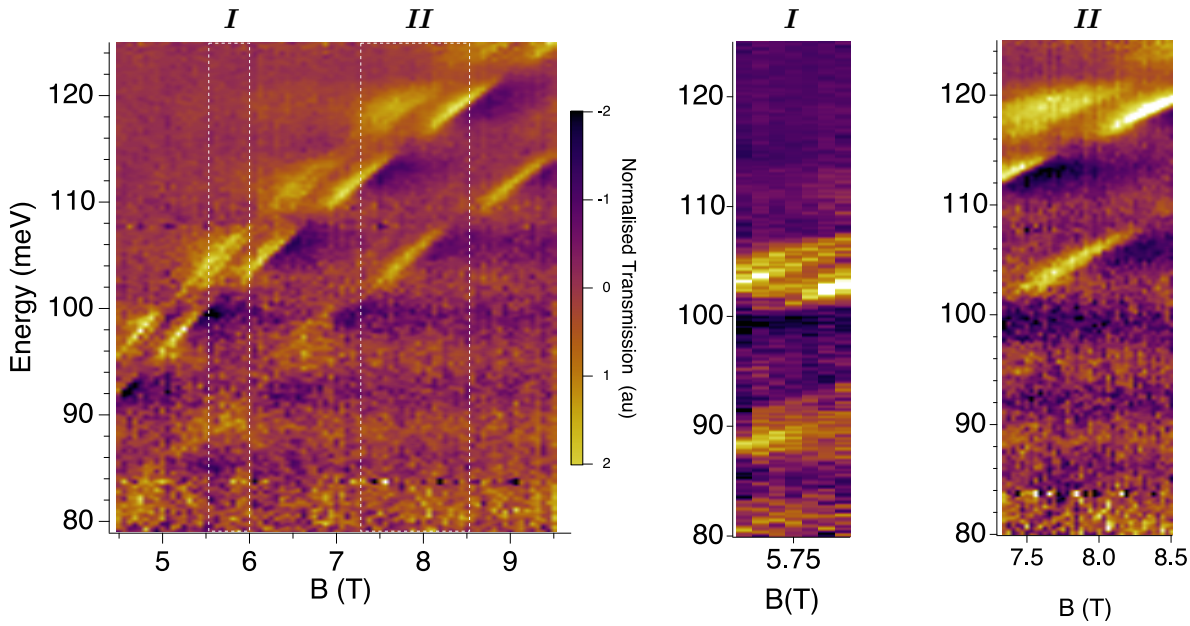

Fig. 4.12: The colormap is generated with an energy resolution of 0.5 meV and a magnetic field resolution of 0.0625 T, covering the range of magnetic field strength B from 4.5 to 9.5 T. Dashed lines mark closer examination into two distinct regions on the spectrum. Subsequent measurements in region I are taken with an energy resolution of 0.25 meV and a magnetic field resolution of 0.0625 T. Measurements in region II are taken with an energy resolution of 0.5 meV and a magnetic field resolution of 0.03125 T.

is found to be

$$|n'| \to |n'| + 1 \quad \Phi/\phi_0 \geqslant 1/q,$$
$$|n'| \to |n'| - 1 \quad \Phi/\phi_0 \leqslant 1/q,$$

indicating that the total angular momentum can be written as the sum over the first and second generations. Moon and Koshino calculate a similar structure at $\Phi/\phi_0 = 1/q$ for every integer q.

In our experimental measurements, we observe a similar phenomenon. Initially, we observe two resonances corresponding to LL transitions from the -1 to 0 level. Yet, with higher

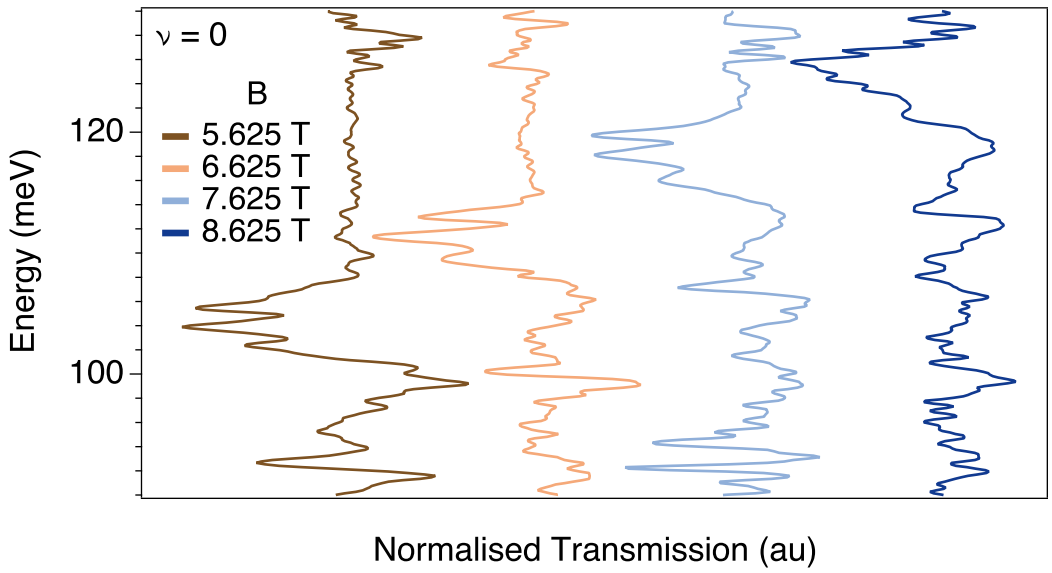

Fig. 4.13: Cyclotron resonance measured as a function of the magnetic field at $\nu = 0$.

resolution measurements, a more intricate picture emerges. We discern the presence of additional, distinct peaks within each of these transitions. Calculations suggest that optical transitions spanning these sub-generation levels become accessible in the regime of the Hofstadter butterfly. We can attribute the observation of the additional peaks likely originating from transitions across second-generation levels, offering further insight into the self-similar behavior of the transitions in the butterfly regime. We lack a comprehensive theoretical model to label the indices of the observed transitions precisely. The idea that LLs reconstruct into sub-generation levels under a magnetic field remains central. An illustrative example of the allowed transitions for one valley is shown in Figure 4.14.

We investigate cyclotron resonance at the $\nu = 0$ filling factor across a range of discrete magnetic field values. The resulting spectra are shown in Figure 5.4. In contrast to the single-degenerate peak observed in high-quality monolayer devices, as detailed in Chapter 3, the $\nu = 0$ spectra for samples with long-wavelength moiré exhibit multiple splitting of this

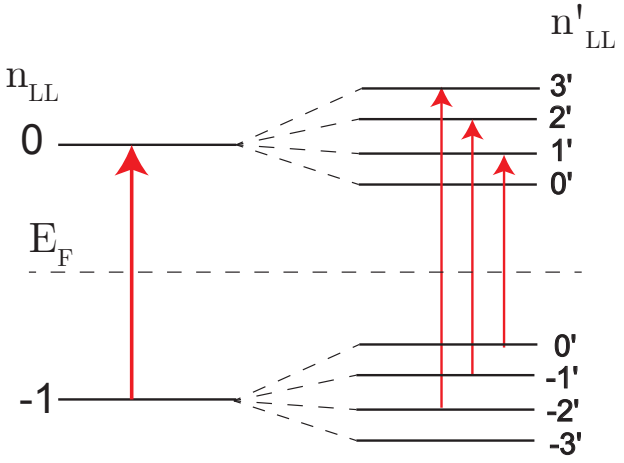

Fig. 4.14: Illustrative example of allowed optical transitions in the fractal regime. In Hofstadter's butterfly regime, the strong reconstruction of Landau levels into sub-generation levels allows for additional transitions across daughter levels within the same parent level.

resonance ($LL_{-1} \rightarrow LL_0$ and $LL_0 \rightarrow LL_1$). Similar to previous analyses, we attribute these additional splittings to transitions across second-generation levels.

4.2.4.2 Asymmteric line shapes and side bands

In addition to resolving distinct features in the CR transitions within the fractal regime, our experiments reveal anomalous line shapes of these transitions. Figure 4.15 presents the normalized transmission near magnetic field values of 5 T, 6 T, and 7 T. We observe dramatic changes in the absorption line shapes and the anomalous peak-dip features that periodically appear in the magnetic field, especially in the B 5/8 T neighborhood, as shown in Figure 4.15. These anomalous features exhibit similarities to those of a Fano resonance.

In optical systems, the underlying physical mechanism of Fano-induced resonance occurs when a discrete localized state becomes coupled to a continuum of states, resulting in characteristic asymmetric line shapes in absorption spectra. Fano resonance initially emerged

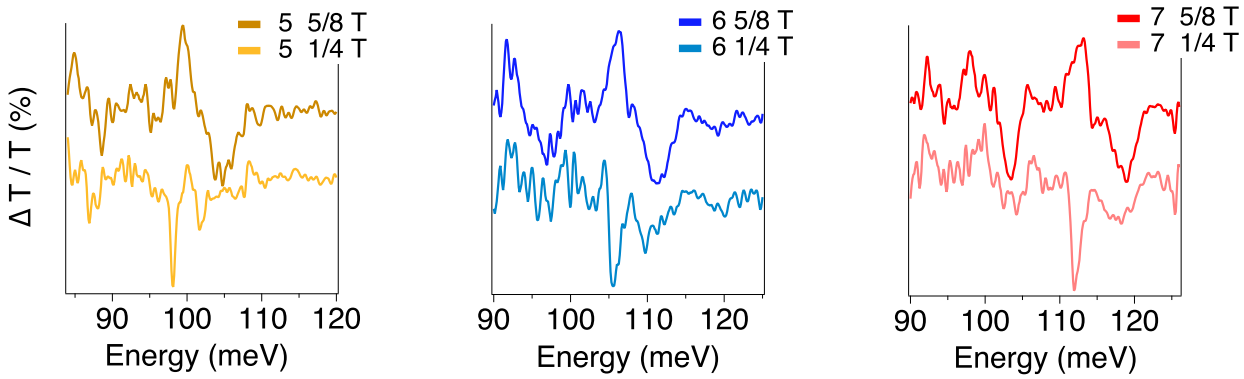

Fig. 4.15: A representative line cut of the color map 4.12 around magnetic fields of 5 T, 6 T, and 7 T reveals characteristic asymmetric line shapes, particularly in the vicinity of B 5/8 T.

in the study of topological insulators [129] such as Bi_2Te_3, where strong asymmetric line shapes were observed in the optical conductivity mode at 50 cm^{-1} due to electron-phonon coupling. In this case, the discrete phonon mode couples to a continuum of intra-valence band transitions, causing a shift in the line shape from Lorentzian to Fano in the presence of a magnetic field.

Similar effects have been observed in bilayer graphene [130] optical absorption studies, where Fano interference between coupled phonons and electron-hole pair excitations is realized and controlled through electrical gating. In this study, Fano resonance describes a collective phonon vibration coupled to a continuum of electron-hole excitations through electron-phonon interactions.

Theoretical investigations suggest that the width of the moiré-modulated Landau Level (LL) increases exponentially [128] in a magnetic field when a continuum of levels is formed within each LL. We hypothesize that if a discrete transition across LL N = -1 to 0 couples to the continuum of reconstructed LLs, we would observe a change in the line shape of the resonance. However, a more detailed analysis is needed to accurately describe the asymmetric

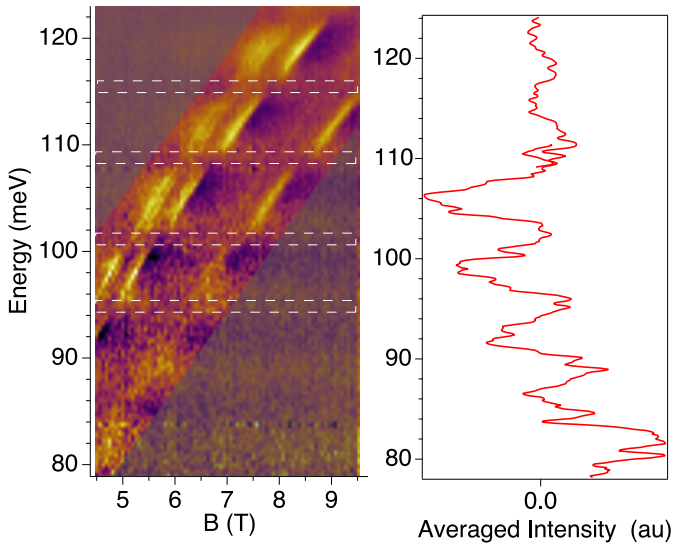

Fig. 4.16: Left panel shows the $\nu = -2$, with a dashed line indicating the dimming of the cyclotron resonance (CR) transitions. In the right panel, the intensities are projected in the direction of the magnetic field. The dark bands in the colormap are observed as oscillations in this projection.

line shapes observed in our measurements using the Fano lineshape.

A particularly noticeable feature, perhaps the first to catch our attention in the colormap, is the periodic dimming of the resonance intensity, as indicated by dashed lines in 4.16, alongside dark side bands occurring at fixed energy intervals. The periodicity of these two features is nearly identical at an energy of around 6 meV.

To better visualize these dark bands against the background, we isolate specific regions of the map highlighted in Figure 4.16 (Left panel) where no resonance is detected and compute the average intensity along the B field direction. The resulting average intensity plot, displayed in the right panel of Figure 4.16, reveals the dark bands that appear as background oscillations are particularly pronounced within the energy range of approximately 80-110 meV, gradually dissipating between 110-120 meV. Notably, these dark bands appear to be strongest in the neighborhood of CR transitions. The periodicity of the background oscilla-

tions is indicative of interference with the CR transitions, which "appear" to lose intensity with the same periodicity. Further analysis is underway to investigate the origin of these anomalies.

4.3 Discussion and Summary

We speculate that the long wavelength background oscillations observed in the spectral measurements likely arise from Fabry-Perot (FP) oscillations. These dark bands appear to vary with gate voltage and are not attributed to the magnetic field effect. The interference of F-P oscillations with cyclotron resonance may intermittently attenuate the resonance, as depicted in the color map (see Figure 4.12). Nonetheless, additional analysis is necessary to elucidate the source of these sidebands in the data comprehensively.

We present cyclotron resonance measurements in the Hofstadter butterfly regime in G/h-BN superlattices. Although magneto-optical absorption studies of self-similar energy spectra in G-h/BN superlattices have received limited attention, understanding the optical transitions in the complex recursive patterns of these systems remains a crucial area for further exploration. Our systematic investigation of first interband cyclotron resonance transitions across varying magnetic field strengths reveals transitions not previously reported in monolayer graphene, likely attributable to the fractal nature of the Landau levels. The magneto-optical measurements could be extended to the spectroscopic investigation of any other graphene-based moiré system, including bi- and tri-layer graphene-hBN and twisted graphene layers [131, 132].

Additionally, we observe a band gap of 12 meV for 0.5° twist angle. This quantitative information should aid in a better understanding of the physics of graphene-based 2D moire superlattice. Particularly, it allows for more accurate modeling of the correlated electron

physics and topological phenomenon in twisted bilayer graphene, ABC trilayer graphene/h-BN, and twisted monolayer-bilayer graphene [133–135].

Chapter 5

Further Investigation and Prospect

5.1 Infrared spectroscopy of phase transitions in the lowest Landau level of bilayer graphene

5.1.1 Overview of the electronic band structure of bilayer graphene

In this section, we briefly review the low-energy band structure of two sheets of graphene. Figure 5.1a shows the bilayer graphene lattice structure, where the bottom layer B_1 atom sits right under the top layer A_2 atom (called the dimer sites). Apart from the nearest neighbor hopping mechanism γ_0 in monolayer graphene, a substantial hopping between A_2 and B_1 atoms is expected as a result of the overlapping of the out-of-plane π orbitals, denoted by the hopping integral γ_1. Weaker hoppings can also occur between orbitals further apart, as indicated in Figure 5.1a (labeled as γ_0). Following the conventional notation in graphite, we denote the corresponding hopping integrals $\gamma_1 = 0.4$ eV, $\gamma_3 = 0.3$ eV, $\gamma_4 = 0.3$ eV [136].

The low energy energy dispersion of bilayer graphene is written as [137]:

$$E^2 = {v_F}^2 p^2 - \frac{\gamma_1}{2} \pm \frac{\gamma_1}{2}\left(\sqrt{1 + 4{v_F}^2 p^2/{\gamma_1}^2}\right), \tag{5.1}$$

where v_F represents the Fermi velocity in bilayer graphene, and $p = \hbar k$ is the momentum with respect to the K point. This equation represents four bands as shown in Figure 5.1b, with a pair of degenerate bands at the charge neutrality point and two split-off bands. Unlike single-layer graphene, the curvature here means the carriers are massive particles. However, the high-energy behavior appears linear, more like single layers. At low energy, near the Dirac points (K), the energy dispersion is simplified to the following hyperbolic form:

$$(2E \pm \gamma_1)^2 - 4{v_F}^2 p^2 = {\gamma_1}^2. \tag{5.2}$$

This is a rather unusual dispersion, evolving smoothly from a parabolic curve at low energies to a linear dispersion at higher energies. Naively, we expect bilayer graphene to exhibit phenomena similar to those of both types of systems.

Since there are four atomic sites in the unit cell and, in principle, they may be held at different energies ε_{A_1}, ε_{A_2}, ε_{B_1}, ε_{B_2}. Three parameters to describe the on-site energy difference between the four atoms are: The energy difference between dimer and non-dimer sites defined by [138]

$$\delta_{dim} = \frac{1}{2}[(\varepsilon_{A_1} + \varepsilon_{A_2}) - (\varepsilon_{B_1} + \varepsilon_{B_2})]. \tag{5.3}$$

Interlayer symmetry U given by

$$U = \frac{1}{2}[(\varepsilon_{A_1} + \varepsilon_{B1}) - (\varepsilon_{A_2} + \varepsilon_{B_2})]. \tag{5.4}$$

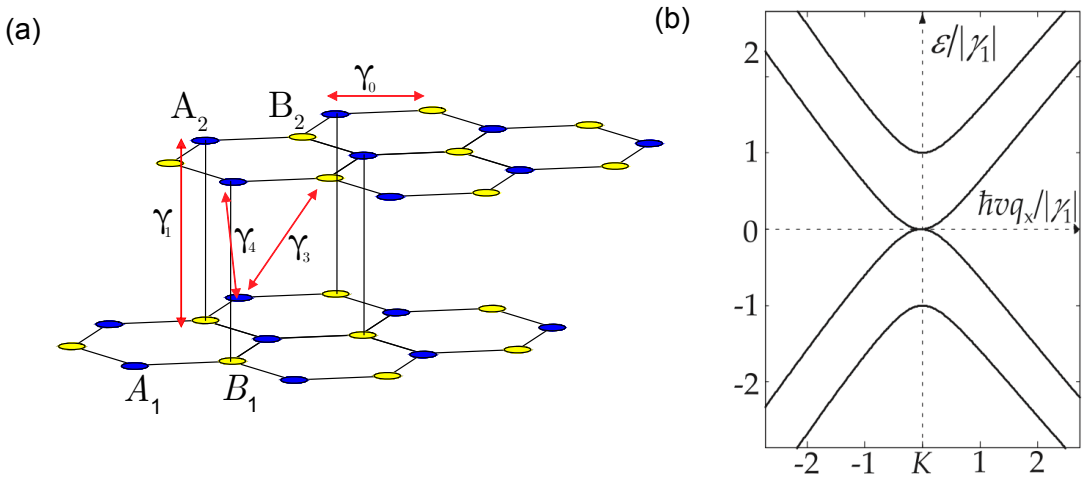

Fig. 5.1: (a) Two sheets of graphene in A-B stacking, γ_i is the hopping integral of the indicated pairs. (b) In the absence of an external magnetic field, the dispersion of neutral bilayer graphene exhibits four bands, with two bands degenerate at the K point and two bands split off by the interlayer hopping energy γ_1. These bands can be concisely described by a single equation of a hyperbolic form.

Energy differences between dimer and non-dimer sites are:

$$\delta = \frac{1}{2}[(\varepsilon_{A_1} + \varepsilon_{B2}) - (\varepsilon_{B1} + \varepsilon_{A_2})]. \tag{5.5}$$

δ_{dim} is intrinsic asymmetry present in bilayer graphene. Interlayer symmetry U can be broken by applying a displacement field using external gates [139]. The presence of a substrate may lead to a difference between on-site energies of adjacent atoms in the bottom layer $\varepsilon_{A_1} + \varepsilon_{B1} \equiv \delta_{dim} + \delta$, leading to both electron-hole asymmetry and an energy gap [140].

5.1.2 Cyclotron resonance in bilayer graphene

In a magnetic field, the lower branches of the bands in bilayer graphene are expected to quantize into LLs with energies given by:

$$E_{n\pm} = \pm\hbar\omega_c\sqrt{|n|(|n|)-1}, \quad \omega_c = \frac{eB}{m^*}, \quad m^* = \frac{\gamma_1}{2{v_F}^2} \approx 0.03m_e \tag{5.6}$$

where m^* is the low-energy bilayer effective mass reflecting the curvature of the hyperbolic band where the conduction and valence meet and is the ratio of the two largest tight-binding parameters γ_1 and v_F. E_{n+} and E_{n-} are assigned to electron and hole states respectively. Similar to monolayer graphene, each nonzero LL is four-fold degenerate due to spin and pseudospin degeneracy, while $n = 0$ LL, the degeneracy doubles because of the orbital degeneracy $n = 0$, or 1 [137].For a given magnetic field B, the index dependence gives rise to an almost equidistant set of LLs.

Due to the combination of spin, valley, and an additional orbital degeneracy, the zero energy LL in BLG is eight-fold degenerate, giving rise to a so-called quantum Hall octet [141]. This massive degeneracy and the couplings of external fields to the involved degrees of freedom make the quantum Hall octet in BLG a fertile environment to explore the effects of symmetry breaking in the quantum Hall regime. Furthermore, Kohn's theorem [30], which prevents the observation of many-body interactions in translationally invariant 2DEGs with parabolic dispersions and fails in monolayer graphene [27, 28, 34, 38, 39], also fails in bilayer graphene due to the chiral nature of its charge carriers [142]. As a result, many-body interactions are expected to impact the cyclotron resonance in BLG but the experimental literature is sparse [143–145]. The phase diagram of bilayer graphene is best studied in dual-gated devices that allow independent control of the charge density and electric displacement field. Measurements based on scanning probes are ill-suited for this purpose, making optical

approaches especially relevant as they can probe through infrared-transparent gates.

Recent scanning tunneling experiments in monolayer graphene sheet found a bond-ordered ground state at LL filling factor $\nu = hn/eB = 0$ (n the zero-field carrier density, $-e$ the electron charge, and B the magnetic field), at odds with the canted antiferromagnet (CAFM) state previously inferred from high field transport [146, 147]. Although the CAFM in *bilayer* graphene is well-established, probing excitations in the bulk of the bilayer sheet directly may nonetheless be illuminating. We address this with a study of the far-infrared CR in a boron nitride-encapsulated, dual-gated graphene bilayer, focusing on excited state transitions to or from the quasi-zero energy Landau level octet. Our findings, consistent with the presence of a CAFM, reveal an intriguing complexity in the excited state transitions at $\nu = 0$, and a surprisingly sharp phase transition from the CAFM to the fully layer (valley) polarized regime.

Specifically, we measure CR transitions between the octet LLs ($N = 0, 1$) and $N = \pm 2$, for both $\nu = 0$ and $+4$, at a fixed magnetic field $B = 13$ T (chosen to match a window of maximum far-ir transmission) while tuning the layer symmetry breaking displacement field, D. At $\nu = 4$ we observe the valley splitting within the $N = 1$ LL, which closely tracks the electrostatically tunable band gap at $B = 0$. At $\nu = 0$ we see an interaction-driven gapped state at $D = 0$, signatures of a spin-ordered ground state at low D, and a sudden sharp transition to the layer-polarized ground state at intermediate D. Finally, in holding $D = 0$ fixed while tuning the filling factor over the range $\nu = \pm 6$, the CR line shapes show a weak electron-hole asymmetry with multiple line splittings and a pronounced increase in the transition energies right at $\nu = 0$.

To better understand these findings, this work undertook an in-depth theoretical calculation of the inter-LL energies corresponding to these CR transitions [M. Schossler et al.]. We progressively increased the order of approximation until the theory attained a very close

match to the $\nu = 4$ data and a reasonable, if not perfect, match to data at partial LL fillings. The single-particle physics is first calculated non-perturbatively for the four-band Slonczewski-Weiss-McClure (SWMc) tight-binding model in a B field, accounting for both the energy difference Δ' between dimer and non-dimer sites, and the skew interlayer couplings γ_3 and γ_4 [148, 149]. While the non-interacting spectrum qualitatively reproduced the phenomenology of the CR transitions at integer filling ($\nu = 4$), it fails to describe the results at partial filling of the octet. This is expected as transition from the symmetry-broken states significantly influences the CR spectrum.

The effect of interactions was studied using a self-consistent Hartree-Fock mean field approximation including all four bands of the SWMc tight-binding model of bilayer graphene. Unlike previous studies [150–153], we numerically project on to the $N = 0, 1$ octet and ± 2 levels, and then incorporate interactions comprising both the long-range layer (valley) independent Coulomb, and layer-dependent short-ranged interactions, which break the SU(4) symmetry of the octet. The inclusion of layer and valley anisotropy is essential to capture the broken symmetry phases at partial filling of the octet at $\nu = 0$ [154]. In our calculations, we also include the influence of the infinitely deep sea of filled states on the zeroth LL [153, 155], the Zeeman interaction, and the externally applied D field. The energy bands are calculated self-consistently with a screening factor, and, at $\nu = 0$, the short-ranged interaction couplings are taken as adjustable parameters. As described below, a coherent picture consistent with the experimental data emerges when the full model described above is employed. Details of the theoretical calculations is presented in [156], while here we focus on experimental phenomenology.

5.1.3 Experiment

Far-ir transmission data were measured in a dual-gated, boron-nitride encapsulated bilayer graphene device with a global Si back gate and a 550 μm^2, 20-nm-thick semi-transparent Cr top gate, all at a fixed magnetic field $B = 13$ T and sample temperature $T \approx 1$ K. Transmission spectra with a resolution of 1 meV were acquired at given ν and D values, averaged for 4-8 hours, and normalized by spectra at different top gate voltages as previously discussed section 2.3.

5.1.4 Cyclotron resonance transitions at $\nu = 4$

We first orient this study on infrared transitions at fixed $\nu = +4$ where interaction effects are expected to be minimal. Figure 5.2a shows a color map of spectra for the $N = +1 \rightarrow +2$ LL transition at displacement fields D/ϵ_0 from -80 to 330 mV/nm; due to the long averaging times required for good signal to noise, spectra were not collected for all D values. Example spectra for $D = 0$ and 150 mV/nm, and 320 mV/nm are shown in Figure 5.2b. The individual resonances are quite narrow, with line widths of 1-3 meV for individual resonances.

With reference to Figure 5.2c, at $\nu = +4$ the Fermi level lies between the $N = 0, 1$ octet and $N = +2$, so valley-conserving cyclotron transitions $|N, \lambda\rangle = |1, +\rangle \rightarrow |2, +\rangle$ and $|1, -\rangle \rightarrow |2, -\rangle$ are allowed where $\lambda = \pm$ denotes the K^λ valley. The applied displacement field breaks the valley degeneracy of the $N = 0, 1$ LLs (and $|N| \geq 2$ as well, to a much smaller degree [149]) and generates an interlayer potential difference, $U = \alpha e D d/\epsilon_0$, with $d = 0.34$ Å the distance between layers, and α a phenomenological screening parameter. At the same time, transitions into the filled $N = 1$ level are blocked. Overall, one expects a single valley-degenerate resonance at $D = 0$ that splits in two for $|D| > 0$, with the splitting being a direct measure of the induced valley gap in the $N = 1$ level. The data in Fig. **??**(a)

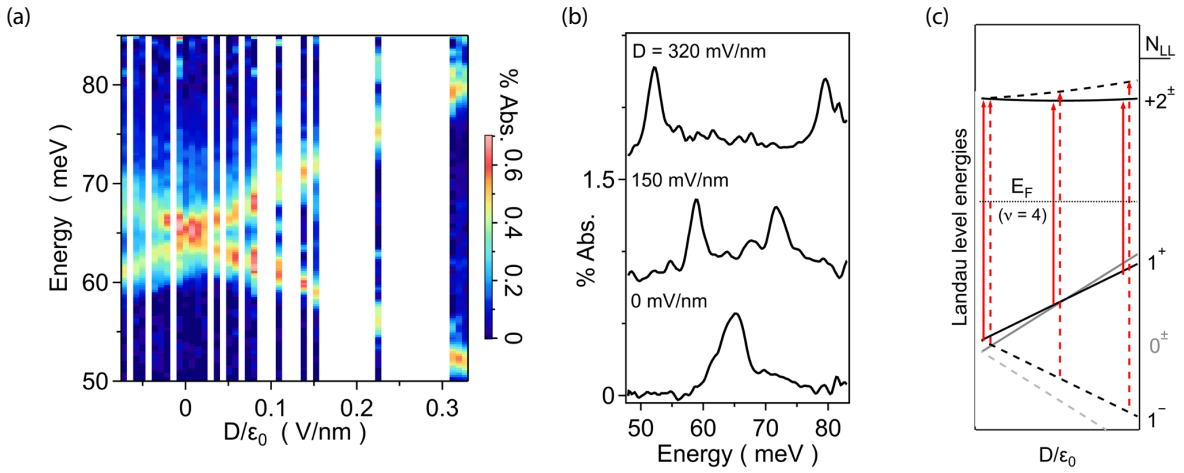

Fig. 5.2: (a) Color map of resonances at $\nu = 4$ vs displacement field, D.(b) Example spectra (black) for $D = 0$ and 150 mV/nm, 320 mV/nm (c) Landau level energies as a function of D; red arrows show allowed transitions between $N_{LL} = 1$ and 2, where superscripts mark the $K^{\pm}$ valleys.

show a nearly linear-in-D gap opening, similar to the zero field case [157–159].

We wish to know what level of theoretical approximation is required to accurately predict the D-dependence of the allowed transition energies shown in Fig 1c. At $\nu = +4$ this model has only a single adjustable parameter, α, which determines the dimensionless screening strength. Interaction anisotropy has little impact far from charge neutrality and are disregarded for now. We adopt literature values for the SWMc terms [149], and α is uniquely determined by its dual role in the model of both reducing the strength of Coulomb interactions and converting the applied electrical potential into a D-field. Therefore, it controls both the transition energies and the rate at which these energies change with the applied D. In Figure 5.3, we present the peak transition energies obtained from the Lorentzian curve fits applied to the data from 5.2a, alongside the theoretically predicted transitions. We observe excellent agreement between the experimental data and the theoretical model described above, particularly with $\alpha = 0.244$, as shown in Figure Figure 5.3b. To further understand

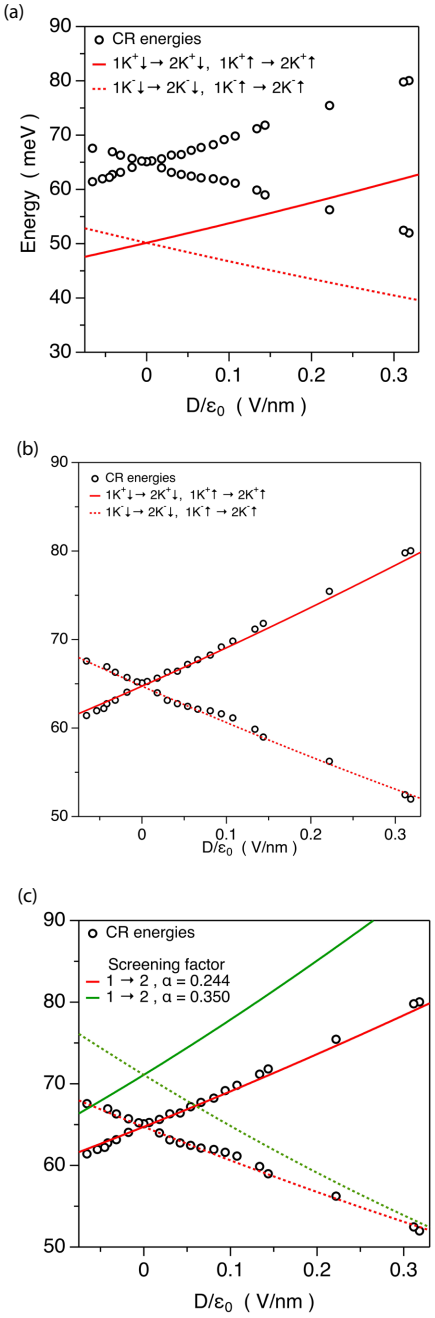

Fig. 5.3: Peak energies from fits to data in Figure 5.2a (depicted by open circles) are compared with theoretically predicted transition energies [156] for (a) the single-particle model, (b) many-body correction with a screening parameter of $\alpha = 0.244$, and (c) $\alpha = 0.350$.

the level of theoretical approximation required to accurately predict the D-dependence of the allowed transition energies shown in Figure 5.3c, we explore the effect of slight adjustments in the value of α. Interestingly, even a slight deviation, such as $\alpha = 0.350$, which gives both a stronger D-dependence and shifts the energies up across the whole range of D and leads to leads to noticeable discrepancies with the experimental data. Beyond the screening term, this good fit is only achieved by including both many-body corrections to the single particle Landau level energies and the more realistic SWMc model for bilayer graphene. Figure 5.3 compares the experimentally obtained transitions with those predicted by the single-particle model.

5.1.5 Cyclotron resonance transitions at $\nu = 0$

A color map of spectra measured at $\nu = 0$ reveals further interesting and unexpected phenomena in Fig. 5.4. Line cuts like those shown in Fig. 5.4(c) reveal the fine structure due to multiple resonances, the energies of which are plotted in Fig. 5.4(b). Beginning precisely at $D = 0$, two peaks of approximately equal weight can be resolved with a small splitting of 2.3 meV. These peaks increase in energy with differing slopes for increasing D, and a third lower-energy peak emerges above $D/\epsilon_0 = 26$ mV/nm. The weight of the middle peak is now roughly double the other two. With increasing D these peaks disperse independently—the highest peak blue-shifts by a few meV while the lower two redshift with differing slopes—until, right at 120 mV/nm, all three peaks suddenly vanish to be replaced by a single broad peak with a long low-energy tail visible in Fig. 5.4(a). Immediately above this critical D field, just two peaks reappear and follow a linear-in-D dependence reminiscent of $\nu = +4$, except in lieu of a V-shaped splitting, both peaks increase in energy with a close approach or possible crossing near 350 mV/nm.

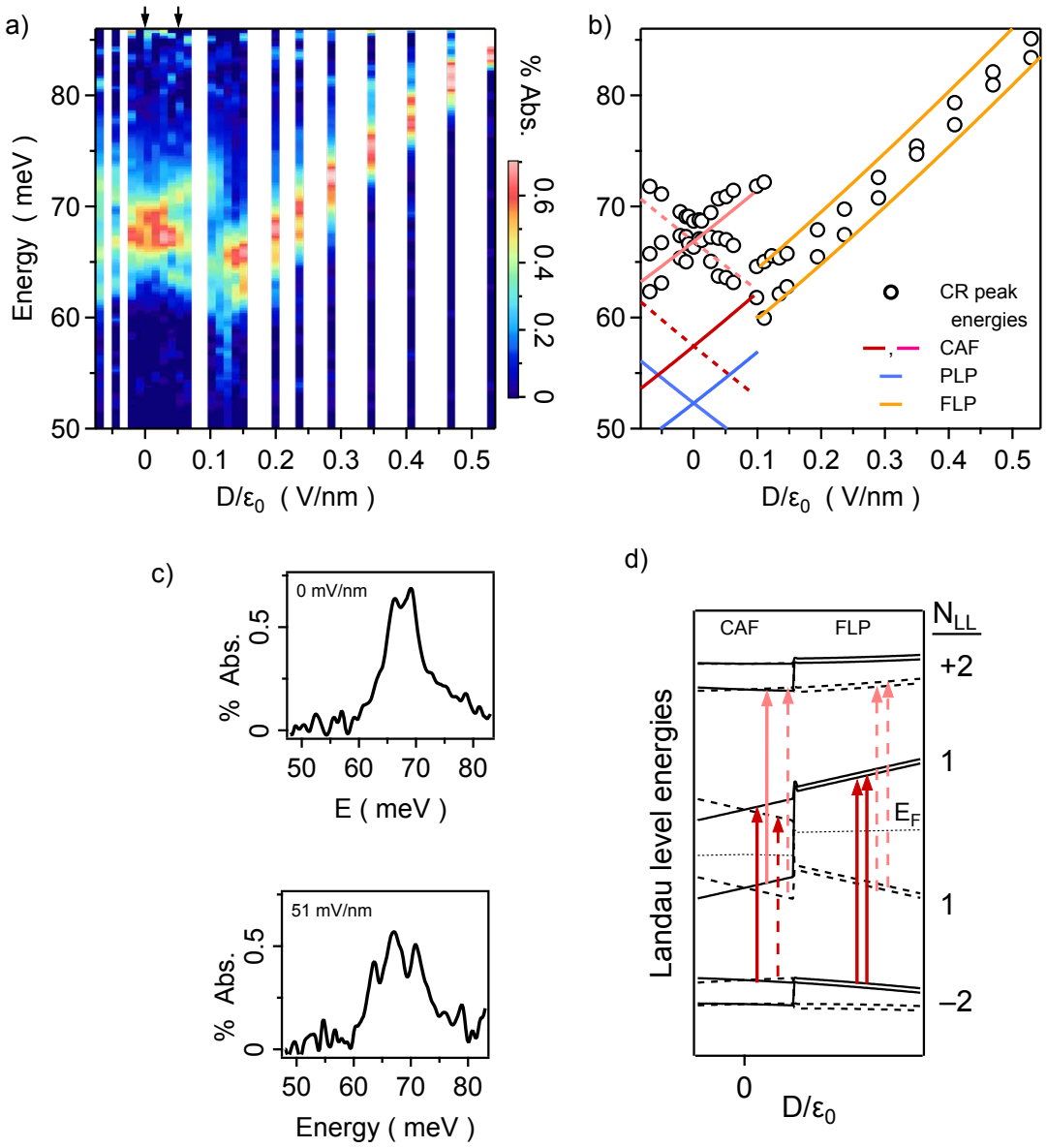

Fig. 5.4: (a) Color map of spectra at $\nu = 0$ vs displacement field, D. (b) Resonance energies vs. D. Colorful lines are results of theoretical calculations for the canted antiferromagnet, partially layer polarized, and fully layer polarized ground states. (c) Example spectra showing the detailed line shapes for $D = 0$ and 51 mV/nm, at the positions of black arrows in (a). (d) Calculated Landau level dispersion vs D, with dipole-allowed transitions $N = -2 \rightarrow +1$ $(+1 \rightarrow +2)$ in red (pink). Transitions are shown separately for both the CAFM and FLP regimes. The $N = 0$ LLs are suppressed as they are not involved in these infrared transitions.

As above, we seek to accurately calculate the energies of the allowed transitions shown in Fig. 5.4(d). Just like $\nu = +4$, at high D the bilayer enters the fully layer polarized (FLP) regime where all charge is dragged to one side of the sample. The FLP prediction shown in Fig. 5.4(b) is a straightforward extension of the calculations above to the case of $\nu = 0$, employing the same values of α and the SWMc parameters, and the results closely track the observed transitions.

For weak displacement fields, however, there are four possible correlated ground state phases expected at $\nu = 0$ in the model we employ, depending on the values of phenomenological short-ranged layer isospin anisotropy terms u_z and $u_\perp$ [154]: a fully magnetized ferromagnet (FM); the FLP, and also a partially layer-polarized (PLP) state; and the canted antiferromagnet. Prior experimental work suggests the CAFM is the ground state for bilayer graphene [160, 161]. The FM is excluded since its quantized edge channels should lead to a finite spin Hall resistance rather than the gap seen in transport, and the FLP regime at high D clearly does not extend below the sharp transition at $D/\epsilon_0 = 120$ mV/nm. Thus we calculate the energies of the allowed LL transitions $|-2, \pm\rangle \rightarrow |1, \pm\rangle$ and $|1, \pm\rangle \rightarrow |2, \pm\rangle$ for $D/\epsilon_0 < 120$ mV/nm, initiating the calculation by choosing values for the anisotropy terms which stabilize either the CAFM or PLP phases. The results are plotted over the data in Fig. 5.4(b).

We find both the CAFM and PLP ground states lead to pairs of diverging linear-in-D transitions arising as the valley symmetry is broken. Since the spin-degenerate PLP has only a single pair of transitions vs two for the CAFM, we rule out the PLP phase because three transitions are plainly visible. As noted, the middle peak has roughly double the spectral weight of the others, implying it contains two nearly (perhaps accidentally) degenerate transitions for a total of four, consistent with the CAFM. There is only partial agreement between the data and the predicted dispersions. While the upper and lower

resonances disperse close to the expected slope vs D, the middle peak shows only a weak and non-monotonic dependence on D. These data do not rule out the CAFM, but neither are they in robust agreement with the predicted behavior: in particular, all the resonances overlap with the energy range of the upper set of CAFM transitions (pink in Fig. 5.4(b)), but not the lower (red).

5.1.6 Discussion

Collective mode excitations (magnetoexcitons) [151, 153, 155, 162, 163], as well as short-range Ising-type interactions caused by fluctuations in the density between two LL orbitals [150, 152], are not accounted for in the present model. These may add to the total excitation energies, enable alternate ground states, and perhaps account for discrepancies between these theoretical calculations and the data.

Alternatively, recent treatments show a larger phase space for correlated ground states exists, particularly at the high B field relevant to this work, and includes Kekule, broken U(1) or U(1)×U(1) symmetries, a host of fully- or partially-polarized states, and various coherent phases [152, 164–166]. If present, these may impact the otherwise first-order CAFM-to-FLP transition, introducing additional intermediate phase transitions that could be first or second-order and which broaden the range of D over which the ultimate CAFM-to-FLP changeover occurs. Though the present data are as yet insufficient to make any strong claim, Fig. 5.4 contains two clear departures from the pure CAFM model: the weak dispersion of the middle two resonances, and a range from approximately 100 to 120 mV/nm where the upper and lower resonances fall to lower energies than expected from their trajectories at small D. This suggests that other interstitial phases may be present between the CAFM and FLP as suggested by prior works [167–169].

On the whole, infrared magnetospectroscopy reveals a host of intriguing behavior arising from electron correlations, and we find the trends and absolute energies of the constituent Landau level transitions can be quite well captured in a sufficiently detailed theoretical model. The close but not perfect agreement leaves room to undertake more sophisticated calculations and suggests infrared spectroscopy in future higher-quality devices will be fruitful in revealing details of the competing correlated ground states in bilayer graphene, as well as in twisted and/or multilayer graphene devices [170, 171].

5.2 Future work

Our vision is to use this system to probe deeply aspects of the physics of interacting electrons that other techniques are not sensitive to.

Quantum sensing is a major topical theme that relies on disturbing a coherent system to achieve higher sensitivity than incoherent devices. Separately, the far-IR/THz regime has always been a difficult problem for sensors since all materials have vibrational and electronic activity there. These themes can be reunited to explore the basis for building a CR-based graphene qubit. The idea is to create a two-level system using the strongly anharmonic spacing of graphene LLs, place the graphene device in a cavity to significantly enhance the light-matter interaction, and explore the ultrastrong coupling regime. Recently, the strongest light-matter coupling outside of superconducting qubits has been achieved using electron CR in a cavity [172], where quasiparticles called Landau polaritons are formed by the strong coupling of light and LL transition. Graphene LLs will also form Landau polaritons [173], but since the LL energies depend on the square root of the LL energies, each $N \rightarrow N+1$ transition is energetically coupled, and so is a proper two-level system. This is a key difference from work to date, which is based on GaAs with evenly spaced LLs,

where excitations can be propelled continuously up the LL ladder. Thus, in principle, the graphene approach can realize a novel qubit that is addressable in the infrared/THz and native to high magnetic fields.

When electron-electron scattering dominates over electron-phonon and impurity scattering, a fluid-like flow of charge carriers results, where this dynamic flow is governed by classical fluid mechanics. In a narrow window of temperature and carrier density, the hydrodynamic limit can be achieved in monolayer graphene. High-quality graphene provides an attractive platform for exploring Dirac-fluid physics, in which relativistic electrons and holes form a strongly interacting plasma. This e-h plasma persists at high temperatures in the quantized regime and resides entirely in the zeroth LL. Recently [174] observed giant linear magnetoresistance in monolayer graphene in the quantized regime, where this linear behavior is qualitatively explained by diffusion of cyclotron orbits on the zeroth landau level through e-h puddles. We can explore the absorption spectrum of Landau quantized graphene in the hydrodynamic limit through magneto-infrared spectroscopy.

Recent work suggests that the hydrodynamic regime is more readily achievable in bilayer graphene as it exhibits no temperature cutoff and provides a wider carrier density window, suggesting that it is better suited for achieving this hydrodynamic limit than monolayer graphene. In the presence of a magnetic field, a hydrodynamic cyclotron resonance arises that departs from the kinematic cyclotron frequency [175]. There is a finite parameter space in temperature and magnetic field in which this departure can be observed, making it possible to explore cyclotron resonance in bilayer graphene using magneto-optical infrared spectroscopy within and outside the hydrodynamic window.

APPENDICES

Appendix A

Setting up LD400 Bluefors for infrared measurement

A.1 Preparing for a cooldown

1. Set up the experiment and sanity checks.

    - Before proceeding with the cooldown, it is crucial to cross-check the wiring of both the sample stage and detector circuit to preempt any potential issues that may arise during the operation. Start by conducting a continuity check between the wiring at the sample stage and the breakout box. The measurement rack accommodates two sets of breakout boxes: one labeled Ph-Bz (Phosphorous Bronze), connected to the IR sample stage, and the other labeled Cu-Su (Copper superconducting), connected to the detector circuit. Using a multimeter, measure the resistance between the breakout box pins and the fuzz buttons (shown in A.2) on the IR stage. Pins 1, 6, 12, and 13 should connect to the co-axial cables, while pins 2, 3, 4, 5, 7, 8, 9, 10, 11, 14, 15, 16, 17, and 18 should connect to the sample puck, and measure an approximate resistance of ≈ 10 kΩ due to the presence of

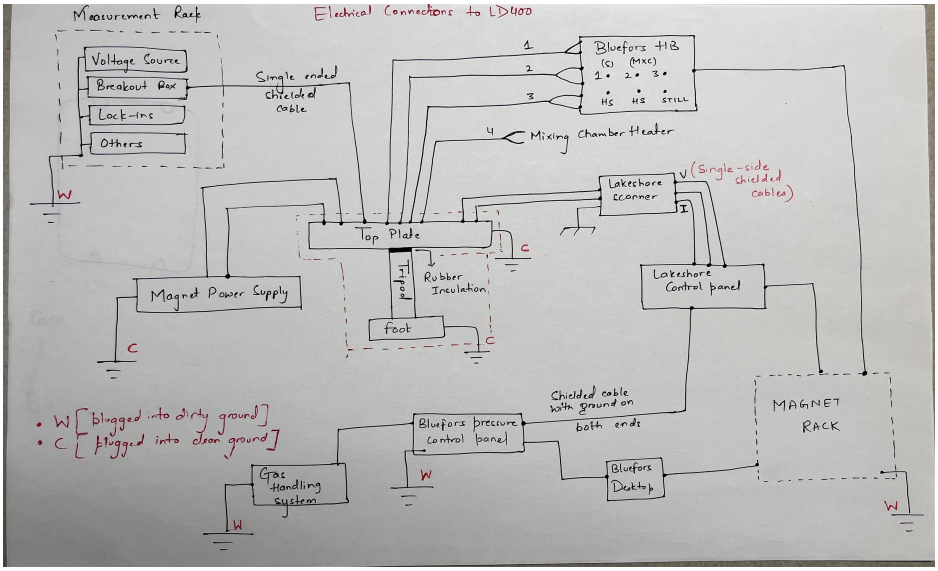

Fig. A.1: Ground configuration of the dilution fridge.

two sets of RC filters, each with a 10 kΩ resistance on the line and ≈ 470 pF to fridge ground. Subsequently, proceed with the isolation test: apply 10V using the Keithley source meter and measure the leakage current for each breakout box channel, aiming for a measurement of < 0.02 A to ensure minimal leakage. The pin configuration of the IR sample puck is shown in A.2.

- Next, to verify the wiring to the detector, measure the resistance of the bolometer and load resistor (20 MΩ) at room temperature. Set the multimeter to a manual setting (value greater than 60 MΩ), bias co-axial line "C" to the fridge ground should measure a resistance of ≈ 20.41 MΩ. Keep a record of this value before proceeding with the cooldown and check with previously recorded values. Additionally, measure the resistance of the bolometer heater and thermometer at the Cu/Su breakout box: pins 14 and 15 should read ≈ 27 Ω, and pins 10, 11, 12, and 13 should show ≈ 1 kΩ. Finally, for pins 3 and 4, connected to the silicon diode-based thermometer on the JFET circuit board, a bias current of 10 μA should

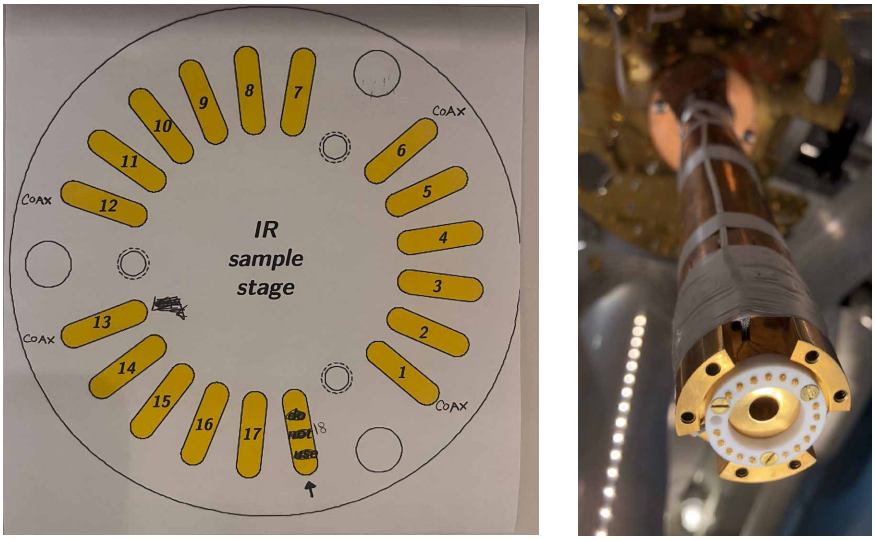

Fig. A.2: (Left) Pin configuration for the IR sample holder. (Right) The top sample stage paraboloid suspended from the mixing chamber plate, with integrated wiring and fuzz button contacts shown.

measure a forward drop of ≈ 0.556 V across the diode at room temperature. The details of the electrical wiring to the bolometer circuit are shown in Figure A.3.

2. Entry in the fridge logbook.

   Check the most recent entry in the fridge logbook to familiarize yourself with the latest fridge status. Begin a new entry in the logbook by recording the date and the name of the person operating the dilution fridge. It is crucial to carefully document the experimental arrangement and specific details pertinent to the current run. For instance, if the ongoing run involves a magnet, provide comprehensive details about the device and the configuration of the infrared setup. Such detailed documentation is invaluable for reference, as different configurations can result in varying fridge temperatures and pressures during each run.

3. Closing up the dilution fridge.

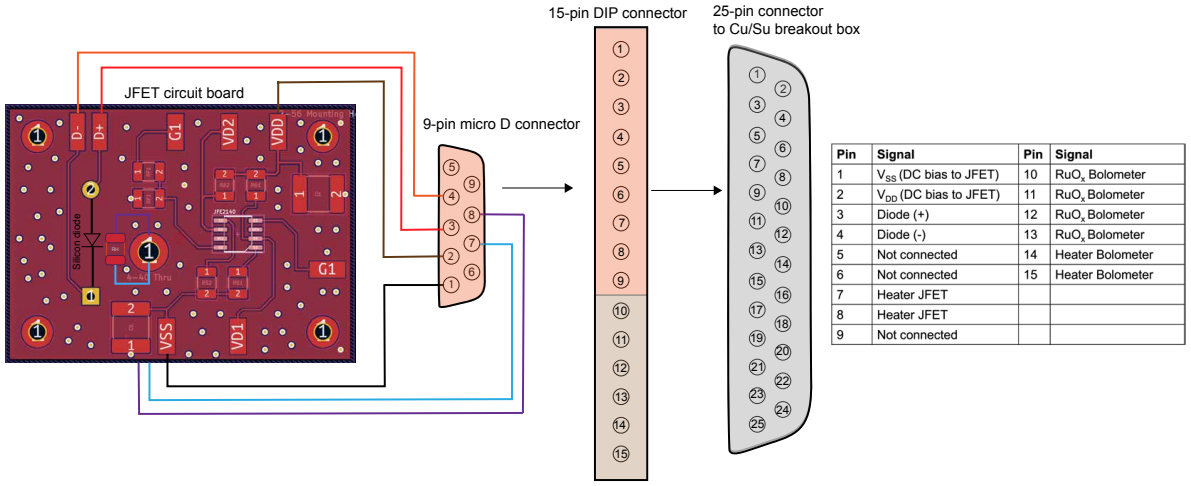

Pin	Signal	Pin	Signal
1	V_{SS} (DC bias to JFET)	10	RuO_x Bolometer
2	V_{DD} (DC bias to JFET)	11	RuO_x Bolometer
3	Diode (+)	12	RuO_x Bolometer
4	Diode (-)	13	RuO_x Bolometer
5	Not connected	14	Heater Bolometer
6	Not connected	15	Heater Bolometer
7	Heater JFET		
8	Heater JFET		
9	Not connected		

Fig. A.3: Color-coded 25 AWG solid wires establish connections to the JFET enclosure via a 9-pin micro D Female connector. Inside the JFET enclosure, 0.003" steel wires run from the Male D connector (mounted on the enclosure) to the JFET circuit board. Additionally, 0.005" copper wires are used for the heater connections. The connections to the thermometer on the bolometer housing utilize quad-twist Ph-Bz wires, while Cu wires connect to the bolometer heater.

- Before closing up the DR, check if the openings to the various cold plates of the dilution fridge are clear. We often cover the mixing chamber plate to prevent dust from falling on the device. In that case, remove the covering and any other unwanted tools from the cold plates of the DR. Install the radiation shields (cans). For all cans, the welded seam should face the east wall of Crow 01. Start with installing the copper radiation shield. Handle the shields minimally; use gloves while handling the copper cans. If the top 50 K shields and cans are already in place, install the middle 4K aluminum can. The aluminum cans should be about as tight as possible with the allen ball driver. Before mounting, each can should be wiped down with isopropanol on the metal sealing surfaces. Screw the heat pipes on the bottom face of the 4K shield. It is time to install the magnet; extra care must be taken while handling it. Ensure the persistent switch wires are not

touching each other, and carefully secure them with aluminum tape. Install the 50 K middle shield followed by the 50 K bottom shield. The nested input cone assembly is attached to the 50 K bottom shield. Therefore, it is essential to handle it carefully without scratching the cones into the wall of the magnet bore. Ensure the 1 mm aperture between the input cone is clear of dust. Wash each o-ring and groove with isopropanol before mounting the outer vacuum cans. Make sure the solvent dries completely before mounting. Install the middle vacuum can, followed by the bottom vacuum can. The bottom can is attached to the gate valve and needs to be carefully aligned with the input cones. Do not over-tighten the wingnuts on the vacuum cans, and do not tighten them during the operation. At this point, check if the gate valve is functional by opening it to the dilution refrigerator

4. If the DR unit will be used, pump out the internal and cold traps.

   - First, ensure that the mixture has been collected safely into the mixture tank and that the manual valve on the tank is closed. Typically, the pressure on the mix tank reads -0.35 Bar when all the mix is properly stored. Note that $V8$, $V9$, and $V10$ must remain closed for this entire procedure.

   - **Pump the internal trap**: Start by switching on *Scroll 2*, and wait approximately 10 s until the internal relay of the pump switches on. Open V21 and confirm the operation of the pump by monitoring gauge P6. When the pressure P6 is < 1 mbar, close V21, open V23, and switch on *Turbo 2*. Once *Turbo 2* is up to speed (1010 Hz), open $V22$. Pump until P6 $< 5 \times 10^{-4}$ mbar, then close V22. The pressure P6 can be used as a reference to monitor how much gas is trapped in the internal trap.

- Open V17. If P6 rises, pump the space up to V17 using either the *Scroll* pump or both the *Scroll* and *Turbo* pump. If *Turbo* was used, close V22.
- With V17 open, open V3 and V4. If P6 rises, record this value in the logbook. If it is much larger than the previous value in the logbook, make a note and take the necessary actions. Pay attention to whether the pressure is more or less than 1 mbar, and use the appropriate *Scroll* pump or *Turbo* pump to reduce P6 to less than 5×10^{-4} mbar. Close V3 and V4.

- **Pump the cold liquid nitrogen (LN_2) trap**: The contamination can be pumped from the LN_2 trap with *Scroll 2* via the service manifold (open V21, V17, and V7). The trap can now removed from the LN2 dewar.
  - When the external LN_2 cold trap is in use, the active carbon inside should be regenerated regularly. Typically, this should be done at the end of a run when the DR system is warmed up to room temperature. While the cold trap is being pumped, its body should be heated with a heat gun for approximately 5-10 minutes to approximately 100 degrees Celsius to regenerate the charcoal inside. Afterward, all valves should be closed, and the trap should be appropriately stored.

5. Evacuating the vacuum cans (VC).

- Before pumping on the vacuum cans (VC), ensure that the manual valve installed between the vacuum cans and pressure sensor P1 is closed to control the venting and evacuation of the cans. Turn on *Scroll 2*, and open V21, V16, and V14 after a few seconds. Pressure gauge P6 should drop precipitously. To evacuate the cans, slowly begin to open the manual valve; P6 will increase, but keep the pressure

P6 below 100 mbar. Monitor P6 during this procedure and continue to open the manual valve further. Repeat this procedure until P6 stops increasing any further; at this point, it is safe to open the manual valve fully. Once P6 is below 1 mbar, close V21 and V16. Open V23 and switch on *Turbo 2*. Once the *Turbo* is up to speed, open V16. If P6 is below 1 mbar, open V22 to pump on the cans with *Turbo*.

6. Leak check the DR.

   - While evacuating the vacuum cans (VC) manually, it is recommended to connect a leak checker to the TEST port at the gas handling system to check for potential leaks. Turn the leak checker on and let it auto-calibrate. Connect the K-25 bellow hose to the test valve port, ensuring that the test valve is closed. Pump the line until the leak detector displays "measure" and all the caution tabs are green. The inlet pressure of the leak checker should read less than 10^{-2} mbar pressure after pumping the test line. The VC can then be leak-checked parallel to the pumping line. Once all the lines are evacuated and the VC is pumped with *Turbo 2*, open the test valve. The leak rate before turning the test valve should read approximately 1.8×10^{-9} mbarl/s.
   - The gas escaping through a possible leak can be detected by the leak checker. Perform the Helium sniffing test by spraying Helium at possible locations where a leak may occur. Start with the top of the fridge, then between the top o-ring of the topmost vacuum can. Repeat this for the middle o-ring and finally the bottom o-ring and close to the gate valve. If a leak is detected, the alarm on the leak detector will turn on, typically when the leak rate exceeds 1×10^{-7} mbarl/s.

7. Start the pulse tube cooler.

- When the pressure P6 in the VC has reached below 2×10^{-2} mbar, the pulse tube can be started. Ensure that the cooling water of the pulse tube is running at 3.5 Gallons per minute; otherwise, the temperature protection circuit of the pulse tube will trip. In this scenario, the pulse tube will cease operation even though the LED on the front panel stays on. In the log book, record the time that the pulse tube is turned on. Start data acquisition to record the fridge temperature and pressures, along with any sample parameters that need to be recorded during the cooldown. Plug in and turn on the Bluefors heater box. From the LD400 control panel, turn on the Still and Mixing Plate heat switches (*HS-STILL* and *HS-MC*). With the magnet and infrared setup, it typically takes approximately 48 hours for the 4K plate thermometer (T2) and magnet thermometer (T3) to fall below 4 K. A typical cooldown curve in the infrared configuration is shown in Figure A.4.

8. Condensing the mixture.

    - To start condensation, the mixture from the tank must be added into circulation, and the manual valve on the tank should be opened. Record the mixture tank pressure both before and after opening it in the logbook. Check pressure P5 and record its value in the logbook, ensuring it matches the previous values. Fill the LN_2 dewar completely (approximately 15 liters). Wait for an hour after the trap is reinserted back into the cold trap. Load and run the script "Condense with LN2". The dilution refrigerator will then begin condensing the mixture in the unit. This process typically takes around 2 hours before the temperature stabilizes.

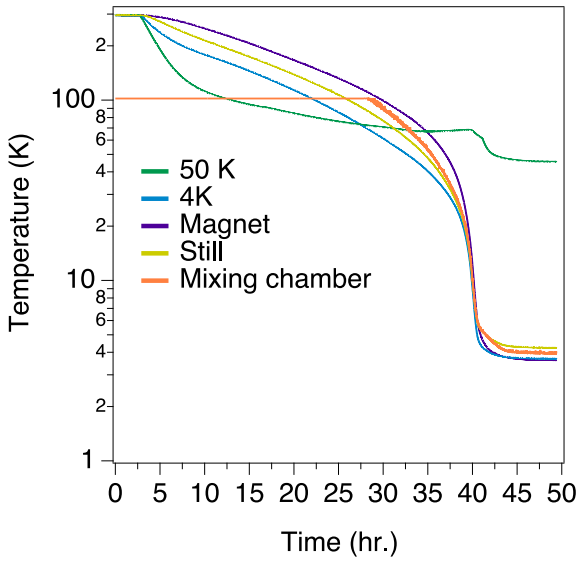

Channel	Temperature (K)
T1 (50 K)	46.68
T2 (4 K)	3.718
T3 (Magnet)	3.68
T4 (STILL)	4.23
T5 (Mixing chamber)	3.92

Pressure sensor	Pressure (mbar)
P1	1.7E-6
P2	8.9E-2
P3	0
P4	1.4E2
P5	750
P6	5e-4

Fig. A.4: (Left) Cooldown curve with infrared setup (Right) Base temperature and pressure with dilution unit off.

A.2 Setting up the IR measurement

1. Setup the external optics.

    - Begin by mounting the optical enclosure, which houses the off-axis paraboloidal (OAP), at the base of the DR unit and subsequently secure it with a K-50 vacuum clamp. Mount and align the light pipe between the OAP enclosure and the spectrometer. At this stage, the necessary beam splitter and optical window should be mounted for the spectral range of interest. Bring the Vertex 80v Bruker to vacuum and turn on the nitrogen gas supply to the spectrometer, typically set at around 22 psi. There is a green valve located on the OAP enclosure that is used to evacuate the space between the optical window and the gate valve. To evacuate this space, turn on *Scroll 2*, open V23, and switch on *Turbo 2*. Close V23 and open V21 to pump on pressure sensor P6. Close V21 and open the vacuum

on tap (V20) valve; P6 should rise. Open the green valve located on the OAP enclosure, then pump on this space for a few minutes with *Scroll 2* and switch to *Turbo 2* when P6 is below 1 mbar. Close the green valve and pump on the neck of the gate valve for a few minutes. Close all the valves: V20, *Turbo 2*, V23, and *Scroll 2*. The OAP enclosure shares the vacuum of the spectrometer. The pneumatically operated gate valve can now be opened to connect the external optics to the dilution refrigerator.

2. Setup the detector electronics.

   - The detector circuit needs to be powered to set up the IR measurement. It is crucial to follow this sequence to ensure the correct biasing of each component of the detector with the right polarity. Co-axial lines from the detector and JFET circuit inside the dilution refrigerator (DR), extending to room temperature, terminate on an SMA (surface mount assembly) feedthrough located on the top plate of the DR. Use SMA-to-BNC connectors and BNC cables to connect $VD1$, $VD2$, and $G2$ to the op-amp enclosure. The details of the electrical connections for the wiring of the op-amp inside the enclosure are illustrated in Figure A.5a. If the detector circuit is not in use, utilize shorting caps to ground these connections on the front end of the enclosure (as shown in Figure A.5b). Remove the shorting caps (if already connected), and power the JFET at the Cu/Su breakout box using a source meter ($VDD = 10V$ and $VSS = -10V$). Measure the current across the JFET. The value of this current will slowly go up as the JFETs are activated. Measure the current across the JFET. The value of this current will slowly increase as the JFETs are activated. The temperature profile of the STILL plate, bolometer housing, and current across the JFET is illustrated in Figure A.6. It

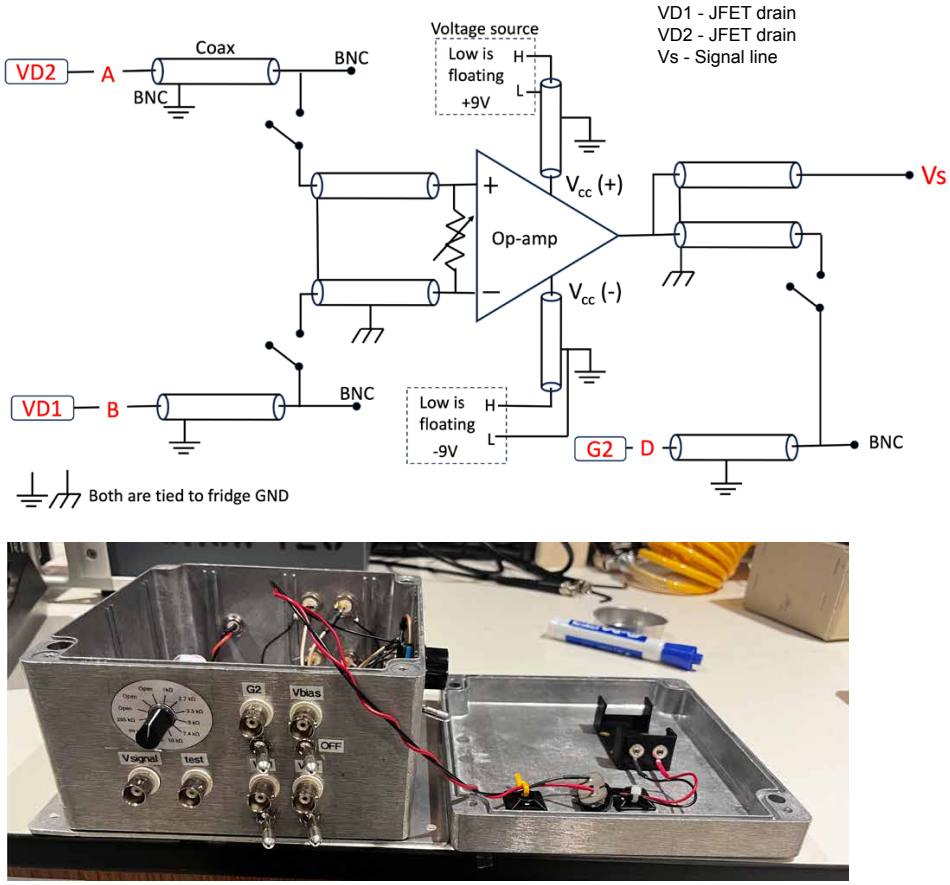

Fig. A.5: (Top) Electrical connections to the room temperature op-amp. (Bottom) The front end of the aluminum case is used as an enclosure for the op-amp circuit.

takes up to 8 hours for the temperature of each component of the preamplifier circuit to stabilize.

- Now is the time to power the op-amp. Flip the two-way switches on the op-amp enclosure front end to connect $VD1$, $VD1$, and $G2$ to establish a connection between the JFET drains and signal line to the op-amp, forming a composite amplifier circuit. Power the op-amp ($\pm$ 9V); the current through the op-amp should read approximately 2.6 mA. Check the temperature of the STILL plate

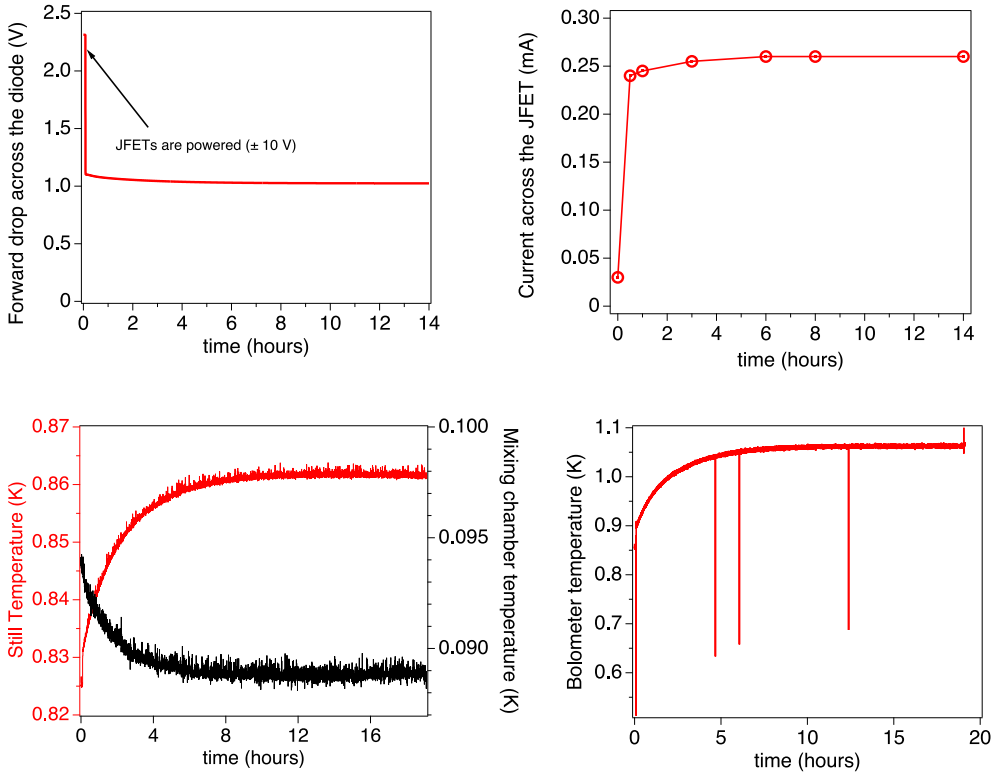

Fig. A.6: Temperature profile of the Si diode thermometer on the JFET board, still plate, bolometer housing, and current across the JFET. It takes roughly 8 hours for all the components of the JFET circuit and fridge cold plate to thermalize after powering the JFETs.

and JFET board; if everything appears stable, bias the bolometer. The enclosure accommodates a bias 9V battery case with a variable resistor to bias the bolometer. However, other source meters like DC205 can also be used. In that case, the co-ax line from the bias line "C" should be directly connected to the source meter. If the magnet is to be used, it is best practice to check the magneto-resistance of the bolometer before and after the magnet is ramped to the desired field value. Connect the signal line $Vsignal$ to the EGG&G preamplifier and ground the preamp input. Pump the gate valve and open the fridge to the external optics. AC couple the input of the EGG&G preamp, adjust the gain and direct the infrared light to the DR. Record the ADC count and peak-to-peak signal voltage on an oscilloscope. Adjust the band-pass filters on the preamp based on the mirror speed used for the step scanner inside the spectrometer. Adjust the OAP mirror to maximize the signal strength. The temperature profile of the STILL plate, mixing chamber, and bolometer housing during this operation is shown in Figure A.7.

A.3 Warming up the DR

- To begin the shutdown procedure, ramp the magnet down to 0 T and cool down the persistent switch heater. Subsequently, switch off the magnet controller and the magnet power supply. Ground the device and redirect the light away from the DR. Proceed to close the gate valve. Ground either the input of the EGGG preamp or directly ground the V_{signal} line at the op-amp enclosure using a shorting cap. Remove the bias and ground the bolometer bias line "C". Power off the op-amp and the JFETs. Maintain the switches on the op-amp enclosure and ground the JFET drain and $G2$

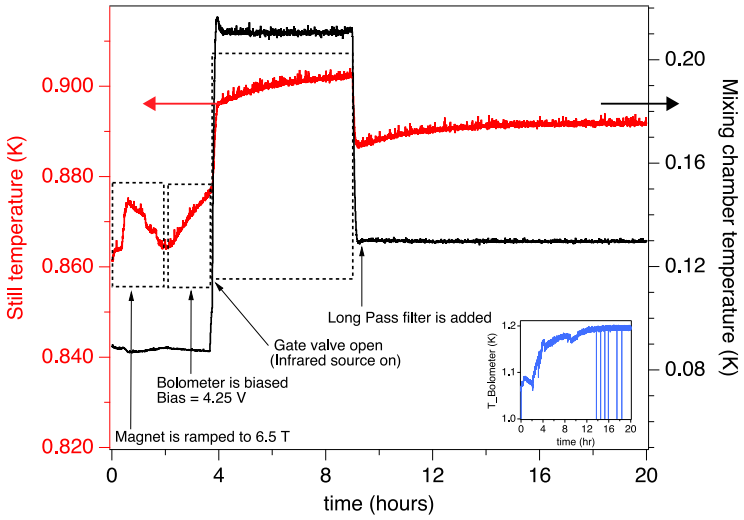

Fig. A.7: Temperature profiles of the still plate, mixing chamber, and bolometer housing are shown after the magnet field is ramped, followed by biasing the bolometer and directing the IR radiation to the DR.

using shorting caps.

- To manually collect the mixture, start by closing V9 and turning off *Turbo 1*. Then, open V13 to direct the mix to the tank. Wait for the *Turbo* to spin down before turning off the external heat to the still plate. Afterward, turn on the heat switches. If no measurements are planned at 4K, the pulse tube can be turned off at this stage. Configure the acquisition software to record the temperature during warmup. Over the next couple of days, the fridge will naturally warm up. To expedite the warm-up process, add some exchange gas using the manual valve to control the addition rate. Ensure the manual valve between the cans and P1 sensor is closed. Burst the vent valve (V19) to allow P6 to rise to 700-900 mbar. Open V16 and V14, then gradually open the manual valve and monitor pressure P6. Slowly open the valve further until a puff of gas is introduced to the DR, recording this value. Apply 20 W heat to the 4K heater; the gas will assist in carrying the heat. Exercise caution as this will rapidly

warm the DR, necessitating regular checks the next day. Disconnect the optics before the DR returns to room temperature. If the pressure increases, the o-ring on the VC will decompress, and the VC can expand and likely bend the light pipe.

Appendix B

Sample fabrication

1. **Transfer**: Exfoliated flakes often need transferring to a different substrate for device fabrication. We employ a dry transfer method using a polymer film on a small PDMS stamp to pick up flakes from a substrate [80]. This stamp can handle multiple flakes, even overlapping, due to van der Waals attraction, enabling complex heterostructures [5]. The polymer, along with the flakes, can then be melted off onto a new substrate. Solvents and thermal annealing remove the polymer, leaving transferred flakes ready for device patterning (see Figure B.1 I).

2. **Contact windows**: We use photolithography to write contact windows on graphene, graphite, and other flakes that need to be exposed. Figure B.1 II shows the exposed contact windows post-writing.

3. **Etch windows**: We predominantly utilize XeF_2 gas to perform a dry chemical etch of h-BN, which we typically cover graphene flakes with, to expose the underlying graphene sheet and graphite for electrical contact or further etching if need be. XeF_2 gas conveniently is extremely reactive with hBN but does not etch graphene whatsoever [119]. The procedure for selective etching of h-BN is schematically described in B.2. This allows us to expose arbitrarily large areas of graphene to evaporate metallic surface

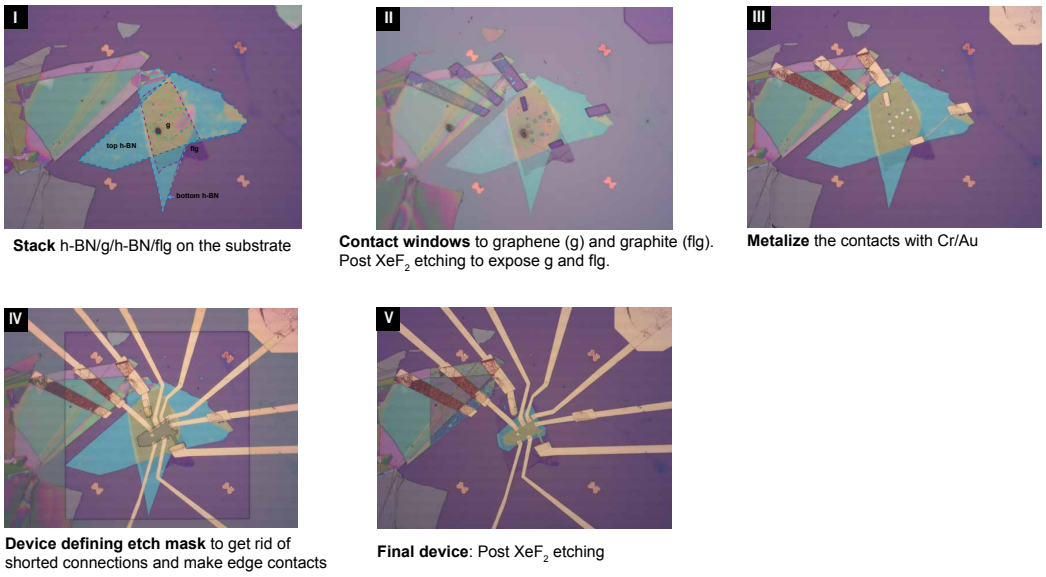

Fig. B.1: Steps for nano-fabrication of vdW heterostructures.

contacts. Etched windows to graphene and few-layer graphene (flg) are shown in Figure B.1 II.

4. **Electrical contacts** can be made to layered materials via metal deposition. There are many deposition methods that work for making contact with 2D materials, but we use thermal evaporation or electron-beam evaporation to evaporate a combination of metals: Cr/Au (Chrome/Gold) contacts or Ti/Al (Titanium/Aluminium). Metalized windows to exposed flakes are shown in Figure B.1 III.

5. **Device define etch**: In order to make contacts for a near-perfect quantum hall geometry or any desired arbitrary shape, we perform photolithography to write an etch mask (see Figure B.1 IV) followed by etching the unwanted flakes using the XeF_2 gas. To characterize the device at room temperature, we begin by testing each contact to the graphene, grounding all but one contact, and measuring the voltage drop in a 2-point configuration. Good samples show contact resistance of a few kΩs or less.

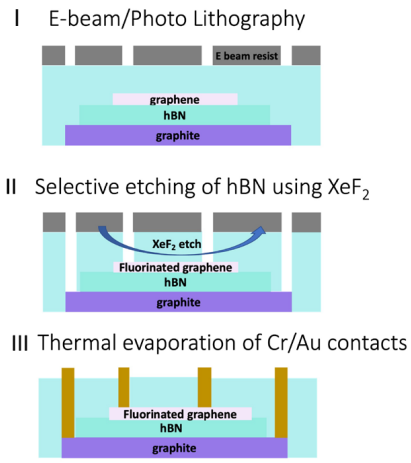

Fig. B.2: (I) Electron-beam lithography or photolithography is employed to define contact windows for the underlying graphene or graphite layer. (II) Selective etching of h-BN is achieved using XeF_2 gas, exposing the buried flakes beneath. (III) Metalization of the exposed regions is performed using Cr/Au deposition through thermal evaporation.

Each fabrication step is crucial to get good contacts. The finished device is shown in Figure B.1 V.

Bibliography

[1] Geim, A. K. & Novoselov, K. S. The rise of graphene. *Nature materials* **6,** 183–191 (2007).

[2] Divigalpitiya, W., Frindt, R. & Morrison, S. R. Inclusion systems of organic molecules in restacked single-layer molybdenum disulfide. *Science* **246,** 369–371 (1989).

[3] Klein, A., Tiefenbacher, S., Eyert, V., Pettenkofer, C. & Jaegermann, W. Electronic band structure of single-crystal and single-layer WS 2: Influence of interlayer van der Waals interactions. *Physical Review B* **64,** 205416 (2001).

[4] Lei, Y. *et al.* Graphene and beyond: Recent advances in two-dimensional materials synthesis, properties, and devices. *ACS Nanoscience Au* **2,** 450–485 (2022).

[5] Geim, A. K. & Grigorieva, I. V. Van der Waals heterostructures. *Nature* **499,** 419–425 (2013).

[6] Novoselov, K. S. *et al.* Electric field effect in atomically thin carbon films. *science* **306,** 666–669 (2004).

[7] Balandin, A. A. *et al.* Superior thermal conductivity of single-layer graphene. *Nano letters* **8,** 902–907 (2008).

[8] Cao, Y. *et al.* Unconventional superconductivity in magic-angle graphene superlattices. *Nature* **556,** 43–50 (2018).

[9] Nair, R. R. *et al.* Fine structure constant defines visual transparency of graphene. *science* **320,** 1308–1308 (2008).

[10] Cooper, D. R. *et al.* Experimental review of graphene. *International Scholarly Research Notices* **2012** (2012).

[11] Basov, D., Fogler, M., Lanzara, A., Wang, F., Zhang, Y., *et al.* Colloquium: graphene spectroscopy. *Reviews of Modern Physics* **86,** 959 (2014).

[12] Wallace, P. R. The band theory of graphite. *Physical review* **71,** 622 (1947).

[13] Das, S. S. Electronic transport in two-dimensional graphene. *Rev Mod Phys* **83,** 430 (2011).

[14] Gusynin, V. & Sharapov, S. Unconventional integer quantum Hall effect in graphene. *Physical review letters* **95,** 146801 (2005).

[15] Novoselov, K. S. *et al.* Unconventional quantum Hall effect and Berryâs phase of 2π in bilayer graphene. *Nature physics* **2,** 177–180 (2006).

[16] Novoselov, K. S. *et al.* Two-dimensional gas of massless Dirac fermions in graphene. *nature* **438,** 197–200 (2005).

[17] Barlas, Y., Yang, K. & MacDonald, A. Quantum Hall effects in graphene-based two-dimensional electron systems. *Nanotechnology* **23,** 052001 (2012).

[18] Zhang, Y., Tan, Y.-W., Stormer, H. L. & Kim, P. Experimental observation of the quantum Hall effect and Berry's phase in graphene. *nature* **438,** 201–204 (2005).

[19] Shockley, W. Cyclotron resonances, magnetoresistance, and Brillouin zones in semiconductors. *Physical Review* **90,** 491 (1953).

[20] Hellstrom, S. Early Measurements of the Band Effective Mass in Silicon Using Cyclotron Resonance.

[21] Galt, J., Yager, W., Merritt, F., Cetlin, B. & Dah Jr, H. Cyclotron resonance in metals: Bismuth. *Physical Review* **100,** 748 (1955).

[22] Dresselhaus, G., Kip, A. & Kittel, C. Cyclotron resonance of electrons and holes in silicon and germanium crystals. *Physical Review* **98,** 368 (1955).

[23] Kohn, W. Cyclotron resonance and de Haas-van Alphen oscillations of an interacting electron gas. *Physical Review* **123,** 1242 (1961).

[24] Chou, M., Tsui, D. & Weimann, G. Cyclotron resonance of high-mobility two-dimensional electrons at extremely low densities. *Physical Review B* **37,** 848 (1988).

[25] Orlita, M. & Potemski, M. Dirac electronic states in graphene systems: optical spectroscopy studies. *Semiconductor Science and Technology* **25,** 063001 (2010).

[26] Rao, P. & Sodemann, I. Cyclotron resonance inside the Mott gap: A fingerprint of emergent neutral fermions. en. *Physical Review B* **100,** 155150. ISSN: 2469-9950, 2469-9969 (2019).

[27] Iyengar, A., Wang, J., Fertig, H. A. & Brey, L. Excitations from filled Landau levels in graphene. *Physical Review B* **75,** 125430 (2007).

[28] Jiang, Z. *et al.* Infrared Spectroscopy of Landau Levels of Graphene. *Physical Review Letters* **98,** 197403 (2007).

[29] Kotov, V. N., Uchoa, B., Pereira, V. M., Guinea, F. & Neto, A. C. Electron-electron interactions in graphene: Current status and perspectives. *Reviews of modern physics* **84,** 1067 (2012).

[30] Kohn, W. Cyclotron resonance and de Haas-van Alphen oscillations of an interacting electron gas. *Physical Review* **123,** 1242–1244 (1961).

[31] Kallin, C. & Halperin, B. I. Many-body effects on the cyclotron resonance in a two-dimensional electron gas. *Physical Review B* **31,** 3635–3647 (1985).

[32] Throckmorton, R. E. & Das Sarma, S. Failure of Kohn's theorem and the apparent failure of the f -sum rule in intrinsic Dirac-Weyl materials in the presence of a filled Fermi sea. en. *Physical Review B* **98,** 155112. ISSN: 2469-9950, 2469-9969 (2018).

[33] Bychkov, Y. A. & Martinez, G. Magnetoplasmon excitations in graphene for filling factors $\nu \leqslant 6$. *Physical Review B* **77,** 125417 (2008).

[34] Shizuya, K. Many-body corrections to cyclotron resonance in monolayer and bilayer graphene. *Physical Review B* **81,** 075407 (2010).

[35] Roldán, R., Fuchs, J.-N. & Goerbig, M. O. Spin-flip excitations, spin waves, and magnetoexcitons in graphene Landau levels at integer filling factors. *Physical Review B* **82,** 205418 (2010).

[36] Faugeras, C. *et al.* Landau Level Spectroscopy of Electron-Electron Interactions in Graphene. *Physical Review Letters* **114,** 126804 (2015).

[37] Sonntag, J. *et al.* Impact of Many-Body Effects on Landau Levels in Graphene. *Physical Review Letters* **120,** 187701 (2018).

[38] Henriksen, E. A. *et al.* Interaction-Induced Shift of the Cyclotron Resonance of Graphene Using Infrared Spectroscopy. *Physical Review Letters* **104,** 067404 (2010).

[39] Chen, Z.-G. *et al.* Observation of an intrinsic bandgap and Landau level renormalization in graphene/boron-nitride heterostructures. *Nature Communications* **5,** 4461 (2014).

[40] Jiang, Y. *et al.* Valley and Zeeman Splittings in Multilayer Epitaxial Graphene Revealed by Circular Polarization Resolved Magneto-infrared Spectroscopy. en. *Nano Letters* **19,** 7043–7049. ISSN: 1530-6984, 1530-6992 (2019).

[41] Nedoliuk, I. O., Hu, S., Geim, A. K. & Kuzmenko, A. B. Colossal infrared and terahertz magneto-optical activity in a two-dimensional Dirac material. en. *Nature Nanotechnology* **14,** 756. ISSN: 1748-3387, 1748-3395 (2019).

[42] Russell, B. J., Zhou, B., Taniguchi, T., Watanabe, K. & Henriksen, E. A. Many-Particle Effects in the Cyclotron Resonance of Encapsulated Monolayer Graphene. *Physical Review Letters* **120,** 047401 (2018).

[43] Fratini, S. & Guinea, F. Substrate-limited electron dynamics in graphene. *Physical Review B* **77,** 195415 (2008).

[44] Ishigami, M., Chen, J.-H., Cullen, W. G., Fuhrer, M. S. & Williams, E. D. Atomic structure of graphene on SiO2. *Nano letters* **7,** 1643–1648 (2007).

[45] Chen, J.-H., Jang, C., Xiao, S., Ishigami, M. & Fuhrer, M. S. Intrinsic and extrinsic performance limits of graphene devices on SiO2. *Nature nanotechnology* **3,** 206–209 (2008).

[46] Martin, J. *et al.* Observation of electron–hole puddles in graphene using a scanning single-electron transistor. *Nature physics* **4,** 144–148 (2008).

[47] Bolotin, K. I. *et al.* Ultrahigh electron mobility in suspended graphene. *Solid state communications* **146,** 351–355 (2008).

[48] Yankowitz, M. *et al.* Emergence of superlattice Dirac points in graphene on hexagonal boron nitride. *Nature Physics* **8,** 382–386 (2012).

[49] Xue, J. *et al.* Scanning tunnelling microscopy and spectroscopy of ultra-flat graphene on hexagonal boron nitride. *Nature materials* **10,** 282–285 (2011).

[50] Decker, R. *et al.* Local electronic properties of graphene on a BN substrate via scanning tunneling microscopy. *Nano letters* **11,** 2291–2295 (2011).

[51] Hofstadter, D. R. Energy levels and wave functions of Bloch electrons in rational and irrational magnetic fields. *Physical review B* **14,** 2239 (1976).

[52] Dean, C. R. *et al.* Hofstadter's butterfly in moire superlattices: A fractal quantum Hall effect. *arXiv preprint arXiv:1212.4783* (2012).

[53] Harper, P. G. Single band motion of conduction electrons in a uniform magnetic field. *Proceedings of the Physical Society. Section A* **68,** 874 (1955).

[54] Wannier, G. A result not dependent on rationality for Bloch electrons in a magnetic field. *physica status solidi (b)* **88,** 757–765 (1978).

[55] Moon, P. & Koshino, M. Electronic properties of graphene/hexagonal-boron-nitride moiré superlattice. *Physical Review B* **90,** 155406 (2014).

[56] Griffiths, P. R. & de Haseth, J. A. *Fourier Transform Infrared Spectrometry* Second (Wiley-Interscience, New York, 2007).

[57] Aschcroft, N. Solid State Theory. *Holt, Rinehart, and Wilson* (1976).

[58] Kennes, D. M. *et al.* Moiré heterostructures as a condensed-matter quantum simulator. *Nature Physics* **17,** 155–163 (2021).

[59] Savary, L. & Balents, L. Quantum spin liquids: a review. *Reports on Progress in Physics* **80,** 016502 (2016).

[60] Sulewski, P. *et al.* Far-infrared absorptivity of UPt 3. *Physical Review B* **38,** 5338 (1988).

[61] Neumann, V., Laurita, N., Pan, L. & Armitage, N. Reduction of effective terahertz focal spot size by means of nested concentric parabolic reflectors. *AIP advances* **5** (2015).

[62] Sudiwala, R. V., Griffin, M. J. & Woodcraft, A. Thermal modelling and characterisation of semiconductor bolometers. *International Journal of Infrared and Millimeter Waves* **23,** 545–573 (2002).

[63] Richards, P. L. Bolometers for infrared and millimeter waves. *Journal of Applied Physics* **76,** 1–24 (1994).

[64] Mather, J. C. Bolometer noise: nonequilibrium theory. *Applied optics* **21,** 1125–1129 (1982).

[65] Johnson, J. B. Thermal agitation of electricity in conductors. *Physical review* **32,** 97 (1928).

[66] McClure, J. W. Diamagnetism of graphite. *Physical Review* **104,** 666–671 (1956).

[67] Gusynin, V. P., Sharapov, S. G. & Carbotte, J. P. Anomalous Absorption Line in the Magneto-Optical Response of Graphene. *Physical Review Letters* **98,** 157402 (2007).

[68] Young, A. F. *et al.* Spin and valley quantum Hall ferromagnetism in graphene. en. *Nature Physics* **8,** 550–556. ISSN: 1745-2473, 1745-2481 (2012).

[69] Dean, C. R. *et al.* Boron nitride substrates for high-quality graphene electronics. *Nature Nanotechnology* **5,** 722–726. ISSN: 1748-3387, 1748-3395 (2010).

[70] Giovannetti, G., Khomyakov, P. A., Brocks, G., Kelly, P. J. & Van Den Brink, J. Substrate-induced band gap in graphene on hexagonal boron nitride: Ab initio density functional calculations. *Physical Review B* **76,** 073103 (2007).

[71] Zhang, Y. *et al.* Landau-Level Splitting in Graphene in High Magnetic Fields. *Physical Review Letters* **96,** 136806 (2006).

[72] Checkelsky, J., Li, L. & Ong, N. P. Zero-Energy State in Graphene in a High Magnetic Field. *Physical Review Letters* **100,** 206801 (2008).

[73] Song, Y. J. *et al.* High-resolution tunnelling spectroscopy of a graphene quartet. *Nature* **467,** 185–189 (2010).

[74] Hunt, B. *et al.* Massive Dirac Fermions and Hofstadter Butterfly in a van der Waals Heterostructure. *Science* **340,** 1427–1430 (2013).

[75] Zibrov, A. A. *et al.* Even-denominator fractional quantum Hall states at an isospin transition in monolayer graphene. en. *Nature Physics* **14,** 930–935. ISSN: 1745-2473, 1745-2481 (2018).

[76] Li, S.-Y., Zhang, Y., Yin, L.-J. & He, L. Scanning Tunneling Microscope Study of Quantum Hall Isospin Ferromagnetic States in the Zero Landau Level in a Graphene Monolayer. en. *Physical Review B* **100,** 085437. ISSN: 2469-9950, 2469-9969 (2019).

[77] Onodera, M. *et al.* Cyclotron Resonance Study of Monolayer Graphene under Double MoirÃ© Potentials. en. *Nano Letters* **20,** 4566. ISSN: 1530-6984, 1530-6992 (2020).

[78] Dresselhaus, G., Kip, A. & Kittel, C. Observation of cyclotron resonance in germanium crystals. *Physical Review* **92,** 827–827 (1953).

[79] Hilton, D. J., Arikawa, T. & Kono, J. in *Characterization of Materials* (John Wiley and Sons, 2012).

[80] Wang, L. *et al.* One-Dimensional Electrical Contact to a Two-Dimensional Material. *Science* **342,** 614–617 (2013).

[81] Gusynin, V. P., Sharapov, S. G. & Carbotte, J. P. Unusual Microwave Response of Dirac Quasiparticles in Graphene. *Physical Review Letters* **96,** 256802 (2006).

[82] Zibrov, A. A. *et al.* Tunable interacting composite fermion phases in a half-filled bilayer-graphene Landau level. *Nature* **549,** 360–364 (2017).

[83] Coleridge, P. T., Stoner, R. & Fletcher, R. Low-field transport coefficients in GaAs/$Ga_{1-x}Al_xAs$ heterostructures. *Physical Review B* **39,** 1120–1124 (1989).

[84] Syed, S., Manfra, M. J., Wang, Y. J., Molnar, R. J. & Stormer, H. L. Electron scattering in AlGaN/GaN structures. *Applied Physics Letters* **84,** 1507 (2004).

[85] Shizuya, K. Many-body effects on Landau-level spectra and cyclotron resonance in graphene. en. *Physical Review B* **98,** 115419. ISSN: 2469-9950, 2469-9969 (2018).

[86] Jung, J., DaSilva, A. M., MacDonald, A. H. & Adam, S. Origin of band gaps in graphene on hexagonal boron nitride. *Nature Communications* **6,** 6308 (2015).

[87] Sokolik, A. A. & Lozovik, Y. E. Many-body filling factor dependent renormalization of Fermi velocity in graphene in strong magnetic field. en. *Physical Review B* **99,** 085423. ISSN: 2469-9950, 2469-9969 (2019).

[88] Dial, O., Ashoori, R. C., Pfeiffer, L. N. & West, K. W. High-resolution spectroscopy of two-dimensional electron systems. *Nature* **448,** 176–179 (2007).

[89] Kharitonov, M. Phase diagram for the $\nu = 0$ quantum Hall state in monolayer graphene. *Physical Review B* **85,** 155439–23 (2012).

[90] Peres, N. M. R., Guinea, F. & Castro Neto, A. H. Electronic properties of disordered two-dimensional carbon. *Physical Review B* **73,** 125411 (2006).

[91] Plochocka, P. *et al.* High-Energy Limit of Massless Dirac Fermions in Multilayer Graphene using Magneto-Optical Transmission Spectroscopy. *Physical Review Letters* **100,** 087401 (2008).

[92] Deacon, R. S., Chuang, K.-C., Nicholas, R. J., Novoselov, K. S. & Geim, A. K. Cyclotron resonance study of the electron and hole velocity in graphene monolayers. *Physical Review B* **76,** 081406 (2007).

[93] Nakamura, D., Saito, H., Hibino, H., Asano, K. & Takeyama, S. Quantum Limit Cyclotron Resonance in Monolayer Epitaxial Graphene in Magnetic Fields up to 560 T: The Relativistic Electron and Hole Asymmetry. en. *Physical Review B* **101,** 115420. ISSN: 2469-9950, 2469-9969 (2020).

[94] MacDonald, A. H., Oji, H. C. A. & Girvin, S. M. Magnetoplasmon Excitations from Partially Filled Landau Levels in Two Dimensions. en. *Physical Review Letters* **55,** 2208–2211. ISSN: 0031-9007 (1985).

[95] Gonzalez, J., Guinea, F. & Vozmediano, M. Non-Fermi liquid behavior of electrons in the half-filled honeycomb lattice (A renormalization group approach). *Nuclear Physics B* **424,** 595 (1994).

[96] Elias, D. C. *et al.* Dirac cones reshaped by interaction effects in suspended graphene. *Nature Physics* **7,** 701–704 (2011).

[97] Laturia, A., Van de Put, M. L. & Vandenberghe, W. G. Dielectric Properties of Hexagonal Boron Nitride and Transition Metal Dichalcogenides: From Monolayer to Bulk. en. *npj 2D Materials and Applications* **2,** 6. ISSN: 2397-7132 (2018).

[98] Hattori, Y., Taniguchi, T., Watanabe, K. & Nagashio, K. Layer-by-Layer Dielectric Breakdown of Hexagonal Boron Nitride. *ACS Nano* **9,** 916–921 (2015).

[99] Song, J. C. W., Shytov, A. V. & Levitov, L. S. Electron Interactions and Gap Opening in Graphene Superlattices. *Physical Review Letters* **111,** 266801 (2013).

[100] Kim, H. *et al.* Accurate Gap Determination in Monolayer and Bilayer Graphene/*h*-BN Moiré Superlattices. en. *Nano Letters* **18,** 7732–7741. ISSN: 1530-6984, 1530-6992 (2018).

[101] Batke, E., Stormer, H. L., Gossard, A. C. & English, J. Filling-factor-dependent cyclotron mass in space-charge layers on GaAs. *Physical Review B* **37,** 3093–3096 (1988).

[102] MacDonald, A. H. & Kallin, C. Cyclotron resonance in two dimensions: Electron-electron interactions and band nonparabolicity. *Physical Review B* **40,** 5795–5798 (1989).

[103] Manger, M. *et al.* Filling-factor-dependent electron correlations observed in cyclotron resonance. *Physical Review B* **63,** 121203 (2001).

[104] Schlesinger, Z., Allen Jr, S. J., Hwang, J. C. M., Platzman, P. & Tzoar, N. Cyclotron resonance in two dimensions. *Physical Review B* **30,** 435–437 (1984).

[105] Henriksen, E. A. *et al.* Disorder-mediated splitting of the cyclotron resonance in two-dimensional electron systems. *Physical Review B* **73,** 241309 (2006).

[106] Summers, G. M. *et al.* New phases of the 2D electron system in the ultra-quantum limit observed by cyclotron resonances. en. *Physical Review Letters* **70,** 2150–2153. ISSN: 0031-9007 (1993).

[107] Cooper, N. & Chalker, J. T. Theory of spin-split cyclotron resonance in the extreme quantum limit. *Physical Review Letters* **72,** 2057–2060 (1994).

[108] Maag, T. *et al.* Coherent cyclotron motion beyond Kohn's theorem. *Nature Physics* **12,** 119–123 (2015).

[109] Batke, E., Heitmann, D., Kotthaus, J. & Ploog, K. Nonlocality in the two-dimensional plasmon dispersion. *Physical Review Letters* **54,** 2367–2370 (1985).

[110] Zhao, Y. *et al.* Grating-induced cyclotron-resonance anomaly in GaAs/$Al_xGa_{1-x}As$ heterostructures. *Physical Review B* (1995).

[111] Kukushkin, I. V., Smet, J. H., Schuh, D., Wegscheider, W. & Von Klitzing, K. Dispersion of the Composite-Fermion Cyclotron-Resonance Mode. *Physical Review Letters* **98,** 066403 (2007).

[112] Gerhardts, R. R., Weiss, D. & Wulf, U. Magnetoresistance oscillations in a grid potential: Indication of a Hofstadter-type energy spectrum. *Physical Review B* **43,** 5192 (1991).

[113] Nakamura, Y., Inoshita, T. & Sakaki, H. Novel magneto-resistance oscillations in laterally modulated two-dimensional electrons with 20 nm periodicity formed on vicinal GaAs (1 1 1) B substrates. *Physica E: Low-dimensional Systems and Nanostructures* **2,** 944–948 (1998).

[114] Geisler, M. *et al.* Detection of a Landau band-coupling-induced rearrangement of the Hofstadter butterfly. *Physical review letters* **92,** 256801 (2004).

[115] Schlösser, T., Ensslin, K., Kotthaus, J. P. & Holland, M. Landau subbands generated by a lateral electrostatic superlattice-chasing the Hofstadter butterfly. *Semiconductor Science and Technology* **11,** 1582 (1996).

[116] Wallbank, J. R., Mucha-Kruczyński, M., Chen, X. & Fal'Ko, V. I. Moiré superlattice effects in graphene/boron-nitride van der Waals heterostructures. *Annalen der Physik* **527,** 359–376 (2015).

[117] Ponomarenko, L. *et al.* Cloning of Dirac fermions in graphene superlattices. *Nature* **497,** 594–597 (2013).

[118] Kim, K. *et al.* van der Waals heterostructures with high accuracy rotational alignment. *Nano letters* **16,** 1989–1995 (2016).

[119] Son, J. *et al.* Atomically precise graphene etch stops for three dimensional integrated systems from two dimensional material heterostructures. *Nature communications* **9,** 3988 (2018).

[120] Koshino, M. & Ando, T. Hall plateau diagram for the Hofstadter butterfly energy spectrum. *Physical Review B* **73,** 155304 (2006).

[121] Park, C.-H., Yang, L., Son, Y.-W., Cohen, M. L. & Louie, S. G. New generation of massless Dirac fermions in graphene under external periodic potentials. *Physical review letters* **101,** 126804 (2008).

[122] Chen, Z.-G. *et al.* Observation of an intrinsic bandgap and Landau level renormalization in graphene/boron-nitride heterostructures. *Nature communications* **5,** 4461 (2014).

[123] Jung, J. *et al.* Moiré band model and band gaps of graphene on hexagonal boron nitride. *Physical Review B* **96,** 085442 (2017).

[124] Kim, H. *et al.* Accurate gap determination in monolayer and bilayer graphene/h-BN Moiré superlattices. *Nano letters* **18,** 7732–7741 (2018).

[125] Pack, J. *et al.* Broken symmetries and Kohnâs theorem in graphene cyclotron resonance. *Physical Review X* **10,** 041006 (2020).

[126] Moon, P. & Koshino, M. Energy spectrum and quantum Hall effect in twisted bilayer graphene. *Physical Review B* **85,** 195458 (2012).

[127] Vogl, P. & Strahberger, C. Self-Similar Optical Absorption Spectra in High Magnetic Fields. *physica status solidi (b)* **234,** 472–477 (2002).

[128] Moon, P. & Koshino, M. Optical properties of the Hofstadter butterfly in the moiré superlattice. *Physical Review B* **88,** 241412 (2013).

[129] Tung, L.-C. *et al.* Magnetoinfrared spectroscopic study of thin Bi 2 Te 3 single crystals. *Physical Review B* **93,** 085140 (2016).

[130] Tang, T.-T. *et al.* A tunable phonon–exciton Fano system in bilayer graphene. *Nature nanotechnology* **5,** 32–36 (2010).

[131] Imran, M., Haney, P. M. & Barlas, Y. Hofstadter moiré butterfly in twisted trilayer graphene. *Physical Review B* **108,** 085417 (2023).

[132] Yang, W. & Zhang, G. Hofstadter butterfly in graphene. *arXiv preprint arXiv:2203.05821* (2022).

[133] Chen, S. *et al.* Competing Fractional Quantum Hall and Electron Solid Phases in Graphene. en. *Physical Review Letters* **122,** 026802. ISSN: 0031-9007, 1079-7114 (2019).

[134] Yankowitz, M. *et al.* Tuning superconductivity in twisted bilayer graphene. *Science* **363,** 1059–1064 (2019).

[135] Serlin, M. *et al.* Intrinsic quantized anomalous Hall effect in a moiré heterostructure. *Science* **367,** 900–903 (2020).

[136] Dresselhaus, M. S. & Dresselhaus, G. Intercalation compounds of graphite. *Advances in physics* **51,** 1–186 (2002).

[137] McCann, E. & Falâko, V. I. Landau-level degeneracy and quantum Hall effect in a graphite bilayer. *Physical review letters* **96,** 086805 (2006).

[138] Mucha-Kruczyński, M., McCann, E. & Fal'Ko, V. I. Electron–hole asymmetry and energy gaps in bilayer graphene. *Semiconductor science and technology* **25,** 033001 (2010).

[139] Castro, E. V. *et al.* Biased bilayer graphene: semiconductor with a gap tunable by the electric field effect. *Physical review letters* **99,** 216802 (2007).

[140] Mucha-Kruczyński, M. *et al.* Characterization of graphene through anisotropy of constant-energy maps in angle-resolved photoemission. *Physical Review B* **77,** 195403 (2008).

[141] McCann, E. Asymmetry gap in the electronic band structure of bilayer graphene. *Phys. Rev. B* **74,** 1–4. ISSN: 10980121. arXiv: `0608221 [cond-mat]` (2006).

[142] Abergel, D. S. L. & Fal'ko, V. I. Optical and magneto-optical far-infrared properties of bilayer graphene. *Phys. Rev. B* **75,** 155430. ISSN: 10980121. arXiv: `0610673 [cond-mat]` (2007).

[143] Henriksen, E. A. *et al.* Cyclotron resonance in bilayer graphene. *Phys. Rev. Lett.* **100,** 087403. ISSN: 00319007 (2008).

[144] Orlita, M. *et al.* Magneto-optics of bilayer inclusions in multilayered epitaxial graphene on the carbon face of SiC. *Physical Review B* **83.** ISSN: 1550-235X. `http://dx.doi.org/10.1103/PhysRevB.83.125302` (2011).

[145] Moriya, R. *et al.* Probing many-body interactions in the cyclotron resonance of *h*-BN/bilayer graphene/*h*-BN. *Physical Review B* **104.** ISSN: 2469-9969. http://dx.doi.org/10.1103/PhysRevB.104.245137 (2021).

[146] Liu, X. *et al.* Visualizing broken symmetry and topological defects in a quantum Hall ferromagnet. *Science* **375,** 321–326 (2022).

[147] Young, A. F. *et al.* Tunable symmetry breaking and helical edge transport in a graphene quantum spin Hall state. *Nature* **505,** 528â532. ISSN: 1476-4687. http://dx.doi.org/10.1038/nature12800 (2014).

[148] McCann, E. & Koshino, M. The electronic properties of bilayer graphene. *Reports on Progress in Physics* **76,** 056503. ISSN: 00344885. arXiv: 1205.6953. https://iopscience.iop.org/article/10.1088/0034-4885/76/5/056503%20http://arxiv.org/abs/1205.6953%20http://dx.doi.org/10.1088/0034-4885/76/5/056503 (2013).

[149] Zhang, L. M., Fogler, M. M. & Arovas, D. P. Magnetoelectric coupling, Berry phase, and Landau level dispersion in a biased bilayer graphene. *Phys. Rev. B* **84,** 075451. ISSN: 10980121 (2011).

[150] Barlas, Y., Cote, R., Nomura, K. & MacDonald, A. H. Intra-Landau level Cyclotron Resonance in Bilayer Graphene. *Phys. Rev. Lett.* **101,** 1–5. http://arxiv.org/abs/0803.0044%0Ahttp://dx.doi.org/10.1103/PhysRevLett.101.097601 (2008).

[151] Sári, J. & Toke, C. Theory of inter-Landau-level magnetoexcitons in bilayer graphene. *Phys. Rev. B* **87,** 085432. ISSN: 10980121. https://link.aps.org/doi/10.1103/PhysRevB.87.085432 (2013).

[152] Murthy, G., Shimshoni, E. & Fertig, H. A. Spin-valley coherent phases of the ν=0 quantum Hall state in bilayer graphene. *Phys. Rev. B* **96,** 245125. ISSN: 24699969 (2017).

[153] Shizuya, K. Many-body effects, orbital mixing and cyclotron resonance in bilayer graphene. *Phys. Rev. B* **101,** 195429. ISSN: 2469-9950. https://link.aps.org/doi/10.1103/PhysRevB.101.195429%20http://arxiv.org/abs/2005.06737%20http://dx.doi.org/10.1103/PhysRevB.101.195429 (2020).

[154] Kharitonov, M. Canted antiferromagnetic phase of the ν=0 quantum Hall state in bilayer graphene. *Phys. Rev. Lett.* **109,** 046803. ISSN: 00319007. https://link.aps.org/doi/10.1103/PhysRevLett.109.046803 (2012).

[155] Shizuya, K. Renormalization and cyclotron resonance in bilayer graphene with weak electron-hole asymmetry. *Phys. Rev. B* **84,** 075409. ISSN: 10980121. https://link.aps.org/doi/10.1103/PhysRevB.84.075409%20http://arxiv.org/abs/1103.5696%20http://dx.doi.org/10.1103/PhysRevB.84.075409 (2011).

[156] Schossler, M., Russell, B. J., Seidel, A., Henriksen, E. A. & Barlas, Y. Cyclotron resonance in bilayer graphene. *work in progress.* GitHub repository (2023).

[157] Min, H., Sahu, B., Banerjee, S. K. & MacDonald, A. H. Ab initio theory of gate induced gaps in graphene bilayers. *Phys. Rev. B* **75,** 155115. https://link.aps.org/doi/10.1103/PhysRevB.75.155115 (15 2007).

[158] Zhang, Y. *et al.* Direct observation of a widely tunable bandgap in bilayer graphene. *Nature* **459,** 820–823. ISSN: 00280836. http://dx.doi.org/10.1038/nature08105 (2009).

[159] Mak, K. F., Lui, C. H., Shan, J. & Heinz, T. F. Observation of an electric-field-induced band gap in bilayer graphene by infrared spectroscopy. *Phys. Rev. Lett.* **102,** 256405. ISSN: 00319007 (2009).

[160] Maher, P. *et al.* Evidence for a spin phase transition at charge neutrality in bilayer graphene. *Nature Physics* **9,** 154–158. ISSN: 17452481 (2013).

[161] Fu, H., Huang, K., Watanabe, K., Taniguchi, T. & Zhu, J. Gapless Spin Wave Transport through a Quantum Canted Antiferromagnet. *Phys. Rev. X* **11,** 021012. https://link.aps.org/doi/10.1103/PhysRevX.11.021012 (2 2021).

[162] Kallin, C. & Halperin, B. I. Excitations from a filled Landau level in the two-dimensional electron gas. *Phys. Rev. B* **30,** 5655–5668. ISSN: 01631829 (1984).

[163] Bisti, V. E. & Kirova, N. N. Coulomb interaction and electron-hole asymmetry in cyclotron resonance of bilayer graphene in a high magnetic field. *Phys. Rev. B* **84,** 155434. ISSN: 10980121. https://link.aps.org/doi/10.1103/PhysRevB.84.155434 (2011).

[164] Knothe, A. & Jolicoeur, T. Phase diagram of a graphene bilayer in the zero-energy Landau level. *Physical Review B* **94.** ISSN: 2469-9969. http://dx.doi.org/10.1103/PhysRevB.94.235149 (2016).

[165] De Nova, J. R. M. & Zapata, I. Symmetry characterization of the collective modes of the phase diagram of the $\nu = 0$ quantum Hall state in graphene: Mean-field phase diagram and spontaneously broken symmetries. *Phys. Rev. B* **95,** 165427. ISSN: 2469-9950. http://link.aps.org/doi/10.1103/PhysRevB.95.165427 (2017).

[166] Green, B. R. & Sofo, J. O. Landau level phases in bilayer graphene under pressure at charge neutrality. *Physical Review B* **101.** ISSN: 2469-9969. http://dx.doi.org/10.1103/PhysRevB.101.195432 (2020).

[167] Lee, K. *et al.* Chemical potential and quantum Hall ferromagnetism in bilayer graphene. *Science* **345,** 58–61. ISSN: 0036-8075. https://www.science.org/doi/10.1126/science.1251003 (2014).

[168] Hunt, B. M. *et al.* Direct measurement of discrete valley and orbital quantum numbers in bilayer graphene. *Nature Communications* **8,** 1–7. ISSN: 20411723 (2017).

[169] Li, J., Tupikov, Y., Watanabe, K., Taniguchi, T. & Zhu, J. Effective Landau Level Diagram of Bilayer Graphene. *Phys. Rev. Lett.* **120,** 047701. ISSN: 10797114. https://doi.org/10.1103/PhysRevLett.120.047701 (2018).

[170] Cao, Y. *et al.* Correlated insulator behaviour at half-filling in magic-angle graphene superlattices. *Nature* **556,** 80â84. ISSN: 1476-4687. http://dx.doi.org/10.1038/nature26154 (2018).

[171] Park, J. M., Cao, Y., Watanabe, K., Taniguchi, T. & Jarillo-Herrero, P. Tunable strongly coupled superconductivity in magic-angle twisted trilayer graphene. *Nature* **590,** 249â255. ISSN: 1476-4687. http://dx.doi.org/10.1038/s41586-021-03192-0 (2021).

[172] Zhang, Q. *et al.* Collective non-perturbative coupling of 2D electrons with high-quality-factor terahertz cavity photons. *Nature Physics* **12,** 1005–1011 (2016).

[173] Hagenmüller, D. & Ciuti, C. Cavity QED of the graphene cyclotron transition. *Physical Review Letters* **109,** 267403 (2012).

[174] Xin, N. *et al.* Giant magnetoresistance of Dirac plasma in high-mobility graphene. *Nature* **616,** 270–274 (2023).

[175] Cruise, J. R., Seidel, A., Henriksen, E. & Vignale, G. Observability of cyclotron resonance in the hydrodynamic regime of bilayer graphene. *arXiv preprint arXiv:2402.02231* (2024).